

**Expanding the palette of genetically-encoded calcium ion
indicators for monitoring neural activity**

by

Yong Qian

A thesis submitted in partial fulfillment of requirements for the degree of

Doctor of Philosophy

Department of Chemistry

University of Alberta

© Yong Qian, 2019

Abstract

Light-emitting proteins, including both fluorescent proteins, luciferases, and their derivative indicators, have equipped scientists with a variety of genetically-encoded tools for non-invasively visualizing cellular signaling networks. Calcium ion (Ca^{2+}) imaging is one of the most widely used imaging technologies due to the pivotal roles that Ca^{2+} plays in cell biology. In neuroscience, Ca^{2+} imaging with genetically encoded Ca^{2+} indicators (GECIs) is a robust approach to monitor neural activity. Furthermore, the combined use of GECIs with optogenetic actuators (*i.e.*, channelrhodopsins) for simultaneously measuring and controlling neural activity in the nervous system could, in principle, provide critical insights into molecular mechanism behind brain networks. However, currently available fluorescent GECIs exhibit substantial spectral overlap with optogenetic actuators, which makes it challenging to image the GECI without also activating optogenetic actuators. In this thesis, I describe two approaches for overcoming this challenge: the development of a bioluminescent Ca^{2+} indicator and near-infrared (NIR) fluorescent Ca^{2+} indicator.

In this thesis, I first describe my efforts to develop a ratiometric bioluminescent Ca^{2+} indicator, LUCI-GECO1, based on one of the brightest luciferase, Nanoluc, and a topological variant of GCaMP6s, ncpGCaMP6s. LUCI-GECO1 retains the high Ca^{2+} affinity of ncpGCaMP6s and outperformed another ratiometric bioluminescent Ca^{2+} indicator CalfluxVTN in histamine-treated HeLa cells. Due to the lack of external excitation, LUCI-GECO1 is compatible with channelrhodopsins.

I also describe a genetically-encoded NIR fluorescent Ca^{2+} indicator, NIR-GECO1, with excitation and emission maxima at 678 nm and 704 nm, respectively. NIR-GECO1 was engineered based on a monomeric near-infrared FP, mIFP, through extensive directed evolution. Working with collaborators, we demonstrated that NIR-GECO1 was able to reliably report Ca^{2+} transients in cultured neurons, in acute brain slice and in mouse brain *in vivo* at mesoscale. Due to the highly red-shifted spectra, imaging of NIR-GECO1 has essentially no crosstalk with the stimulation of the high photocurrent channelrhodopsin CoChR. NIR-GECO1 also enabled multiparameter imaging in conjunction with other fluorescent-protein-based intensimetric and ratiometric indicators.

Finally, I describe efforts to further improve the properties of NIR-GECO1. I performed three additional rounds of directed evolution and selected a new variant, NIR-GECO2. Compared to NIR-GECO1, NIR-GECO2 enables more sensitive Ca^{2+} imaging in cultured neurons and acute brain slices with 50% improvement in cellular brightness and a K_d of 102 nM (the K_d of NIR-GECO1 is 215 nM). Working with collaborators, I expressed NIR-GECO2 in *C. elegans* and successfully detected spontaneous neural activity in worms *in vivo*. I anticipate that NIR-GECO2 will be an excellent tool for studying central nervous system (CNS) circuits and complex behaviors of *C. elegans* and other model organisms.

Preface

A version of Chapter 2 of this thesis has been published as Y. Qian, V. Rancic J. Wu, K. Ballanyi and R. E. Campbell, “A bioluminescent Ca^{2+} indicator based on a topological variant of GCaMP6s”. *ChemBioChem*, 20, 516-520 (2019) (VIP, cover feature). Y.Q. developed LUCI-GECO1, performed *in vitro* characterization of ncpGCaMP6s and LUCI-GECO1, and imaged LUCI-GECO1 in HeLa cells and dissociated neurons. V.R. performed electrophysiology and cytosolic Ca^{2+} imaging of GCaMP6s and ncpGCaMP6s in dissociated neurons. J.W. constructed ncpGCaMP6s. All authors were involved in data analysis. Y.Q. and R.E.C. wrote the manuscript.

A version of Chapter 3 of this thesis has been published as Y. Qian, K.D. Piatkevich, B. Mc Larney, A.S. Abdelfattah, S. Mehta, M.H. Murdock, S. Gottschalk, R.S. Molina, W. Zhang, Y. Chen, J. Wu, M. Drobizhev, T.E. Hughes, J. Zhang, E.R. Schreiter, S. Shoham, D. Razansky, E.S. Boyden, and R.E. Campbell, “A genetically-encoded near-infrared fluorescent calcium ion indicator”, *Nature Methods*, 16, 171-174 (2019). Y.Q. developed NIR-GECO1 and performed *in vitro* characterization. Y.Q., K.D.P., A.S.A. and M.H.M. performed characterization in hippocampal neurons. K.D.P. and M.H.M. characterized NIR-GECO1 in intact brain slices. B.M.L. and S.G. performed *in vivo* mesoscale imaging. S.M. performed live-cell imaging in MIN6 β -cells. R.S.M. and M.D. measured two-photon spectra. W.Z. built the pcDuEx2 vector. Y.C. and J.W. worked on development of the smURFP-based GECl. M.D., T.E.H., J.Z., E.R.S., S.S., D.R.,

E.S.B. and R.E.C. supervised research. All authors were involved in data analysis.

Y.Q., K.D.P. and R.E.C. wrote the manuscript.

Acknowledgements

Foremost, I would like to say thank you to my Ph.D. supervisor Dr. Robert E. Campbell for his strong support and patient guidance during my Ph.D. study and research. Without him, I wouldn't step in this colorful and fascinating interdisciplinary area that combines protein engineering and neuroscience. A Ph.D. career might be tough with all the difficulties and obstacles that I have met, but his passion, intelligence and valuable advices can always guide me to the right direction. I feel so lucky that I have such a considerate advisor and mentor who supports me from many aspects. I would also like to thank my thesis committee: Dr. Todd Lowary, Dr. Matthew Macauley, Dr. Lingzi Sang and Dr. Xiaokun Shu from Department of Pharmaceutical Chemistry, University of California, San Francisco for attending my Ph. D. defense and providing me valuable reviews and comments on my thesis.

I sincerely thank my lab member and friend Dr. Wei Zhang who was always there when I had questions. I also thank Dr. Jiahui Wu, who gave me tremendous help when I first joined the group. Because their contribution, I could initiate and proceed my research projects more smoothly. I really appreciate the help from our lab members, their contribution to the lab have made my research life much easier.

I would also like to thank our collaborators, especially Dr. Kiryl D. Piatkevich, Dr. Vladimir Rancic and Ben Mc Larney. Without their efforts, much of the work described in this thesis would not have been possible.

Finally, I would like to express my sincere gratitude to my parents and sisters for their support and understanding over these years.

Table of Contents

Abstract	ii
Preface	iv
Acknowledgements	vi
Table of Contents	vii
List of Tables	xi
List of Figures	xii
List of Abbreviations	xv
Chapter 1: Introduction	1
1.1 Fluorescent proteins and genetically-encoded fluorescent indicators ...	2
1.1.1 β -barrel shaped fluorescent proteins with autogenic fluorophores .	2
1.1.2 Endogenous chromophore-binding fluorescent proteins engineered from natural photoreceptors.....	4
1.1.3 Genetically-encoded fluorescent indicators based on fluorescent proteins	11
1.1.3.1. Single FP-based indicators	11
<i>FP-only indicators</i>	11
<i>GCaMP-type indicators with external modulation</i>	12
<i>BiFC-based indicators</i>	13
1.1.3.2. Multiple FP-based indicators	14
<i>FRET-based indicators</i>	14
<i>ddFP- and FLINC-based indicators</i>	15
1.2 Bioluminescent proteins and indicators	18
1.2.1 Bioluminescence	18
1.2.2 Luciferase	20
<i>Improving luciferase brightness using directed evolution</i>	21
<i>Improving luciferase brightness using BRET</i>	21
<i>Improving luciferase brightness by development of new luciferase- luciferin pairs</i>	22

1.2.3 Genetically-encoded bioluminescent indicators.....	25
1.3 Multiplexing light-emitting genetically-encoded indicators and light driven-actuators.....	29
1.3.1 Spectral separation of optogenetic actuators and indicators	31
<i>Blue light-activated channelrhodopsins with red light-excited voltage indicators</i>	31
<i>Yellow/red-light activated channelrhodopsins with blue light-excited GCaMP Ca²⁺ indicator</i>	32
<i>Blue-shifted channelrhodopsin with orange-light excited Ca²⁺ indicator</i>	33
<i>Channelrhodopsins with bioluminescent indicators</i>	33
1.3.2 Spatial separation of optogenetic indicators and actuators	34
1.4 The scope of the thesis	36
Chapter 2: A Bioluminescent Ca ²⁺ Indicator Based on a Topological Variant of GCaMP6s.....	39
2.1 Abstract	39
2.2 Introduction.....	39
2.3 Results and discussion.....	44
2.4 Conclusion.....	58
2.5 Materials and methods	58
2.5.1 General methods and materials.....	58
2.5.2 Construction and engineering of LUCI-GECO1	59
2.5.3 Protein purification and <i>in vitro</i> characterization	60
2.5.4 Dissociated rat cortical neuron culture preparation	64
2.5.5 Electrophysiology and cytosolic Ca ²⁺ imaging of GCaMP6s and ncpGCaMP6s in cultured cortical neurons.....	64
2.5.6 Live cell imaging of bioluminescent Ca ²⁺ indicators in HeLa cells and cultured cortical neurons.....	66
Chapter 3: A genetically encoded near-infrared fluorescent calcium ion indicator	68

3.1 Abstract	68
3.2 Introduction.....	68
3.3 Results and discussion.....	71
3.3.1 Rationale for an insertion-based design	71
3.3.2 Engineering of NIR-GECO1.....	73
3.3.3 Attempted engineering of a smURFP-based GECl	81
3.3.4 <i>In vitro</i> characterization of NIR-GECO1.....	83
3.3.5 Characterization of NIR-GECO1 in dissociated neuron culture....	88
3.3.6 Imaging of <i>in vivo</i> expressed NIR-GECO1	97
3.3.7 Multiplexed imaging of NIR-GECO1 in combination with optogenetic actuators and fluorescent-protein-based indicators.	105
3.4 Conclusion.....	116
3.5 Materials and methods.....	118
3.5.1 General methods and materials.....	118
3.5.2 Engineering of NIR-GECO1.....	118
3.5.3 NIR-GECO1 expression vectors.....	120
3.5.4 Protein purification and <i>in vitro</i> characterization	121
3.5.5 Two-photon spectral measurements.....	123
3.5.6 Animal care.....	124
3.5.7 Imaging of NIR-GECO1 in HeLa cells and dissociated neuron cultures	125
3.5.8 Electrophysiology and Ca ²⁺ imaging in dissociated hippocampal neurons	129
3.5.9 Multiplexed live-cell imaging with NIR-GECO1 in MIN6 β-cells..	130
3.5.10 <i>In utero</i> electroporation.....	131
3.5.11 Acute brain slice preparation	132
3.5.12 Concurrent electrophysiology and Ca ²⁺ imaging in acute brain slice	132
3.5.13 <i>In vivo</i> two-photon microscopy.....	133
3.5.14 <i>In vivo</i> meso-scale imaging.....	135

3.5.15 Statistics and reproducibility	141
Chapter 4: Improved genetically encoded near-infrared fluorescent calcium ion indicator for <i>in vivo</i> imaging	142
4.1 Abstract	142
4.2 Introduction.....	142
4.3 Results and discussion.....	145
4.3.1 Engineering and <i>in vitro</i> characterization of NIR-GECO2.....	145
4.3.2 Characterization of NIR-GECO2 in cultured mouse hippocampal neurons and in acute mouse brain slices.....	150
4.3.3 Imaging neural activity in <i>C. elegans in vivo</i> using NIR-GECO2	152
4.3.4 Development of NIR-GECO variants with blue-shifted spectra. .	155
4.4 Conclusion.....	158
4.5 Materials and methods	159
4.5.1 General methods and materials.....	159
4.5.2 Construction of miRFP-based Ca ²⁺ indicator prototype.....	159
4.5.3 Engineering of NIR-GECO2 and design of blue-shifted NIR-GECO2 variant	160
4.5.4 Protein purification and <i>in vitro</i> characterization	160
4.5.5 Imaging of miRFP-based Ca ²⁺ indicator prototype in HeLa cells	161
4.5.6 Imaging of NIR-GECO2 in dissociated hippocampal neurons	162
4.5.7 Imaging of NIR-GECO2 in acute brain slice	163
4.5.8 Ca ²⁺ imaging in <i>C. elegans</i>	163
Chapter 5: Conclusion and future direction	165
5.1 Summary of the thesis.....	165
5.2 LUCI-GECO: general perspective and future directions	167
5.3 NIR-GECO: general perspective and future directions.....	169
References	172

List of Tables

Table 2.1. Biophysical properties of purified GCaMP6s and ncpGCaMP6s	48
Table 3.1. Summary of fluorescence intensity and fluorescence response to Ca^{2+} when CaM-RS20 were inserted to various sites of mIFP.....	73
Table 3.2. Spectral, photochemical and biochemical properties of NIR-GECO1 in comparison with iRFP682, miRFP, GCaMP6s and GCaMP3.....	86

List of Figures

Figure 1.1. Structures of mTagBFP (PDB ID: 3M24), GFP (PDB ID: 1MEA), mCherry (PDB ID: 2H5Q), and their respective chromophores.	4
Figure 1.2. Chromophores of phytochromes.	5
Figure 1.3 Domain structure and chromophore configuration of phytochromes. ..	7
Figure 1.4. Crystal structures and corresponding chromophores of three types exogenous chromophore-binding fluorescent proteins.	10
Figure 1.5. Schematic representation of FP-based genetically-encoded indicators.	18
Figure 1.6. Naturally existing luciferase-luciferin bioluminescent pairs.	19
Figure 1.7 Novel Luciferase-Luciferin pairs with bright bioluminescence.	24
Figure 1.8. Different types of bioluminescent indicators.	27
Figure 1.9. Optogenetic tools are divided into two categories: optogenetic actuators for perturbation and optogenetic indicators for observation.	30
Figure 1.10. Spatial separation of optogenetic actuators and indicators.	35
Figure 2.1. Engineering and <i>in vitro</i> characterization of ncpGCaMP6s.	43
Figure 2.2. Absorbance spectra of GCaMP6s and ncpGCaMP6s.	45
Figure 2.3. ncpGCaMP6s has higher BRET efficiency, as a bioluminescent acceptor, than GCaMP6s when fused to NanoLuc luciferase.	46
Figure 2.4. Comparison of GCaMP6s and ncpGCaMP6s in cultured dissociated cortical neurons.	49
Figure 2.5. Design and <i>in vitro</i> characterization of LUCI-GECO1.	52
Figure 2.6. Amino-acid-sequence of LUCI-GECO1.	52
Figure 2.7. LUCI-GECO1 expressed in HeLa cells and its response to Ca ²⁺	55
Figure 2.8. LUCI-GECO1 is sensitive to Ca ²⁺ concentration changes in dissociated rat cortical neurons.	57
Figure 3.1. Design and Structure of mIFP-based GECl.	74
Figure 3.2. Directed evolution of NIR-GECO1 by library screening.	77
Figure 3.3. Lineage of improved NIR-GECO variants.	79

Figure 3.4. Sequence alignment of NIR-GECO1 and mIFP.....	80
Figure 3.5. Attempted engineering of a smURFP-based Ca ²⁺ indicator.....	82
Figure 3.6. <i>In vitro</i> characterization of NIR-GECO1.....	84
Figure 3.7. Brightness and photostability of NIR-GECO1 compared to iRFP682 and miRFP.	89
Figure 3.8. Increasing intracellular BV concentration has a modest effect on NIR-GECO1 brightness.	91
Figure 3.9. Representative traces of single trial NIR-GEO1 fluorescence responses to field stimulation in cultured mouse hippocampal neurons.	93
Figure 3.10. Quantification data of NIR-GEO1 fluorescence responses to field stimulation in cultured mouse hippocampal neurons.	94
Figure 3.11. Fluorescence-response comparison of NIR-GECO1, NES-NIR-GECO1 and GCaMP6s in cultured mouse hippocampal neurons.	95
Figure 3.12. Co-expression of NIR-GECO1 and GCaMP6s in cultured rat cortex neurons.	97
Figure 3.13. Characterization of NIR-GECO1 in intact brain tissues using whole-cell-patch clamp electrophysiology.....	98
Figure 3.14. Characterization of NIR-GECO1 in intact brain tissues under pharmacological stimulation.	99
Figure 3.15. <i>In vivo</i> mesoscale imaging of footshock responses in mice using NIR-GECO1.....	101
Figure 3.16. Control experiments for <i>in vivo</i> mesoscale imaging using GCaMP6s and miRFP.	103
Figure 3.17. Two photon imaging of NIR-GECO1 with GCaMP6f in cultured mouse hippocampal neurons.	106
Figure 3.18. Two-photon fluorescence microscopy of NIR-GECO1.....	108
Figure 3.19. Combined use of CoChR and NIR-GECO1 in acute brain slices for optogenetic stimulation and imaging of activity.	110
Figure 3.20. Combined use of CoChR and NIR-GECO1 in cultured neurons for optogenetic stimulation and imaging of activity.	111

Figure 3.21. Combined use of CheRiff and NIR-GECO1 in cultured neurons for optogenetic stimulation and imaging of activity.	112
Figure 3.22. Multi-color imaging of NIR-GECO1 in combination with AKAR4 and Pink Flamingo.	115
Figure 3.24. Multi-color imaging of NIR-GECO1 in combination with GCaMP6f and RCaMP1.07.	116
Figure 4.1 Ca ²⁺ indicator prototype based on mRFP.	146
Figure 4.2. Alignment of amino acid sequences of mRFP and miRFP.	147
Figure 4.3 Sequence alignment of NIR-GECO2 and NIR-GECO1.	149
Figure 4.4 <i>In vitro</i> characterization of NIR-GECO2.	150
Figure 4.5. NIR-GECO2 in cultured mouse hippocampal neurons.	151
Figure 4.6. All-optical electrophysiology in acute mouse slice using NIR-GECO2 and CoChR.	152
Figure 4.7. Imaging neural activity in the <i>C. elegans</i> using NIR-GECO2 and NLS-jGCaMP7s.	154
Figure 4.8. Rational design of blue-shifted NIR-GECO2.	157

List of Abbreviations

4-AP	4-aminopyridine
ACSF	Artificial cerebrospinal fluid
Arch	Archaeorhodopsin
ATP	Adenosine triphosphate
BFP	Blue fluorescent protein
BiFC	Bimolecular fluorescence complementation
B-PER	Bacterial protein extraction reagent
BphP	Bacterial phytochrome photoreceptor
BRET	Bioluminescence resonance energy transfer
BV	Biliverdin
CaM	Calmodulin
cAMP	Cyclic adenosine monophosphate
<i>C. elegans</i>	<i>Caenorhabditis elegans</i>
CFP	Cyan fluorescent protein
CCD	Charge-coupled device
ChR	Channelrhodopsin
cp	circularly permuted (or circular permutation)
ddFP	dimerization-dependent fluorescent protein
DIV	Days <i>in vitro</i>
DMD	Digital micromirror device
DMEM	Dulbecco's modified Eagle medium
EC (or ϵ)	Extinction coefficient

<i>E. coli</i>	<i>Escherichia coli</i>
EDTA	Ethylenediaminetetraacetic acid
EGFP	Enhanced green fluorescent protein
EGTA	Ethylene glycol tetraacetic acid
Em	Emission
Ex	Excitation
FBS	Fetal bovine serum
FLINC	Fluorescence fluctuation increase by contact
FMN	Flavin mononucleotide
FP	Fluorescent protein
FpFP	FMN-binding fluorescent protein
FRET	Förster resonance energy transfer
GAF	cGMP phosphodiesterases/adenylyl cyclases/ FhIA transcriptional activator
GECI	Genetically-encoded Ca ²⁺ indicator
GECO	Genetically-encoded Ca ²⁺ indicator for optical imaging
GFP	Green fluorescent protein
Gly	Glycine
GTP	Guanosine triphosphate
His	Histidine
HHBS	Hank's buffer with hepes
IFP	Infrared-fluorescent protein
iRFP	Near-infrared fluorescent protein

IUE	<i>In utero</i> electroporation
K_d	Dissociation constant
LB	Luria-Bertani
LED	Light-emitting diode
LP	Light-emitting protein
LOV	Light-oxygen-voltage sensing
Luc	Luciferase
mL	millilitre
mm	millimetre
mM	millimolar
MOPS	3-(N-morpholino) propanesulfonic acid
ncp	non-circularly permuted
NES	Nuclear exclusion sequence
NIR	Near-infrared
NLS	Nuclear localization sequence (or signal)
nm	nanometre
nM	nanomolar
NpHR	<i>Natromoas pharaonic</i> halorhodopsin
NTA	Nitrilotriacetic acid
PAS	Per-Arnt-Sim
PBS	Phosphate buffered saline
PCR	Polymerase chain reaction
PCB	Phycocyanobilin

PCM	Photosensory core module
PDB	Protein data bank
PHY	Phytochrome specific
PKA	Protein kinase A
PPI	Protein-protein interaction
PΦB	Phytochromobilin
QY (or Φ)	Quantum yield
RCF	Relative centrifuge force
RFP	Red fluorescent protein
sCMOS	Scientific complementary metal-oxide semiconductor
Ser	Serine
SEM	Error of the mean
SD	Standard deviation
smURFP	small ultra-red fluorescent protein
SNc	Substantia nigra pars compacta
Str	Dorsal striatum
TEA	tetraethylammonium
Tyr	Tyrosine
$t_{1/2}$	half-life
μm	micrometer
μM	micromolar
UV	Ultraviolet
YFP	Yellow fluorescent protein

Chapter 1: Introduction

The discovery and engineering of fluorescent proteins (FPs) has revolutionized the way biologists do research. Not only are FPs every-day tools to visualize cellular structures but they are increasingly being used to create biosensors that enable biologists to visualize dynamic changes of biological activities within cells. In addition to fluorescence, the rapid development of luciferase-based bioluminescence technologies in recent years is now enabling researchers to investigate biological process without the need for external excitation light.

Light-emitting proteins (LPs) including both FPs and luciferases and derivative biosensors are often used for spectrally multiplexed imaging in combination with one or more additional LPs that possesses different color and spectral properties. Spectral multiplexing is not only limited to the use of multiple LPs and biosensors for imaging of biological structures and activities, recently, multiplexing between light-driven optogenetic actuators and light-emitting biosensors has also generated a lot of interest in the field of biological science. There has been particular interest among neuroscientists who aim to uncover the molecular mechanism underlying complex neural dynamics by simultaneous perturbation and measurement of neuronal activity. In this chapter, I will provide an overview of current fluorescence and bioluminescence technologies with focus on the multiplexing between light-emitting sensors and light-driving actuators

1.1 Fluorescent proteins and genetically-encoded fluorescent indicators

1.1.1 β -barrel shaped fluorescent proteins with autogenic fluorophores

β -barrel shaped FPs are considered the “traditional” FPs and are the most abundant and widely-used members of the broad family of FPs. This class of proteins was firstly discovered in the jellyfish *Aequorea victoria* in 1962 by Dr. Osamu Shimomura when he was studying the greenish luminescence of *Aequorea*, which was ultimately found to be due to the combination of green fluorescent protein (GFP) and the blue bioluminescent protein aequorin^{1,2}. Only many years after its initial discovery was the gene encoding GFP finally cloned and sequenced³. Following this key development, GFP rapidly emerged as an unprecedented and widely-used marker of gene expression and protein localization in various biological systems. The utility and acceptance of GFP continued to grow as further improved variants of GFP were engineered⁴⁻⁶.

In the late 1990s, the palette of FPs was greatly expanded when six FPs, homologous to GFP but with fluorescent hues range from cyan to red, were discovered and cloned from reef coral⁷. Intensive protein engineering efforts on one of these proteins, the red fluorescent protein (RFP) from *Discosoma* sp., led to the development of the mFruit (m for monomeric) series with hues that spanned the yellow to far-red region of the optical spectrum⁸⁻¹¹. Another series of β -barrel shape FPs that are now widely used in biological science are the derivatives of eqFP611¹² and eqFP578¹³, both of which are originally from the sea anemone

Entacmaea quadricolor. The engineering of eqFP611 led to the development of monomeric RFP mRuby¹⁴, while engineering of eqFP578 resulted in the generation of blue fluorescent protein (BFP) mTagBFP¹⁵, the RFP mKate¹⁶, and the far-red FP mCardinal¹⁷. As a consequence of extensive protein engineering, the hues of β -barrel FPs cover the whole visible light spectrum, ranging from the ultraviolet (UV) to far-red. Currently, the most blue-shifted β -barrel FP is Sirius with excitation and emission peaks at 355 nm and 424 nm, respectively¹⁸. The most red-shifted β -barrel FP is mNeptune681_Q159N with excitation and emission maxima at 607 nm and 685 nm, respectively¹⁹. Although red-shifted FPs are favorable tools for non-invasive imaging in live animals, because red light has less absorption and scattering in tissue, even the most red-shifted β -barrel FP is outside the optimal imaging window (650 nm - 900 nm) where tissue is the most transparent²⁰. Furthermore, efforts to engineer even more red-shifted (*i.e.*, NIR) β -barrel FPs have not been successful.

As the name “ β -barrel” indicates, all β -barrel FPs shared a conserved β -barrel structure that is formed from 11 β -strands (**Figure 1.1**). Once the β -barrel is folded properly, a specific tripeptide (Ser65-Tyr66-Gly67 for GFP; the residue in position 65 can be different in GFP mutants and homologs) that is contained in the centre helix, undergoes oxygen-involved autocatalytic maturation to form the chromophore that emits fluoresce when excited with visible wavelength light²¹ (**Figure 1.1**). The feature of autogenic chromophore formation appears to be unique in the natural world, and makes β -barrel FPs indispensable genetically encoded tools for modern biological science.

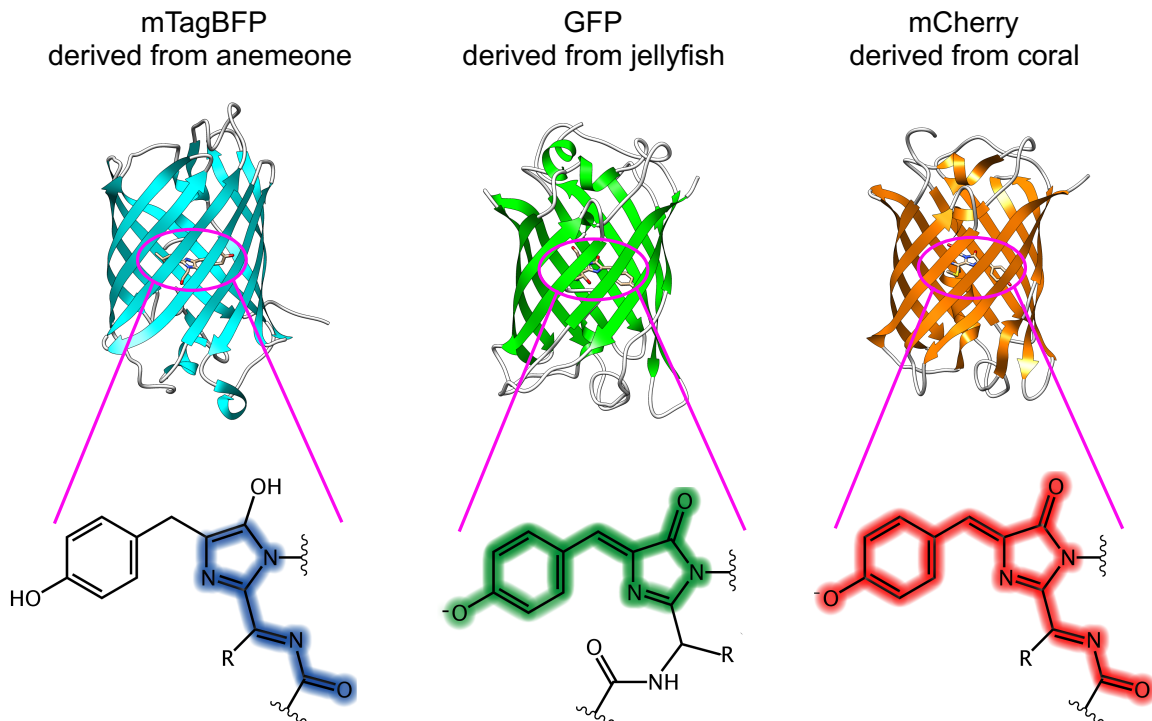


Figure 1.1. Structures of mTagBFP (PDB ID: 3M24), GFP (PDB ID: 1MEA), mCherry (PDB ID: 2H5Q), and their respective chromophores.

1.1.2 Endogenous chromophore-binding fluorescent proteins engineered from natural photoreceptors

Natural photoreceptors are a family of photosensory proteins that exist in bacteria, fungi, cyanobacteria, plants and higher eukaryotes. By absorbing light, photoreceptors transduce light signals to cellular activities via photo-induced conformational changes. Although the light that natural photoreceptors are able to absorb ranges from UV to NIR²¹, those that absorb red to NIR light are of particular interest as potential tools. Specifically, if such proteins could be engineered to be NIR FPs, it would overcome the challenge of expanding the spectra of

aforementioned β -barrel FPs to the NIR region. NIR FPs should be particularly useful for non-invasive deep-tissue imaging because tissue has minimal absorbance and less scattering of light in the NIR range (650 nm – 900 nm), compared to light with shorter wavelength^{20,22}.

Phytochromes, which are proteins that covalently bind to various highly conjugated linear tetrapyrrole bilins as chromophores²³ (**Figure 1.2**), are far-red- and NIR-light-sensing photoreceptors that are good candidates for making NIR FPs.

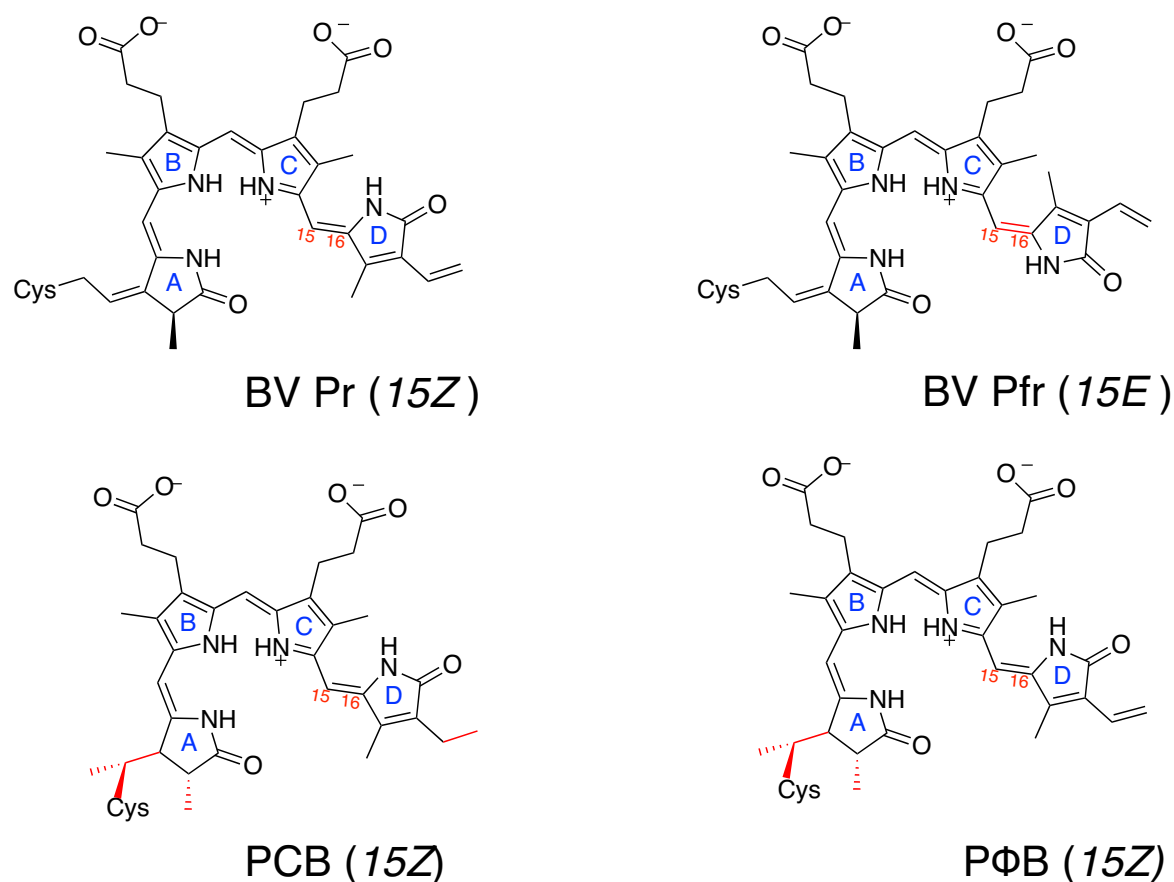


Figure 1.2. Chromophores of phytochromes.

BV (biliverdin) in the Pr (15Z) and Pfr (15E) (chromophore of bacterial and fungal phytochromes); PCB (phycocyanobilin, chromophore of cyanobacterial phytochromes), PΦB (phytochromobilin, chromophore of plant phytochromes), in the Pr (15Z) conformation. Difference relative to BV (15Z) are highlighted in red. Figure is adapted from Ref. 24.

Phytochromes are generally photoswitchable and can exist either in the Pr or Pfr states, which differ due to *Z/E* isomerization around the C15-C16 double bond of the chromophore (**Figure 1.2**)²⁴. Phytochromes in Pr states have been found to exhibit fluorescence with emission peaks at 700 nm – 720 nm²⁵, while the fluorescence of Pfr states of phytochromes have never been successfully detected. Accordingly, to engineer a FP from a phytochrome, the Pr state should be stabilized by abolishing its ability to photoswitch. Structural analysis has revealed that phytochromes share a conserved photosensory core module (PCM) consisting of a PAS domain, a GAF domain and a PHY domain²⁶ (**Figure 1.3**). The PAS domain and the GAF domain are associated with the incorporation and stabilization of the chromophore while the PHY domain plays a key role in photoswitching²⁶⁻²⁹. Thus, discarding PHY domain and site-directed mutagenesis of residues surrounding the chromophore are effective strategies for making the chromophore fluorescent.

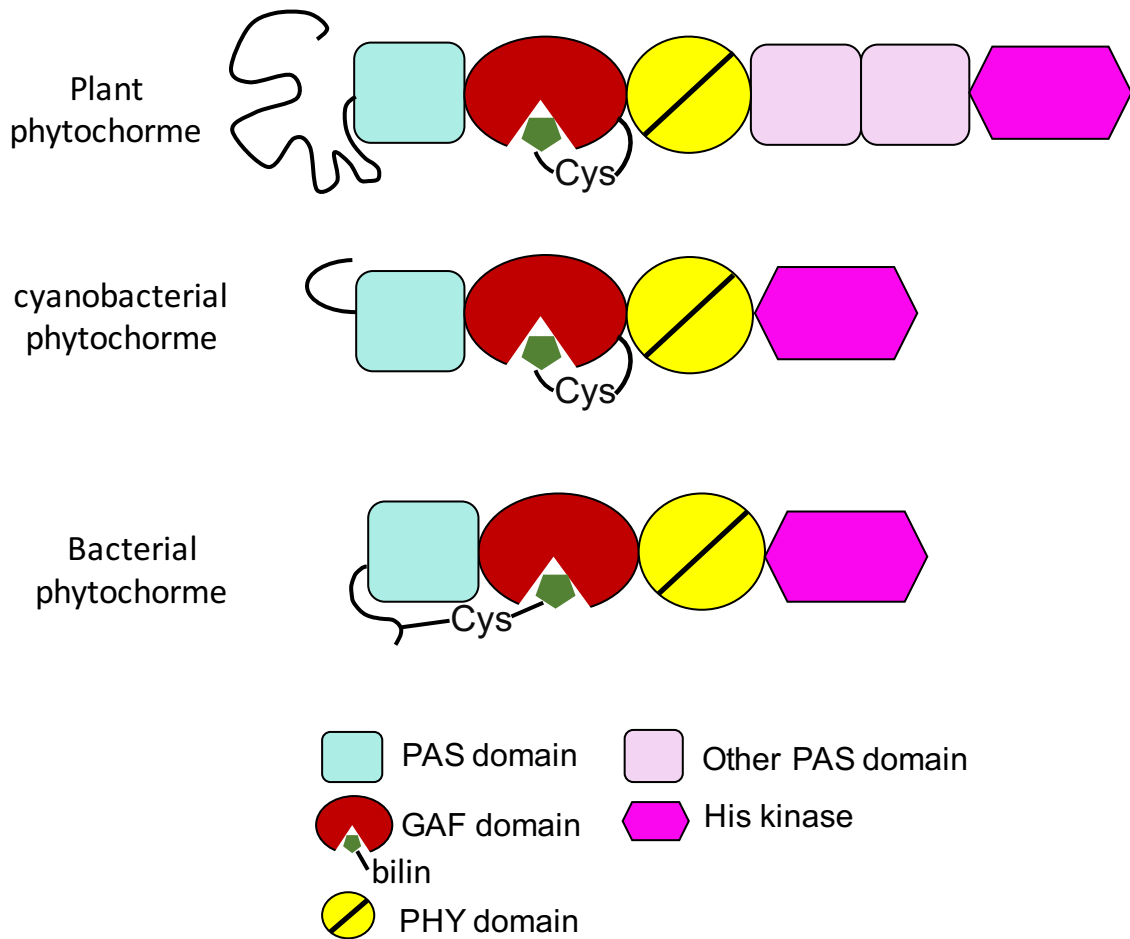


Figure 1.3 Domain structure and chromophore configuration of phytochromes.

Figure is adapted from Ref. 26.

In 2009, a bacteriophytochrome from *Deinococcus radiodurans* (DrBphP), incorporating BV as the chromophore, was engineered into infrared-fluorescent protein 1.4 (IFP1.4) via truncation of PHY domain followed by directed evolution³⁰. IFP1.4 expressed well in mammalian cells and in mouse liver, and was demonstrated very useful for whole-body imaging due to its unique NIR spectral properties (648 nm excitation and 708 nm emission).

As the first example of a NIR FP that could be expressed in mammalian cells, IFP1.4 is self-sufficient to covalently bond to endogenously produced BV and thus its application should be, in principle, no different than conventional β -barrel FPs (*i.e.*, no need to add exogenous BV chromophore). However, neither the *in vitro* brightness nor BV binding ability of IFP1.4 was good enough for *in vivo* imaging and administration of BV was often required³⁰. Later in 2011, an improved NIR FP iRFP³¹ (renamed to iRFP713 in 2013) was reported. iRFP was brighter and more effectively bound to endogenous BV than IFP1.4, such that administration of exogenous BV was not necessary to make it fluorescent in cells, tissues, and whole animals.

Following the development of iRFP, many other NIR and far-red FPs were published such as bacteriophytochrome (BphP)-based Wi-Phy³², IFP2.0 (Ref. 33), the iRFP series³⁴ and cyanobacterial allophycocyanin-based smURFP³⁵. All of the proteins mentioned above were either dimeric proteins or have a tendency to dimerize at high concentrations. Attempts to develop truly monomeric far-red and NIR FPs led to the development of BphP-based mIFP³⁶, the mIRFP series^{37,38}, and the recently published mIRFP670nano, which was derived from a cyanobacteriochrome (CBCR)³⁹. Although monomeric NIR FPs are more favorable for protein tagging and development of NIR reporters, they are substantially dimmer in neurons and *in vivo* than dimeric NIR FPs. Of all the dimeric NIR FPs currently available, iRFP713 and iRFP682 are the brightest two when expressed in mammalian brain *in vivo*⁴⁰. In summary, phytochrome derived far-red and NIR

FPs are an important complement to the β -barrel FPs and many of them are now widely used in protein and cell labeling.

In addition to BV-binding FPs, there are other endogenous-chromophore binding proteins such as flavin mononucleotide (FMN)-binding FPs (*i.e.*, FpFPs)⁴¹ and the bilirubin-binding FP (*i.e.*, UnaG)⁴² (**Figure 1.4**). FpFPs were engineered from light-oxygen-voltage-sensing (LOV) domains of bacterial and plant photoreceptors. These proteins become green fluorescent only after non-covalently binding to FMN. The advantages of FpFPs over GFP-like β -barrel FPs include oxygen-independent fluorophore formation⁴¹, which is especially useful for applications under anaerobic conditions, and a relative small size (about 100 amino acids). FpFPs have been shown to have advantages relative to GFP as a reporter for viral movement in plants⁴³. UnaG is another type of green FP, which was discovered in Japanese eel muscles and is the first known FP from a vertebrate organism⁴². This 139-amino acid protein non-covalently binds to bilirubin with high affinity and specificity. One interesting application of this protein is for rapid and easy measurement of bilirubin in clinical blood samples⁴².

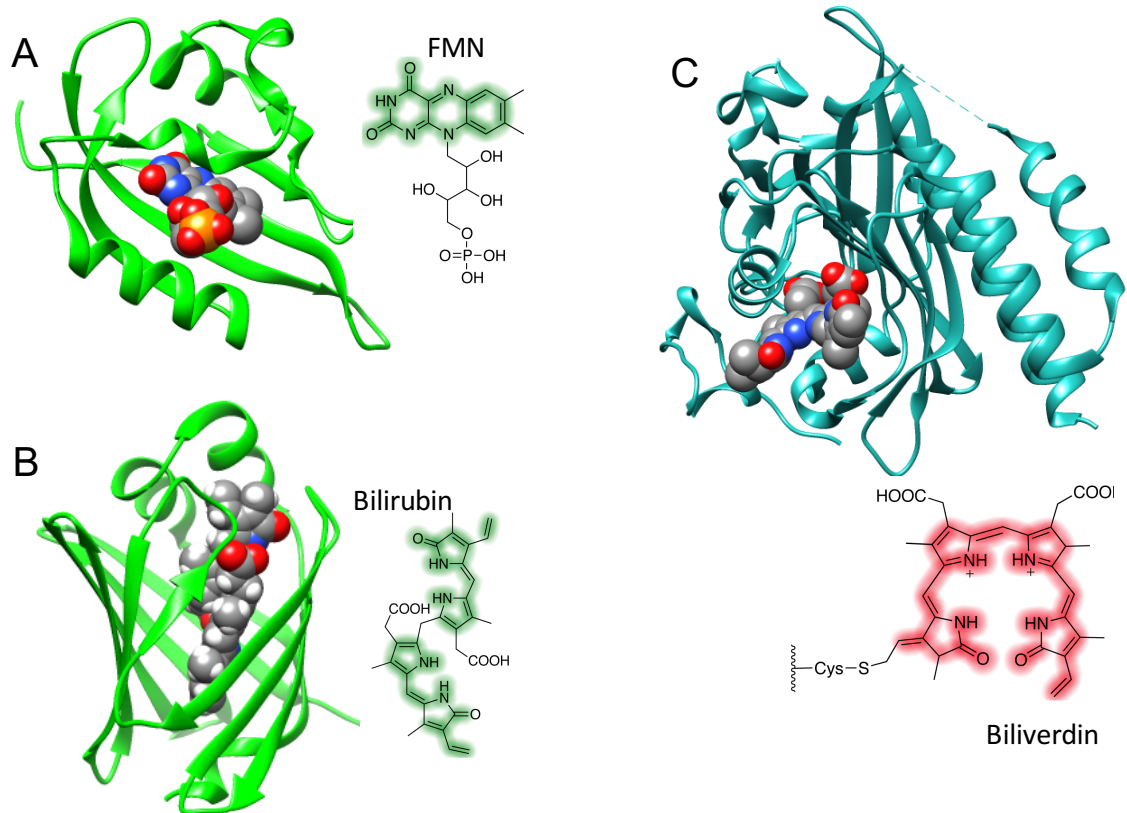


Figure 1.4. Crystal structures and corresponding chromophores of three types exogenous chromophore-binding fluorescent proteins.

(A) FMN-binding FPs FbFPs (PDB ID: 4EET). (B) Bilirubin-binding FP UnaG (PDB ID: 4I3B). (C) BV-binding FPs (e.g., IFP1.4 and iRFP; PDB ID: 2O9B). Figure is adapted from Ref. 216

In summary, these endogenous chromophore-binding FPs are engineered from protein domains of natural photoreceptors that incorporate ubiquitously present cellular metabolites as the chromophores. They are an important addition to the family of FPs and could be applied to some areas that traditional β -barrel FPs cannot be applied to.

1.1.3 Genetically-encoded fluorescent indicators based on fluorescent proteins

In addition to functioning as fluorescent markers of protein localization and organelle structure, FPs have been engineered to be indicators to monitor a wide variety of biological process with high spatial and temporal resolution. Generally, a genetically-encoded fluorescent indicator consists of a recognizing moiety that is able to sense a certain biological analyte or event and a reporting moiety (*i.e.*, an engineered FP) that transduces the signal received from the recognizing moiety to a fluorescence-intensity or color change. Depending on the number of FP molecules involved, genetically-encoded fluorescent indicators can be categorized into following two sub-types: Single FP-based indicators and multiple FP-based indicators.

1.1.3.1. Single FP-based indicators

FP-only indicators

FP-only indicators were first engineered by virtue of the fact that an FP itself can be sensitive to some small ions due to its inherent structural and chemical properties (**Figure 1.5A**). One of the typical examples of this type of indicators are the GFP-based pH indicator known as pHluorins⁴⁴, whose fluorescence changes due to the pH change-induced protonation and deprotonation of the chromophore

phenolate (or phenol respectively) group. In addition to pH indicators, GFP has also been engineered to be the low-affinity calcium ion (Ca^{2+}) indicator, CatchER⁴⁵, by mutation of residues near the chromophore to form a Ca^{2+} binding site. Accordingly, this protein undergoes Ca^{2+} -dependant rearrangement of the β -barrel leading to stabilization of the chromophore and thus increased fluorescence. Another two examples are halide ion indicators based on YFP variants with halide binding sites close to the chromophore⁴⁶⁻⁴⁸, and engineered GFP variants with modifications on the surface of the β -barrel that are sensitive to redox potential^{49,50}.

The FP-only design strategy is not very generalizable because there are only a small number of cellular analytes and biological processes that can directly interact with a FP such that a change in fluorescence intensity results.

GCaMP-type indicators with external modulation

A more universal strategy for developing FP-based indicators is to fuse external sensing domains with topologically rearranged FPs at sites that are spatially adjacent to the chromophore (**Figure 1.5B**). In this type of indicator, external sensing domain undergoes a substantial conformational change after binding to a specific analyte or being induced by a certain biological event, which will result in a modulation of microenvironment surrounding the chromophore and a change of fluorescence intensity or color. The prototypical example of this type of indicator is the Ca^{2+} indicator GCaMP⁵¹⁻⁵³, in which Ca^{2+} sensing domain calmodulin and calmodulin binding peptide RS20 were fused to the C- and N-termini of circularly-permuted GFP, respectively. In the Ca^{2+} free state, Ca^{2+} -

unbound calmodulin and RS20 do not interact, exposing the chromophore of GFP to solvent thus only dim fluorescence emits from GFP. In the Ca^{2+} bound state, Ca^{2+} -bound calmodulin binds to RS20 and the resulting conformational changes leads to stabilization of the chromophore and increase of green fluorescence. Following the example of GCaMP, many other indicators have been engineered based on similar strategies⁵⁴. Those indicators were made by swapping the sensing domain to detect different biochemical signals, or substituting GFP with other hues of FP to expand the palette of genetically-encoded indicators.

BiFC-based indicators

Another strategy for developing indicators involves splitting a FP into two separate and non-fluorescent fragment polypeptides, which can reconstitute to a whole FP and become fluorescent when brought to a close proximity (**Figure 1.5C**). This design is known as bimolecular fluorescence complementation (BiFC). Split FP fragments are generally connected to putative interaction protein partners to detect sub-cellular protein-protein interactions⁵⁵ or to screen protein-protein interaction partners in high-throughput^{56,57}. Other reported applications include monitoring G protein-coupled receptor (GPCR) activation in human cells^{58,59}, visualization of newly synthesized proteins⁶⁰, and small-molecule drug discovery⁵⁸. Although the versatility of this type of indicators have been demonstrated, they do suffer from inherent and widely-recognized drawbacks. Those drawbacks include irreversibility of the complementation for most examples of this type of indicators,

poor folding, undesired aggregation, and interaction-independent complementation.

1.1.3.2. Multiple FP-based indicators

FRET-based indicators

Förster resonance energy transfer (FRET) is arguably the single most effective strategy for the development of genetically-encoded indicators. In this strategy, a sensing domain is inserted between a donor FP and an acceptor FP. The conformational change or cleavage of the sensing domain induced by a certain biochemical event will affect the distance and/or relative orientation of the FP pair and cause a change in the non-radiative energy transfer efficiency (**Figure 1.5D**). Non-radiative energy transfer efficiency can be quantified using either steady-state measurements or lifetime measurements⁶¹. In steady-state FRET, there is an increase in the ratio of acceptor emission to donor emission when FRET efficiency increases, and a decrease when it decreases. For lifetime measurements, there is a decrease in donor lifetime when FRET efficiency increases, and an increase in donor lifetime when it decreases⁶¹.

Among all the FRET-based indicators, the pair of cyan fluorescent protein (CFP) with yellow fluorescent proteins (YFP) are the most common FPs used. However, with the extensive engineering of FPs, many other FP pairs now offer distinct advantages for FRET. For example, the mClover-mRuby2 pair substantially improves photostability⁶², the mCyRFP-mMaroon pair enables

simultaneous imaging of FRET indicators with green fluorescent indicators⁶³, and the miRFP670-miRFP720 pair provides opportunities for combining optogenetic actuators and FRET-based indicators⁶⁴ with reduced spectral crosstalk.

Overall, FRET-based indicators have equipped scientists with a powerful set of molecular tools. There are some drawbacks however, including their larger size, often low signal-to-noise ratio (SNR), and more complex requirements for microscope setups⁶⁵ compare to single FP-based indicators.

ddFP- and FLINC-based indicators

Dimerization-dependant FPs (ddFP) were first reported in 2012 as an alternative technology to BiFC and FRET for monitoring protein-protein interaction and dynamics activities⁶⁶. Instead of structurally splitting one FP or recruiting two spectrally distinct FPs, Alford and co-workers engineered a low-affinity dimeric FP pairs that fluoresced when each pair were brought into sufficiently close proximity to interact and form a more brightly fluorescence heterdimer⁶⁶⁻⁶⁸ (**Figure 1.5E**). This approach provides new opportunities for making genetically-encoded intensimetric indicators such as a recently published small GTPase sensor⁶⁹ and a kinase sensor⁷⁰.

Similar to ddFPs, FLINC (fluorescence fluctuation increase by contact) also takes advantage of binding-induced fluorescence changes (**Figure 1.5F**). Specifically, Mo and colleagues found that the red FP TagRFP-T⁹ exhibited significant fluorescence fluctuation (*i.e.*, blinking) when the photoswitchable green FP Dronpa⁷¹ was in close proximity. The fluorescence fluctuation was induced by

the residues on the barrel surface of Dronpa instead of its chromophore. This distance dependent blinking phenomenon enabled the development of a new class of kinase indicators for visualizing PKA activities at super-resolution⁷².

Together, genetically-encoded fluorescent indicators continue to provide valuable insights into the signaling network, metabolic regulation and other molecular dynamic that govern cell function, accelerating progress towards an improved understanding of cell biology.

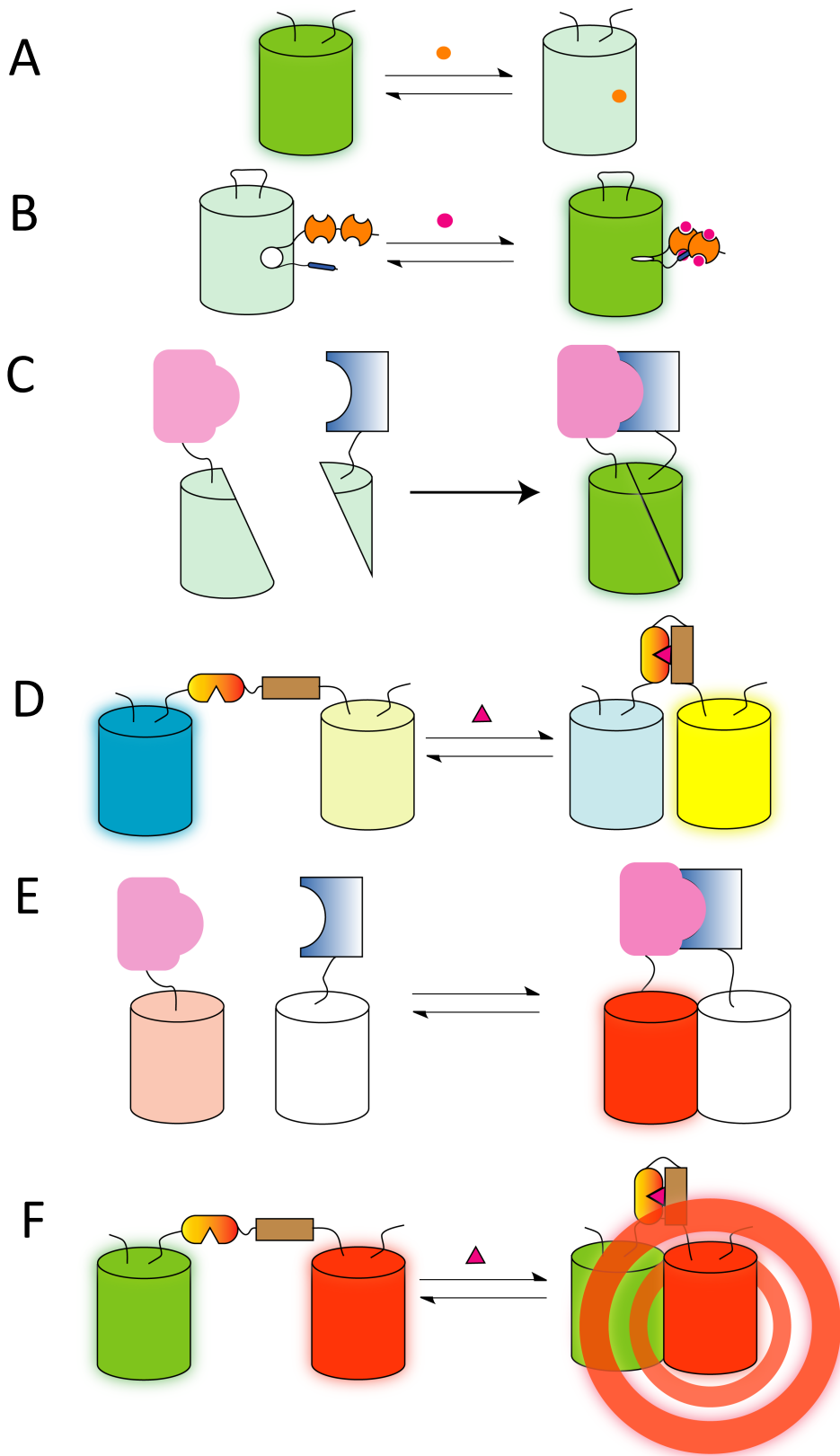


Figure 1.5. Schematic representation of FP-based genetically-encoded indicators.

(A) FP-only indicators. *i.e.*, The fluorescence of GFP variant pHluorins decreases upon binding to H⁺. (B) GCaMP-type indicators with external modulation. In the case of GCaMP, Ca²⁺-dependant conformational change dramatically increases green fluorescence. (C) BiFC. Two non-fluorescent GFP fragments regain fluorescence when brought together by protein-protein interaction. (D) FRET-based indicators. The excitation energy from CFP (donor) is transferred YFP (acceptor) via dipole-dipole interaction when the distance and orientation are in the favor of FRET. (E) ddFP. When in proximity to its non-fluorescent partner ddFP-B, dimly fluorescent ddFP-A becomes substantially brighter. (F) FLINC. The fluorescence of TagRFP-T (red) fluctuates upon binding with Dronpa (green).

1.2 Bioluminescent proteins and indicators

1.2.1 Bioluminescence

Bioluminescence is very common among living organisms. In addition to the familiar yellow-light emitting fireflies, many other organisms such as fungi, algae, and 76% of deep-ocean creatures⁷³ were also reportedly bioluminescent. Although the reasons for that why those organisms emit light are various, ranging from attracting prey, to attracting mates, to protecting themselves from predators, the chemical principles behind those luminescence are very similar. Specifically, proteins called luciferases catalyze the oxidation of chemicals (*i.e.*, D-luciferin,

coelenterazine) to form products in the excited state when they then emit light through an electronic transition (**Figure 1.6**). Due to the lack of external light for excitation compared to fluorescence, bioluminescence has some advantages for imaging applications: negligible phototoxicity, much lower background signal, and ability to be detected deeper within tissue. These advantages make it a great imaging tool for reporting biological processes.

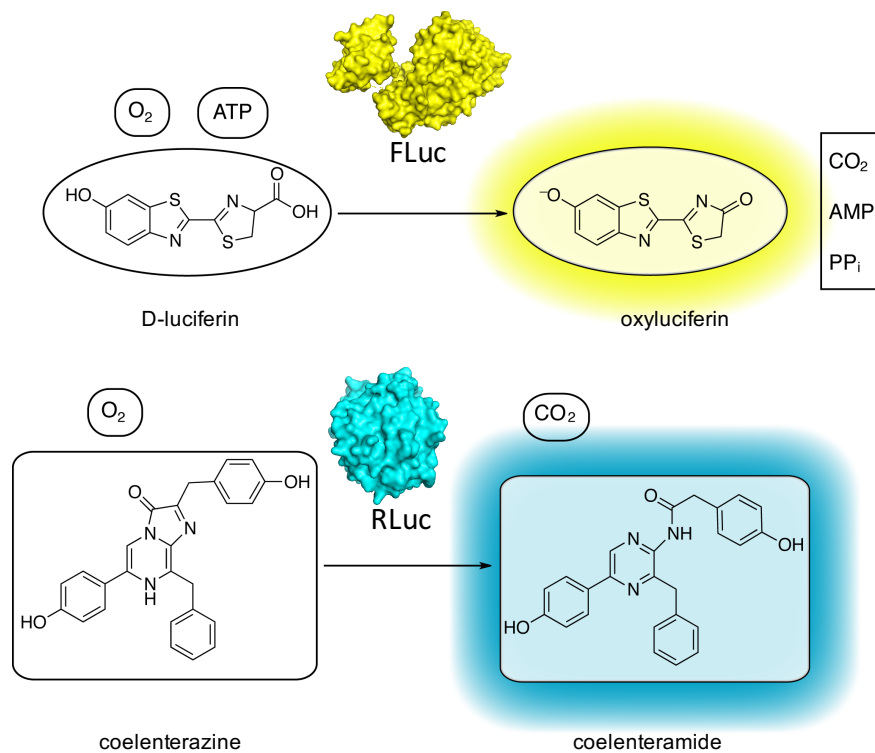


Figure 1.6. Naturally existing luciferase-luciferin bioluminescent pairs.

D-luciferin is oxidized by firefly luciferase (FLuc) to produce oxyluciferin and yellow light. Coelenterazine is another common luciferin that is oxidized by luciferases from a variety of marine organisms such as *Renilla* luciferase (RLuc). Unlike D-

luciferin, the light-emitting process of coelenterazine to coelenteramide requires no ATP as a cofactor and generates cyan light instead of yellow light.

1.2.2 Luciferase

Luciferases play central role in the production of bioluminescence. In 1985, Wet and colleagues successfully cloned the gene for luciferase from the firefly *Photinus pyralis* for the first time⁷⁴. Since then, firefly luciferase (Fluc) has been used as a reporter in cell cultures and small animals⁷⁵. Fluc is one of the most well-studied luciferases with a protein size of 62 kDa (550 a.a.) and emission peak at 562 nm. Fluc requires beetle D-luciferin (benzothiazole) as its substrate, ATP and Mg^{2+} as cofactors. Later, in 1991 and 2005, luciferases from the sea pansy *Renilla reniformis* (RLuc)⁷⁶, and copepod marine organism *Gaussi princeps* (GLuc)⁷⁷, were cloned, characterized, and used in biomedical research ever since. Compare to Fluc, RLuc and GLuc have smaller sizes (36 kDa and 19.9 kDa, respectively), utilize coelenterazine instead of D-luciferin as substrates, and are ATP independent enzymes. Those advantages made RLuc and GLuc more appropriate for use as bioluminescent fusion tags. However, the inherently weak bioluminescent signal produced by those luciferases, and limited color variants, hindered their wide usage for live imaging. To overcome the intrinsic drawbacks of bioluminescence, three strategies have been used to improve the performance of luciferases, including directed evolution, bioluminescence resonance energy transfer (BRET), and development of new luciferase-luciferin pairs.

Improving luciferase brightness using directed evolution

Directed evolution of a protein is an iterative process that consists of mutagenesis of a specific gene and human-defined functional selection of protein variants that are encoded by the generated gene library, through which proteins with desired traits or functions could be created. Directed evolution of RLuc led to the development RLuc8, a bright variant of RLuc with a 4-fold improvement in light output⁷⁸. In other work, rationally mutating residues in the active pocket of RLuc8 and Fluc led to the engineering of red-shifted luciferase variants^{79, 80}. A major breakthrough in the area of developing a brighter luciferase was in 2012 when NanoLuc (NLuc) from deep-sea shrimp *Oplophorus gracillirostris* was engineered through directed evolution⁸¹. NanoLuc exhibits 150-fold brighter bioluminescence than either FLuc or RLuc when it is paired with a novel substrate, furimazine (**Figure 1.7A**). Because of its small size (19 kDa) and brightness, NLuc rapidly replaced RLuc and GLuc for many biomedical imaging applications and has since been widely used in biological research^{82,83}.

Improving luciferase brightness using BRET

In addition to directed evolution, BRET is another approach that can be used to enhance the brightness of a luciferase. The story of this approach goes back to 1962 when Dr. Osamu Shimomura was studying the greenish luminescence of *Aequorea* jellyfish, which he found to be due to the combination of GFP and the luciferase aequorin. In the jellyfish, GFP functioned as a BRET acceptor to increase the emitted photon number. Inspired by this natural intermolecular BRET,

chimeric luminescent proteins BAF-Y⁸⁴ and Nano-lantern⁸⁵ have been generated by fusing Rluc8 to high quantum yield β -barrel FPs. BAF-Y and Nano-lantern allowed for live-cell imaging with improved spatial and temporal resolution. A similar approach has also been applied to further increase the brightness of NLuc. Five different color variants of NLuc were created by fusing the protein mTurquoise2, mNeonGreen, Venus, mKOk, and tdTomato, respectively⁸⁶. Those color variants either enhanced bioluminescence intensity or red-shifted spectra of NLuc, therefor expanding the scope of bioluminescent tools for biological research.

Improving luciferase brightness by development of new luciferase-luciferin pairs

Luciferins play an equally important role to luciferases in the light-emitting process. Thus, development of novel luciferins is another effective method to improve the performance of bioluminescence technology. In 2013, Iwano *et al.* developed a series of firefly luciferin analogs emitting blue, green, red and NIR light when used as substrates with native Fluc⁸⁷. Among those analogs, Akalumine generated particular interest due to its 675 nm emission maximum and reasonable bioluminescence intensity, which were promising features for improved deep-tissue bioimaging of living animals. However, the poor water solubility of Akalumine limited its uses *in vivo*. To solve this problem, Akalumine-HCl with improved biodistribution was synthesized. The bioluminescence produced by Akalumine-HCl pairing with native FLuc in deep lung metastases in mice enabled imaging with considerable penetration depth and sensitivity⁸⁸. Considering the specificities of luciferases to luciferins, Iwano *et al.* evolved FLuc for improved

activity with Akalumine-HCl, leading to the development of Akaluc, an optimal luciferase for Akalumine-HCl (**Figure 1.7B**). The AkaLuc-Akalumine hydrochloride pair allowed unprecedented non-invasive measurement of neuronal activity in mouse hippocampus, and long-term (more than 1 year) detection of Akaluc-expressed striatal neurons in the brains of freely moving marmosets⁸⁹.

The other efforts to optimize new luciferase-luciferin pairs have led to the development of teLuc-DTZ (Diphenylterazine) pair⁹⁰, which is the brightest luciferase-luciferin pair so far. The teLuc luciferase is engineered from NLuc while DTZ is a derivative of furimazine (**Figure 1.7C**). Some challenges that teLuc-DTZ faces for *in vivo* applications include spontaneous oxidation *in vivo*, short-wavelength emission (~510 nm, ~600 nm when teLuc is fused to CyOFP) and DTZ's poor ability to cross blood-brain barrier.

AkaLuc-Akalumine hydrochloride and teLuc-DTZ are currently the two most promising luciferase-luciferin pairs for bioluminescence imaging. However, it remains unclear if one is superior to the other due to inconsistent results in several experiments⁸⁹⁻⁹¹. As suggested by Yeh *et al.*, researchers should be aware of the advantages and disadvantages of both luciferases and chose the right one accordingly for different experiments.

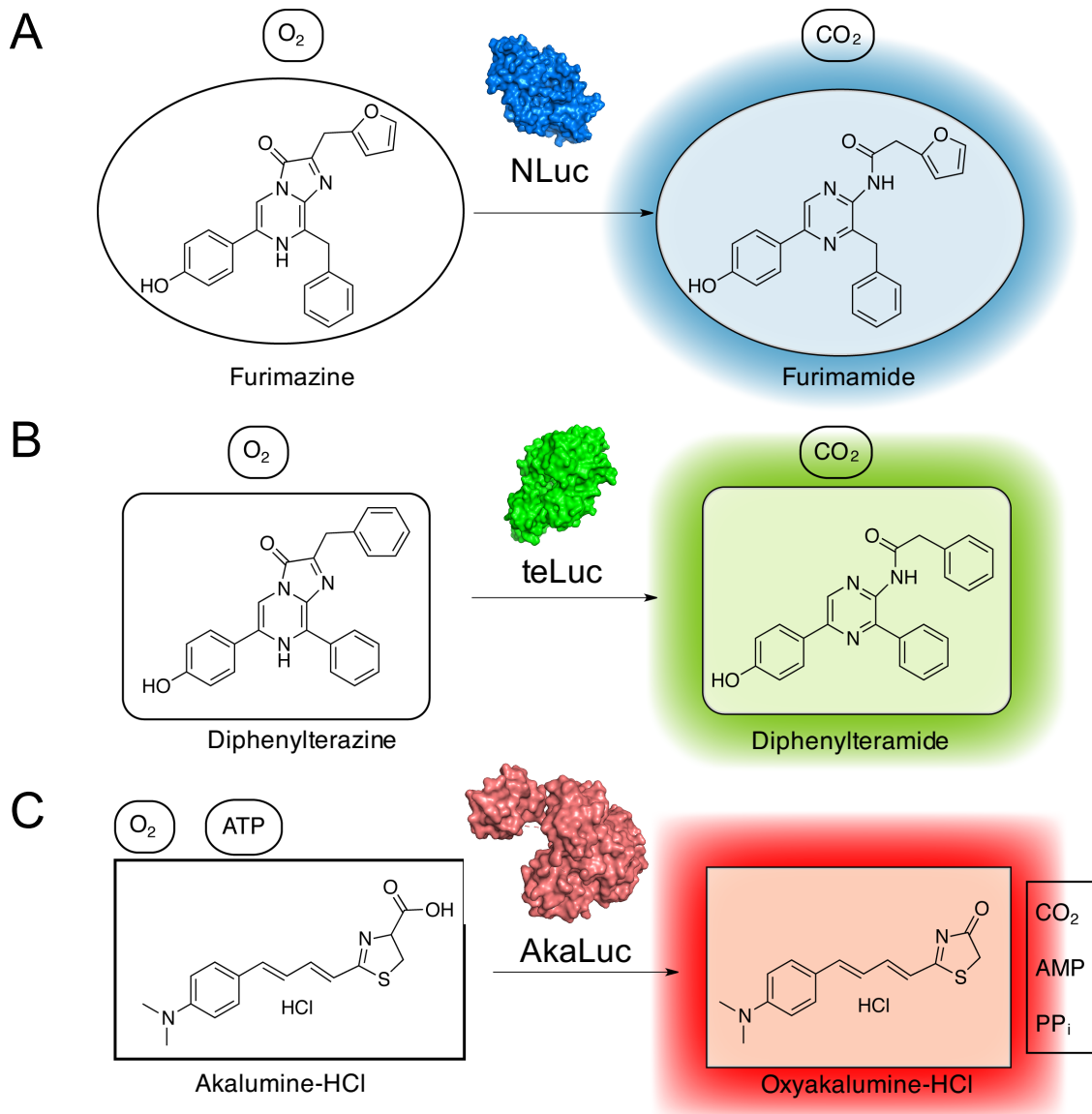


Figure 1.7 Novel Luciferase-Luciferin pairs with bright bioluminescence.

(A) NLuc-furimazine produces 150-fold brighter bioluminescence than RLuc or FLuc does with emission maximum at ~460 nm. (B) The brightest luciferase-luciferin pair to date is teLuc-DTZ with emission maximum at ~510 nm. (C) AkaLuc-Akalumine hydrochloride emits 100 to 1000 times brighter bioluminescence *in vivo* than conventional FLuc-D-luciferin system.

1.2.3 Genetically-encoded bioluminescent indicators

Bioluminescence imaging requires no external light for excitation, thus bioluminescent indicators should be particularly useful for reporting biological events that could be induced or influenced by the use of illumination. Some luciferases can be used as indicators due to their inherent cofactor requirements. For example, ATP is a cofactor of FLuc in the light-emitting reaction, therefore FLuc has been used to report ATP changes in mitochondria and cytosol of cardiac myocytes⁹² due to the positive correlation between ATP concentration and bioluminescence intensity. Similarly, aequorin, a Ca^{2+} dependent luciferase, has been used to investigate intracellular Ca^{2+} activities^{93,94}.

In addition to these naturally existing bioluminescent indicators, researchers have also developed many other bioluminescent indicators. The two most widely used strategies for making bioluminescent indicators are to use reconstitution of split luciferases or BRET. Split luciferases were first used to detect intracellular protein-protein interactions⁹⁵. The principle of split luciferase is similar to that of split FPs. Inactive split fragments, which are fused to two different proteins, will regain activities and produce bioluminescence in the presence of substrate when they are brought into close proximity by the interaction of proteins partners (**Figure 1.6A**). Although split FLuc and RLuc have been used for imaging of protein-protein interactions in live animals^{95,96}, both of them suffer from relatively low sensitivity due to poor signal-to-noise ratio and high background due to intrinsic affinity of the fragments for each other. Ongoing efforts have led to the development of various split luciferase-based protein-protein interaction indicators⁹⁷⁻⁹⁹, and a notable

recent one was based on the bright NLuc¹⁰⁰, which allowed sensitive measurements of protein interactions in cells.

In addition to their use for monitoring protein-protein interaction, split luciferases have also been used to report intracellular dynamic changes of small molecules such as Ca²⁺, cAMP, and ATP. In these type of indicators, split luciferases fragments were connected to each end of a particular sensing domain, whose conformational changes would alter the activity of the luciferase and then alter the real-time light output (**Figure 1.6B**). Bioluminescent Ca²⁺ indicators made from split Rluc with the insertion of CaM-RS20 was reported in 2008 (Ref. 101). In 2012, a similar strategy was reported for Nano-lantern (Rluc8-Venus), from which three bioluminescent indicators were developed for detecting intracellular changes of Ca²⁺, cAMP and ATP by inserting corresponding sensing moieties into Rluc8⁸⁵. Split NLuc has also been engineered to be an intensimetric Ca²⁺ indicator by insertion of CaM-RS20 and fusion to the FP mNeonGreen⁸⁶ or CyOFP¹⁰².

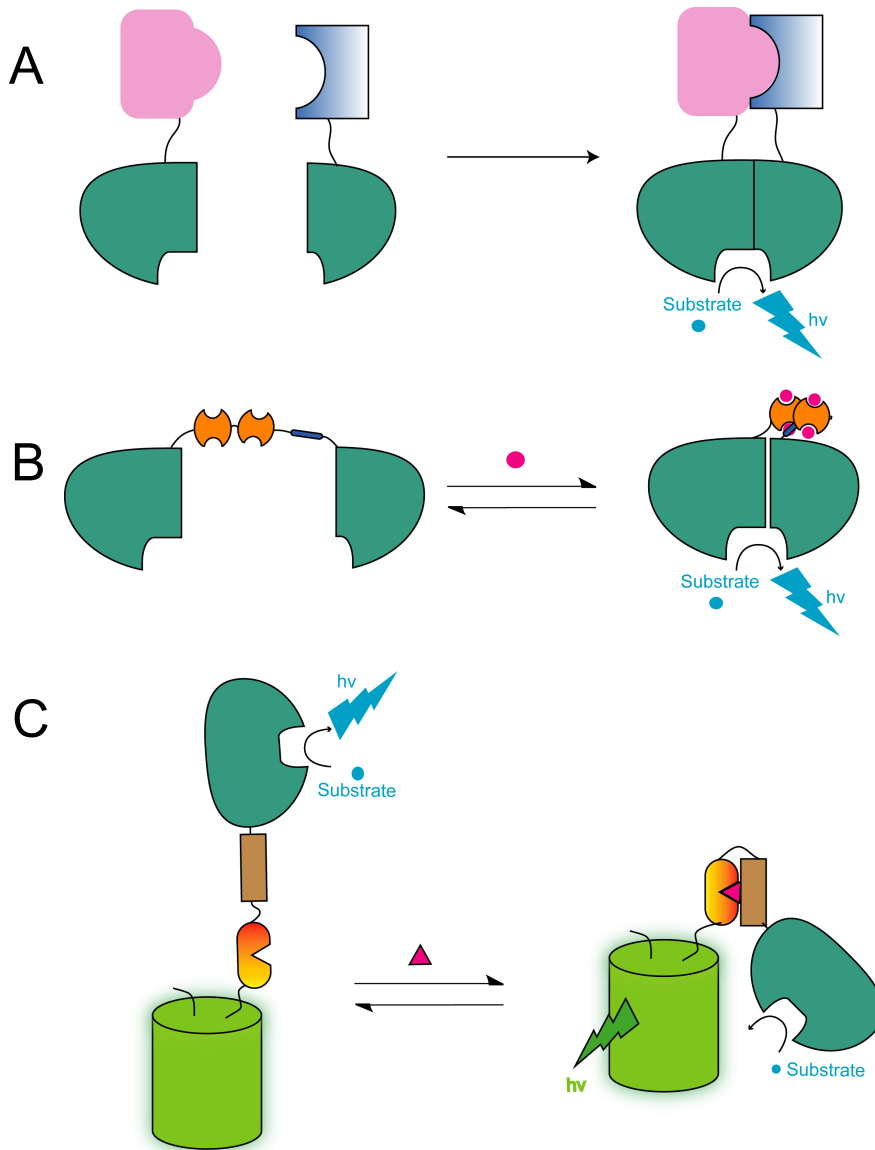


Figure 1.8. Different types of bioluminescent indicators.

(A) Split luciferase-based tools for monitoring protein-protein interactions. (B) Intensimetric bioluminescent indicators based on split luciferases. In this design, N-terminal luciferases are generally fused to a FP to improve QY of emission. (C) BRET-based ratiometric bioluminescent indicators.

BRET, which is fundamentally the same phenomenon as FRET, is a powerful and relatively straightforward method by which to develop bioluminescent indicators. The design of this type of indicators is identical to that of FRET-based fluorescent indicators, with the key difference being that the donor FP is swapped to a spectrally similar luciferase (**Figure 1.8C**). For example, by replacing CFP with NLuc, the Ca²⁺ indicator CalfluxVTN¹⁰³, the voltage indicator LOTUS-V¹⁰⁴, and the ATP indicator BTeam¹⁰⁵, were made based on the design of Twitch¹⁰⁶, Mermaid2 (Ref. 107), and Ateam¹⁰⁸, respectively.

1.3 Multiplexing light-emitting genetically-encoded indicators and light driven-actuators

All living organisms, including even the simplest single-celled organisms, are composed of extremely complicated molecular systems to enable a wide variety of functions and behaviors. Among all the biological systems, the nervous system is the most complicated, especially in mammals, allowing for the capabilities of learning, memory, and complex behaviors. A better understanding of the molecular mechanisms underlying the astonishing complexity of the nervous system could help to uncover the role of dysfunctional neural circuits in brain degenerative diseases and accelerate progress in the burgeoning field of artificial intelligence (AI).

To advance the understanding of the nervous system and brain function, both observational and perturbational technologies are required¹⁰⁹. Over the last two decades, optogenetics, which refers to the combination of optics and genetics, has equipped researches with many tools for non-invasively observing and perturbing cell functions¹¹⁰. Genetically-encoded light-emitting indicators, which are mainly based on FPs and luciferases as described earlier in this chapter, and light-driven actuators that are based on light-activated channels and pumps¹¹¹, are the two main classes of optogenetic tools. Optogenetic indicators can be used to monitor dynamics changes of membrane voltage, intracellular Ca^{2+} concentration, synaptic transmission, and other aspects of cell biology¹¹⁰. Optogenetic actuators can be used to stimulate or silence cells via illumination with specific wavelengths of light¹¹⁰ (**Figure 1.9**). In principle, the combined use of optogenetic indicators and

actuators makes it possible to simultaneously monitor and manipulate biological progress by using only light. However, the spectral and spatial overlap between high-performance indicators and actuators has hampered their simultaneous co-application to date. To solve this problem, researchers have come up with a variety of solutions and technologies, which can be divided into two categories: spectral separation and spatial separation.

Optogenetic

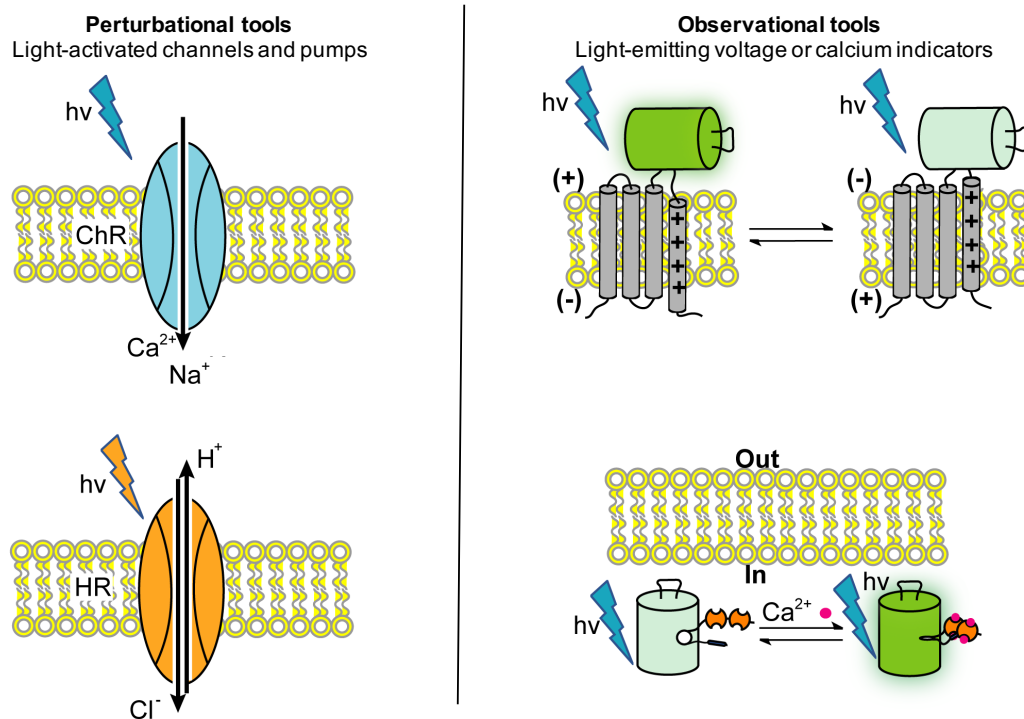


Figure 1.9. Optogenetic tools are divided into two categories: optogenetic actuators for perturbation and optogenetic indicators for observation.

Left, optogenetic actuators. Light-activated ion channels (top) are used to stimulate neural activity while ion pumps (bottom) are used to inhibit neural activity. Right,

two types of optogenetic indicators that are generally used to report neural activity: membranal voltage indicators (top) and cytosolic Ca²⁺ indicators (bottom).

1.3.1 Spectral separation of optogenetic actuators and indicators

The majority of optogenetic actuators which have been widely used to drive neural activity (e.g., channelrhodopsin-2 (ChR2)¹¹², CheRiff¹¹³, and CoChR¹¹⁴) are activated with blue light. Blue light-excited Ca²⁺ and voltage indicators, on the other hand, are frequently used to report neural activity¹¹⁵. The spectral overlap, however, makes it difficult (if not impossible) to avoid activating the actuator when imaging the indicator. Thus, there is a need for both optogenetic actuators and indicators that have been either blue or red shifted to be compatible with each other. Below I list some examples of successful combinations between optogenetic actuators and genetically-encoded indicators for simultaneous perturbing and observing cell activities.

Blue light-activated channelrhodopsins with red light-excited voltage indicators

Archaeorhodopsin 3 (Arch) is a far-red voltage indicator with excitation maximum at 558 nm and emission maximum at ~705 nm¹¹⁶. Due to its broad excitation spectrum, Arch can be imaged with excitation at 640 nm, therefore enabling simultaneous optical control and readout of neuronal voltage when paired with ChR2, which is generally activated with 470 nm illumination¹¹⁷. Intensive efforts to improving both Arch3 and channelrhodopsins led to a technology called Optopatch, which describes the combination of improved Arch variants (QuasArs)

and a blue shifted and sensitive channelrhodopsin (Cheriff). Optopatch enables precise and cross-talk free optical stimulation and optical recoding of neural activity¹¹³.

Yellow/red-light activated channelrhodopsins with blue light-excited GCaMP Ca²⁺ indicator

C1V1 (a red-shifted channelrhodopsin¹¹⁸ with photocurrent peak at ~558 nm), has been used in combination with GCaMP6s¹¹⁹ (an ultra-sensitive green-fluorescent Ca²⁺ indicator) for simultaneous manipulation and readout of activity of multiple neurons *in vivo* in mice under two-photon microscopy^{120,121}. Two-photon stimulation and imaging helped to minimize the optical cross-talk¹²². Chrimson is an even more red-shifted channelrhodopsin with a photocurrent peak at ~600 nm¹¹⁴. The optogenetic strategy of using Chrimson with GCaMP6s in *C. elegans* successfully revealed that the serotonergic neuron NSM is able to sense food after ingestion in a way that does not require synaptic inputs¹²³. In addition, newly developed green-fluorescent dopamine indicators dLight and GRAB_{DA} have been used with Chrimson for deep brain imaging in freely moving mice to detect dopamine release following optogenetic stimulation^{124,125}. bReaChES is another newly developed red-light-activated channelrhopsin with improved trafficking in long-range projections and a high photocurrent¹²⁶. The combination of bReaChES and GCaMP6 has helped neuroscientists to explore the molecular and structural connectivity of brain circuits in mice during behaviors like memory retrieval¹²⁶, social and feeding^{127,128}

Blue-shifted channelrhodopsin with orange-light excited Ca²⁺ indicator

TsChR is the most blue-shifted channelrhodopsin reported to-date¹¹⁴. Starting from TsChR, Farhi *et al.* developed an optimized variant designated as eTsChR¹²⁹ with robust trafficking. Due to the blue-shifted spectrum of eTsChR, the yellow light required for excitation for red-fluorescent Ca²⁺ indicator jRGECO1a¹³⁰ produces only negligible photocurrent from eTsChR. This slight photocurrent is not strong enough to trigger an action potential, thus permitting all-optical manipulation and observation of neural activity by coexpression of eTsChR and jRGECO1a. This combination, in conjunction with wide-area Hadamard microscopy, provided a powerful platform to map neuronal excitability, pharmaceutical responses, and functional connectivity in intact brain tissue¹²⁹.

Channelrhodopsins with bioluminescent indicators

One of the biggest advantages of bioluminescent indicators is that they don't need external excitation. Furthermore, the light output via oxidization of substrates in bioluminescence is generally much too weak to drive channelrhodopsins expressed in the same cell. Together, these features make bioluminescent indicators fully compatible with optogenetic actuators regardless of spectral properties. For example, bioluminescent Ca²⁺ indicator CalfluxVTN have been paired with CheRiff in dissociated neurons for simultaneously stimulating and reporting Ca²⁺ concentration changes in without the need for excitation light¹⁰³. As another example, the bioluminescent voltage indicator LOTUS-V enabled voltage

imaging compatible with two bidirectional optogenetic actuators: the depolarizing tool ChR2 and the hyperpolarizing tool eNphR3.0 (Ref. 111), which were driven by 438 nm and 580 nm illuminations, respectively¹⁰⁴.

1.3.2 Spatial separation of optogenetic indicators and actuators

Another approach for combined use of optogenetic actuators and indicators is to rely on spatial, rather than spectral, separation. That is, optogenetic actuators and indicators can be targeted to different areas of interest and then precise spatially confined illumination of specific areas is used for either stimulation or imaging. One example is the combination of green fluorescent dopamine indicator GRAB_{DA} with yellow-light excited C1V1 in mouse brain *in vivo*¹²⁴. In this example, C1V1 was targeted to dopaminergic neurons in substantia nigra pars compacta (SNc) while GRAB_{DA} was expressed in the dorsal striatum (Str). Projections from activated dopaminergic neurons of SNc will result in dopamine release in Str. By delivering 561 nm and 470 nm LED to SNc and Str, respectively, transient fluorescence increase from GRAB_{DA} in the Str were successfully detected with optogenetic stimulation in C1V1 expressed SNc¹²⁴ (**Figure 1.10a**). In addition to millimetre-level separation (as in the previous example), micrometre-level separation between optogenetic actuators and indicators has also been exploited in culture neurons using digital micromirror devices (DMDs). One such example is a technology called SynOptopatch, in which an optogenetic actuator (soma-localized CheRiff) and optogenetic indicators (soma-targeting QuasAr2, and spine-

enriched jRGECO1a) were exclusively expressed in adjacent neurons for studying synaptic physiology¹³¹. A digital micromirror was used to pattern the yellow light that is required for imaging of jRGECO1a such that the illumination only spanned the dendritic spines of the indicator-expressing neurons. In this way, the yellow light did not stimulate adjacent CheRiff-expressed neurons (**Figure 1.10B**).

Spatially separating optogenetic actuators and indicators provides new opportunities for the combined use of spectrally overlapped actuators and indicators and will continue to become more practical and user friendly with further advances in the technology of optical devices.

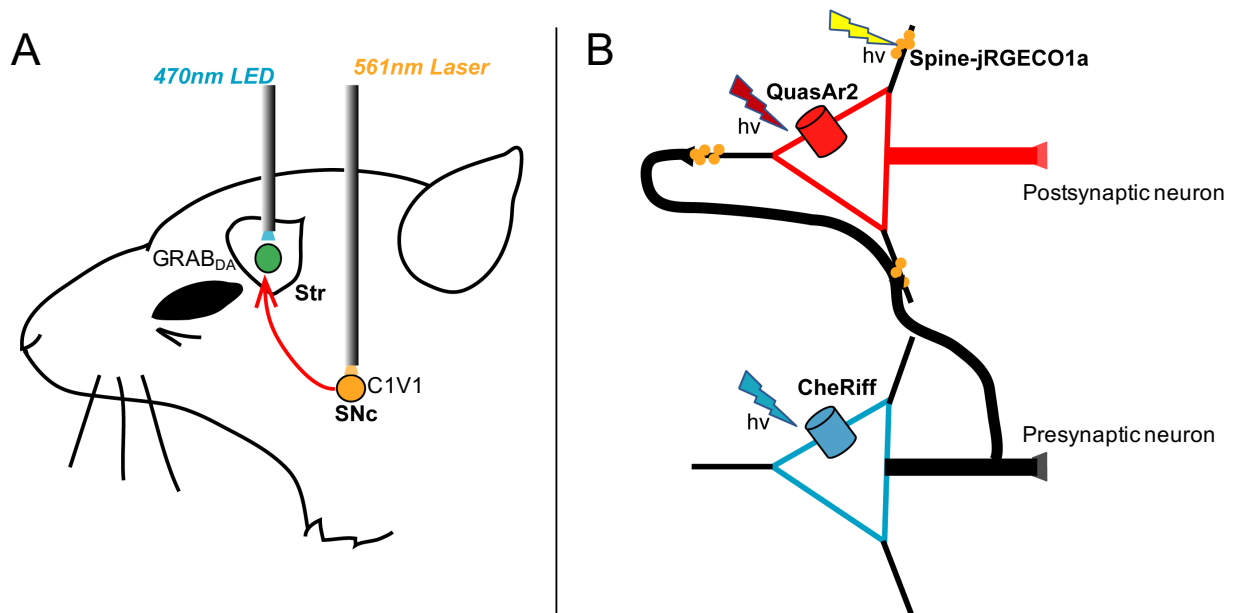


Figure 1.10. Spatial separation of optogenetic actuators and indicators.

(A) Millimeter-level separation in mouse brain. Dopamine indicator GRAB_{DA} and Channelrdopsin C1V1 were targeted to dorsal striatum (Str) and substantia nigra pars compacta (SNc), respectively. 470 nm LED light and 561 nm laser were

delivered to corresponding areas for simultaneous imaging of dopamine dynamics in Str and stimulation of dopaminergic neurons in SNc. Red arrow indicates the projection from SNc to Str. **(B)** Micrometer-level separation. Schematic shows blue light-activated soma-localized CheRiff, yellow light-excitable spine-jRGECO1a, and red-light-excitable QuasAr2 are spatially separated in neuron (in the SynOptopatch technology). CheRiff was expressed in presynaptic cells while spine-jRGECO1a and QuasAr2 were expressed in postsynaptic cells. A digital micromirror device was used to illuminate light with different wavelength to different areas for controlling and reporting voltage and Ca^{2+} dynamics. Graphs are adapted from references 124 and 131.

1.4 The scope of the thesis

Advances in the development of light-driven actuators have allowed increasingly precise and fast control of neural activity to modulate animal behaviour. In parallel, the ongoing optimization of light-emitting Ca^{2+} indicators has permitted high-fidelity and real-time measurement of neural activity at cellular resolution in large populations of cells. Together, the progress in the two branches of optogenetics has raised the possibility of simultaneous optical controlling and monitoring brain activity at single-cell-resolution *in vivo*. However, issues like spectrum crosstalk between channelrhodopsins and high performance fluorescent Ca^{2+} indicators still present problems and better approaches for minimizing cross-talk are required. In order to achieve zero-crosstalk between the two types of optogenetic tools, Ca^{2+} indicators with new properties are currently in high demand. In this thesis, I present two new indicators that represent progress towards

overcoming the challenge of spectral cross-talk between indicators and actuators. One new indicator is a genetically-encoded bioluminescent Ca^{2+} indicator based on a topological variant of GCaMP6s. The other new indicator is a genetically-encoded NIR fluorescent Ca^{2+} indicator engineered from a BV-binding FP, mIFP. These two types of Ca^{2+} indicators are nearly ideal matches for use with popular optogenetic actuators.

In Chapter 2, we describe the development of the ratiometric bioluminescent Ca^{2+} indicator, LUCI-GECO1, based on a bright luciferase NanoLuc and a topological variant of GCaMP6s, which is termed ncpGCaMP6s. ncpGCaMP6s worked as well as GCaMP6s *in vitro* and in cultured neurons, but gave higher BRET efficiency than GCaMP6s did when fused to NanoLuc. LUCI-GECO1 was generated by connecting NanoLuc to the N-termini of ncpGCaMP6s followed by the optimization of the connecting peptide. LUCI-GECO1 outperformed ratiometric bioluminescent Ca^{2+} indicator CalfluxVTN in HeLa cells due to its higher affinity, which is inherited from GCaMP6s. We also demonstrated the usage of LUCI-GECO1 in cultured neurons and its compatibility with a optogenetic actuator, CheRiff.

Chapter 3 described our effort on the engineering of the first NIR fluorescent Ca^{2+} indicator, NIR-GECO1, with peak 1-photon excitation and emission within the NIR window (650 nm to 900 nm). NIR-GECO1 was developed based on the first truly monomeric NIR FP, mIFP, through extensive directed evolution. We fully characterized the brightness and Ca^{2+} -response of NIR-GECO1 in cultured neurons and acute brain slices. We also demonstrated that NIR-GECO1 was able

to report neural activity in anesthetized mouse brain at mesoscale. Furthermore, owing to its highly red-shifted fluorescence, NIR-GECO1 was demonstrated practically useful for *in vitro* imaging in combination with optogenetic actuators and other fluorescent-protein-based indicators.

In Chapter 4, we described further optimization of NIR-GECO1 into NIR-GECO2 with brighter fluorescence and higher affinity to Ca^{2+} . NIR-GECO2 performs better than NIR-GECO1 in neuron cultures and acute brain slices. We also expressed NIR-GECO2 in neurons of *C. elegans* and demonstrated its use for reporting neural activity in transgenic worms.

Chapter 5 provides a summary of this thesis and a brief discussion on the future directions of bioluminescent and NIR fluorescent Ca^{2+} indicators.

Chapter 2: A Bioluminescent Ca^{2+} Indicator Based on a Topological Variant of GCaMP6s

2.1 Abstract

Fluorescent genetically encoded calcium ion (Ca^{2+}) indicators (GECIs) enable Ca^{2+} dynamics to be monitored in a diverse array of cell types and tissues. One drawback of green fluorescent GECIs, such as the widely used GCaMP6, is that the blue wavelengths of light used to excite the GECI also activate optogenetic actuators such as channelrhodopsins. Accordingly, it is particularly challenging to simultaneously use both optogenetic actuators and GECIs to both control and image cell signaling. Bioluminescence is an alternative imaging modality that circumvents this problem by avoiding the need for illumination for fluorescence excitation. Here, we report the development of a bioluminescent GECI, designated LUCI-GECO1, based on efficient bioluminescent resonance energy transfer (BRET) between the NanoLuc luciferase and a topological variant of GCaMP6s. LUCI-GECO1 is a sensitive ratiometric GECI that retains the highly optimized properties of GCaMP6s, as we demonstrate by imaging of chemically and optogenetically induced Ca^{2+} concentration changes in cultured cells and neurons.

2.2 Introduction

Ca^{2+} is a second messenger that plays a central role in practically all signaling activities in mammalian cells¹³². Numerous FP-based genetically-encoded Ca^{2+} indicators (GECIs) have been developed and used to monitor

Ca²⁺ concentration dynamics in cultured cells and *in vivo*^{51,53,133,134,135,130}. Among those GECIs, the ultrasensitive and brightly fluorescent GCaMP6 series is currently one of the most highly optimized and widely used⁵³ (**Figure 2.1A**). As a green fluorescent probe, GCaMP6 requires excitation with blue light, which is strongly absorbed by most tissues; this leads to phototoxicity and limits imaging depth. In addition, optogenetic actuators such as the channelrhodopsin light-activated cation channels, are similarly activated by blue light. As blue light is required for both GECI excitation and actuator activation, it is typically not possible to image the GECI without also activating the actuator as discussed in section **1.3**^{112,136}. Bioluminescence imaging is an alternative to fluorescence imaging that replaces fluorescence excitation with a luciferase-catalyzed chemical reaction for the generation of emitted photons (as described in section **1.2**)¹³⁷.

In addition to its inherent compatibility with optogenetic actuators, other advantages of bioluminescent imaging include minimal phototoxicity, negligible background, and the absence of photobleaching. Notable disadvantages of bioluminescent imaging include the requirement of a luciferase substrate (a luciferin), and much weaker luminescent signal intensity.

A variety of bioluminescent GECIs, including ones that exist in nature and ones that have been engineered in the laboratory, have been used for Ca²⁺ imaging. For example, aequorin is a natural bioluminescent GECI found in jellyfish that produces light in the presence of Ca²⁺ and its substrate, coelenterazine¹³⁸. However, aequorin is generally difficult to image due to its low catalytic efficiency which results in relatively dim bioluminescence. To develop an improved

bioluminescent GECl, Saito *et al.* engineered Nano-lantern (Ca^{2+})⁸⁵. The mechanism of Nano-lantern (Ca^{2+}) involves the reversible intramolecular reconstitution of a split *Renilla* luciferase (Rluc8) due to the interaction of calmodulin (CaM) with a peptide that interacts with the Ca^{2+} -bound form of CaM. Efficient BRET to a genetically fused yellow fluorescent protein (YFP) results in increased brightness relative to Rluc8 alone. Nano-lantern (Ca^{2+}) provides Ca^{2+} -dependent bioluminescence intensity changes, but relatively low brightness remains a limiting factor⁸⁵.

A major advance in the area of bioluminescent imaging was the development of NanoLuc luciferase, which is substantially brighter than any previously reported luciferase⁸¹. NanoLuc has inspired the development of several bioluminescent GECl, including the GeNL (Ca^{2+}) series of intensimetric GECl with different K_d values ranging from 60 to 520 nM⁸⁶. The design of GeNL (Ca^{2+}) is similar to that of Nano-lantern (Ca^{2+}), but GeNL (Ca^{2+}) uses split-NanoLuc instead of split-RLuc8, and mNeonGreen instead of YFP. However, the bioluminescence signal of these intensimetric GECl is sensitive to the concentration of substrate and can be affected by motion artifacts¹³⁹. To avoid these problems, a ratiometric bioluminescent GECl, CalfluxVTN, has been developed¹⁰³. CalfluxVTN exhibits a Ca^{2+} -dependent change in BRET¹⁰³. Compared to the GeNL (Ca^{2+}) series, CalfluxVTN has a ratiometric emission signal (*i.e.*, the ratio of FP acceptor to luciferase donor bioluminescence) that corrects for differences in substrate concentration and minimizes motion artifacts. However, the Ca^{2+} affinity ($K_d = 480$

nM) of CalfluxVTN is outside the optimal range (100–200 nM) for the detection of action potentials in neurons.

We envisioned a new design for a ratiometric bioluminescent GECl that would retain all of the favorable properties of GCaMP6s, which have been optimized over many iterative rounds of protein engineering and screening for maximum sensitivity in neurons (**Table 1**)⁵³. Furthermore, we sought to take advantage of the high bioluminescent brightness of NanoLuc, which would be expected to exhibit low BRET efficiency to GCaMP6s in the Ca²⁺-free state, and high BRET efficiency in the Ca²⁺-bound state. Modulation of BRET efficiency from a luciferase donor to a FP acceptor is a well-established strategy for making bioluminescent GEClS^{103,104,140}. Typically, this is achieved by genetically fusing a conformationally dynamic sensing domain between the donor and acceptor domains. In contrast, our strategy for constructing a bioluminescent GECl aimed to take advantage of the fluorescent response of the GCaMP acceptor domain.

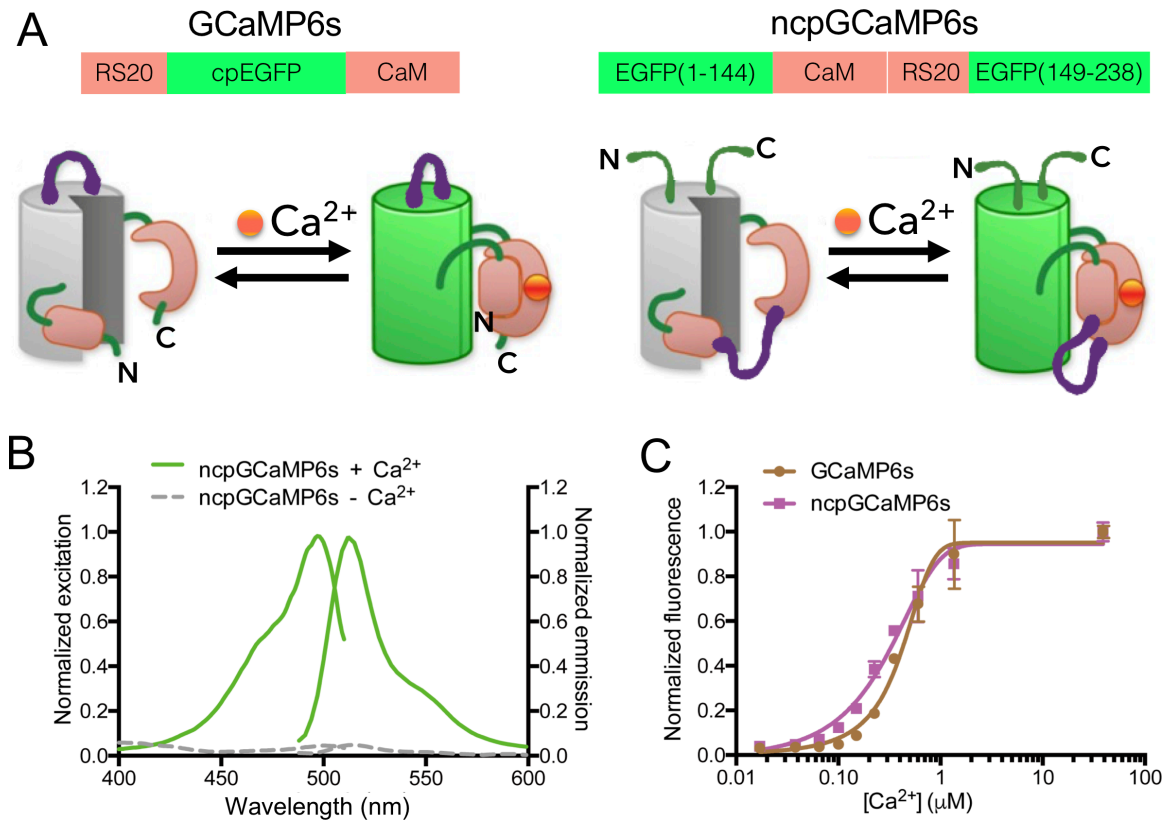


Figure 2.1. Engineering and *in vitro* characterization of ncpGCaMP6s.

(A) Representation of the GCaMP structure¹⁴¹. From N to C terminus: the Ca²⁺-CaM-binding peptide from light-chain myosin kinase (RS20); circularly permuted (cp) GFP; CaM. (B) Representation of the ncpGCaMP6s structure. A flexible peptide linker (GGGGS) was used to connect CaM and RS20 and allowed the original GFP N- and C- termini to be reintroduced. (C) Normalized excitation and emission spectra of ncpGCaMP6 in the Ca²⁺-free (0 μM Ca²⁺) and Ca²⁺-bound (39 μM Ca²⁺) states. (D) Ca²⁺ titration curves of GCaMP6s and ncpGCaMP6s. Data points are mean ± standard deviation, *n* = 3. Schematic representation adapted from Ref. 142

2.3 Results and discussion

To develop a bioluminescent version of GCaMP6s, we initially genetically fused NanoLuc to either the N or C terminus of GCaMP6s. Purification and *in vitro* characterization of NanoLuc-GCaMP6s and GCaMP6s-NanoLuc revealed that the BRET efficiency was low for both proteins. After the addition of 39 μM Ca^{2+} , the ratios of the green peak (resulting from BRET to GCaMP6s; $\lambda_{\text{em}}=516$ nm) to blue peak (resulting from direct NanoLuc emission; $\lambda_{\text{em}}=460$ nm) were 0.75 and 0.36, respectively (**Figure 2.3**). These results indicate a poor BRET efficiency and are consistent with the N- and C- termini of GCaMP6s being distant from the FP chromophore. Based on the crystal structure of GCaMP6m (PDB ID: 3WLD, the closest crystal structure to that of GCaMP6s)¹⁴¹, the distance from the chromophore, which is located near the geometric center of the protein, to the N and C termini are 42 and 30 Å, respectively. It has been previously reported that fusion of NanoLuc to the C terminus of enhanced GFP (EGFP) results in highly efficient BRET and an emission ratio (as defined above) of 2.97 (Ref. 143), thus indicating that the normal EGFP termini are closer to the chromophore. Based on the crystal structure of EGFP (PDB ID: 2Y0G), the distance from the N- and C-termini of EGFP to the chromophore are 22 and 25 Å, respectively. Accordingly, we reasoned that if we could connect NanoLuc to GCaMP6 in an arrangement that is similar to the connection to EGFP, the BRET efficiency would be higher.

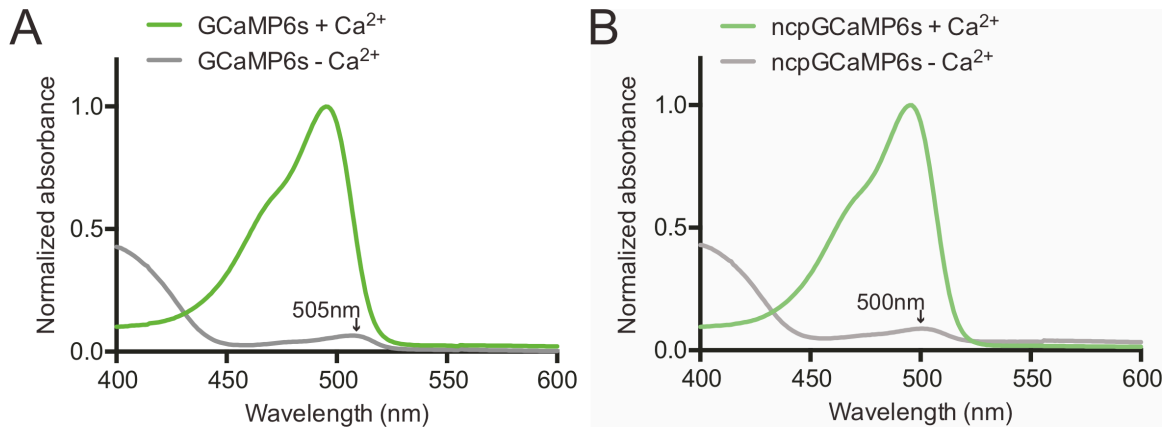


Figure 2.2. Absorbance spectra of GCaMP6s and ncpGCaMP6s.

(A) Normalized absorbance spectra of GCaMP6s with and without presence of Ca²⁺. (B) Normalized absorbance spectra of ncpGCaMP6s with and without presence of Ca²⁺. Absorbance peaks of GCaMP6s and ncpGCaMP6s in Ca²⁺-free state are at 505 nm and 500 nm, respectively; absorbance peaks of these two in Ca²⁺-bound state are the same, at 495 nm.

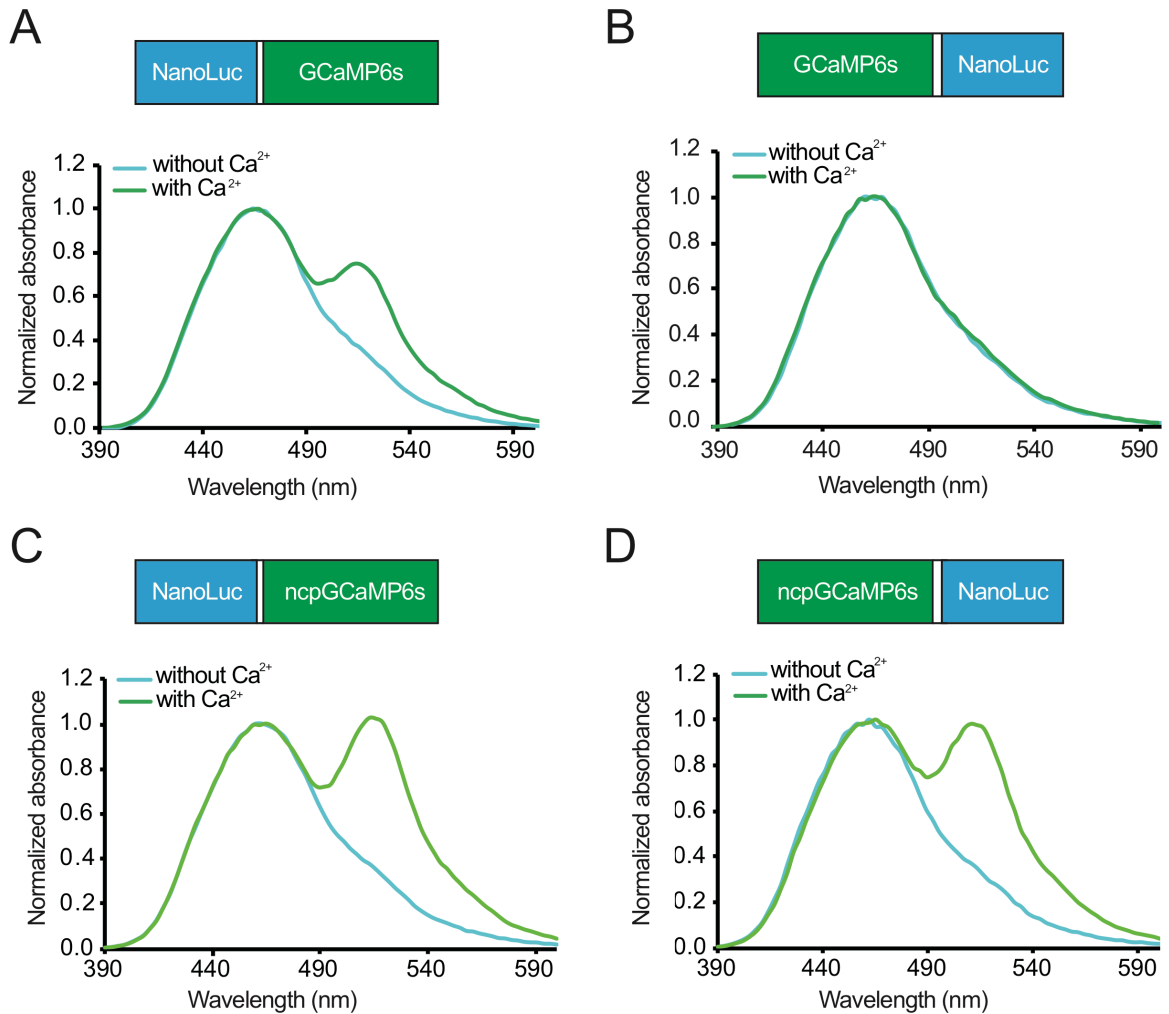


Figure 2.3. ncpGCaMP6s has higher BRET efficiency, as a bioluminescent acceptor, than GCaMP6s when fused to NanoLuc luciferase.

(A) Luminescence spectrum of NanoLuc fused to the N-terminus of GCaMP6s. (B) Luminescence spectrum of NanoLuc fused to the C-terminus of GCaMP6s. (C) Luminescence spectra when NanoLuc fused to the N-terminus of ncpGCaMP6s. (D) Luminescence spectra when NanoLuc fused to the C-terminus of ncpGCaMP6s. All of the constructs were tested in solution containing 10 μM EGTA and solution containing 39 μM Ca²⁺. Linkers between bioluminescence donors and fluorescence acceptors are short peptide with the sequence of GGSGT.

To construct a GCaMP6s variant with the same N- and C- termini as EGFP, we genetically rearranged the gene of GCaMP6s to give it an altered topology. Specifically, the RS20 and CaM domains were connected with a flexible peptide linker (GGGGS), and the original EGFP termini were reintroduced (**Figure 2.1B**). This topology corresponds to an insertion of the CaM–RS20 sensing domain into the FP; it was first used to construct the “camgaroo” GEC1¹⁴⁴, and has been recently used for Ca²⁺ and glutamate indicators^{145,146}. We refer to this topological variant of GCaMP6s as non-circularly permuted (ncp) GCaMP6s (ncpGCaMP6s). *In vitro* characterization of ncpGCaMP6s revealed that key properties such as absorption spectrum, excitation and emission spectra, dynamic range, p*K*_a, quantum yield, extinction coefficient, and dissociation kinetics remained very similar to those of GCaMP6s (**Figures 2.1C** and **Figure 2.2, Table 2.1**). One notable difference is that both the *K*_d (283 nM) and Hill coefficient (1.59) of ncpGCaMP6s are decreased relative to those of GCaMP6s (*K*_d=380 nM, Hill coefficient=2.43; **Figures 2.1D** and **Table 2.1**). These modest differences are attributed to the direct linkage of RS20 and CaM, which affects the affinity and cooperativity of their Ca²⁺-dependent interaction. Although not of direct relevance to this work, we speculate that, due to its being fused through both its N and C termini, the CaM portion of a ncpGCaMP could be less accessible for interaction with endogenous proteins; this could be a source of biological artifacts in GCaMP-expressing transgenic mice^{147,148}. In addition, a ncpGCaMP might be particularly well suited for use in targeted genetic fusions, as the fusion partner would be linked to either the normal N or C terminus of EGFP, as opposed to the RS20 or CaM

domain, which undergoes Ca^{2+} -dependent conformational changes as part of the GCaMP response mechanism.

Table 2.1. Biophysical properties of purified GCaMP6s and ncpGCaMP6s

Protein	Fold change (F_{\max}/F_{\min})	K_d^a (nM)	Hill slope	$pK_{a, \text{apo}}$	$pK_{a, \text{sat}}$	ϵ_{apo} (/1000) ($\text{mM}^{-1} \cdot \text{cm}^{-1}$)	ϵ_{sat} (/1000) ($\text{mM}^{-1} \cdot \text{cm}^{-1}$)	ϕ_{sat}	k_{off} (s^{-1})
GCaMP6s	30	380	2.43	9.77	6.00	4.5	73.5	0.61	1.08
ncpGCaMP6s	26	283	1.59	8.15	6.07	4.3	72.7	0.63	1.21

^a Values measured in this work. GCaMP6s has previously been reported to have $K_d=144 \text{ nM}^{53}$. K_d , dissociated constant; ϵ , extinction coefficient; ϕ , quantum yield; k_{off} , off kinetic constant.

To compare ncpGCaMP6s to GCaMP6s for multiphoton imaging of neuronal activity, we expressed both genes in cultured dissociated rat cortical neurons. Neurons transfected with each construct were imaged under identical conditions with application of a whole-cell-recording patch electrode. These experiments revealed that ncpGCaMP6s performs similarly to GCaMP6s in terms of fluorescence response to action potentials ranging from 1 to 16 in number (**Figure 2.4**). We conclude that changing the topology does not affect the performance of

GCaMP6s detrimentally for imaging small numbers of induced neuronal action potentials.

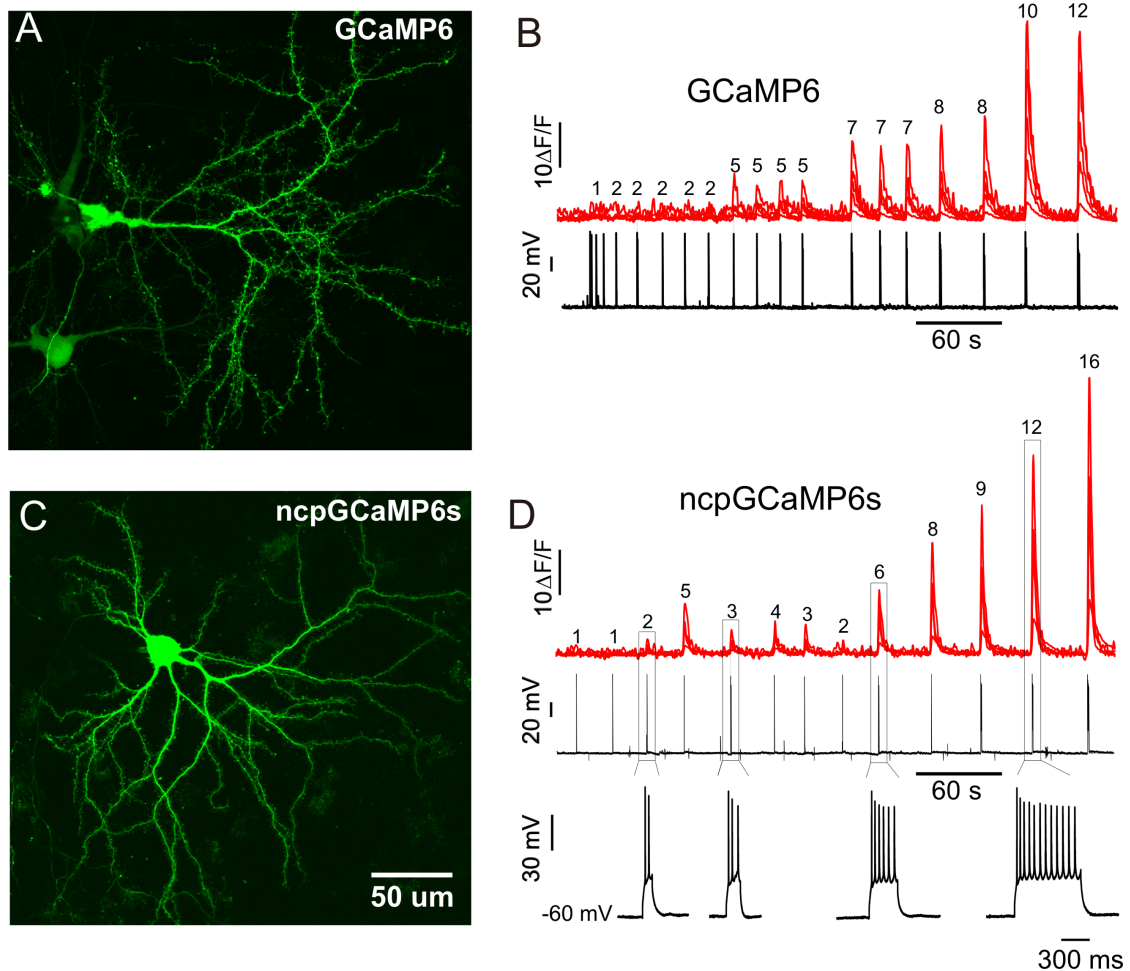


Figure 2.4. Comparison of GCaMP6s and ncpGCaMP6s in cultured dissociated cortical neurons.

(A) Representative multiphoton fluorescence image of neurons expressing GCaMP6s ($\lambda_{\text{ex}} = 920 \text{ nm}$ and $\lambda_{\text{em}} = 480/40 \text{ nm}$). (B) ncpGCaMP6s-expressing neuron imaged as in A. Scale bar is identical for A and B. (C) Optical recording of GCaMP6s and ncpGCaMP6s fluorescence responses (red) to different numbers

of action potentials (the numbers are shown on the top of the peaks) evoked by current injection through the whole-cell-recording patch electrode. The traces were extracted from regions of interest that included the whole cell bodies. Membrane potential traces are shown in black. An expanded time resolution for some responses is shown in the lowest trace. **(D)** $\Delta F/F_0$ of GCaMP6s and ncpGCaMP6s as functions of different numbers of APs. $n = 3$ neurons for GCaMP6s and $n = 5$ neurons for ncpGCaMP6s. Values are shown as means \pm standard deviation.

With the expectation that the termini of ncpGCaMP6s are less distant from the chromophore than the termini of GCaMP6s, we explored the use of ncpGCaMP6s for constructing a bioluminescent GEI. We constructed NanoLuc–ncpGCaMP6s and ncpGCaMP6s–NanoLuc by genetically fusing the two proteins with a five-residue linker (GGSGT). Luminescence spectra showed that the green-to-blue peak ratios in the Ca^{2+} -bound state were 1.03 and 0.98, respectively. These higher ratios (compared to 0.75 and 0.36 for the corresponding GCaMP6s fusions) indicated that, as expected, NanoLuc was closer to the chromophore, and the BRET efficiency was correspondingly higher. Although both fusions gave similar BRET efficiency, we decided to focus our optimization efforts on NanoLuc-ncpGCaMP6s due to its slightly higher BRET efficiency (**Figure 2.3C, D**). To increase the BRET efficiency further, we deleted one, two and three amino acids at the N termini of ncpGCaMP6s. We found out that deleting two amino acids ($\Delta\text{N}2$; **Figure 2.5A**) gave the highest BRET efficiency without adversely affecting the folding of ncpGCaMP6s. To increase the BRET efficiency even further, we deleted

three residues of the GGSGT linker and created a genetic library by randomizing the remaining two residues. This library of variants was expressed in colonies of *Escherichia coli*. The colonies (~50) that exhibited the brightest green fluorescence were picked and cultured, and their Ca^{2+} -dependent bioluminescent response was analyzed. The variant that exhibited the largest Ca^{2+} -dependent change in BRET efficiency was designated luciferase-based genetically encoded Ca^{2+} indicator for optical imaging 1 (LUCI-GECO1; **Figures 2.5A, B and Figure 2.6**).

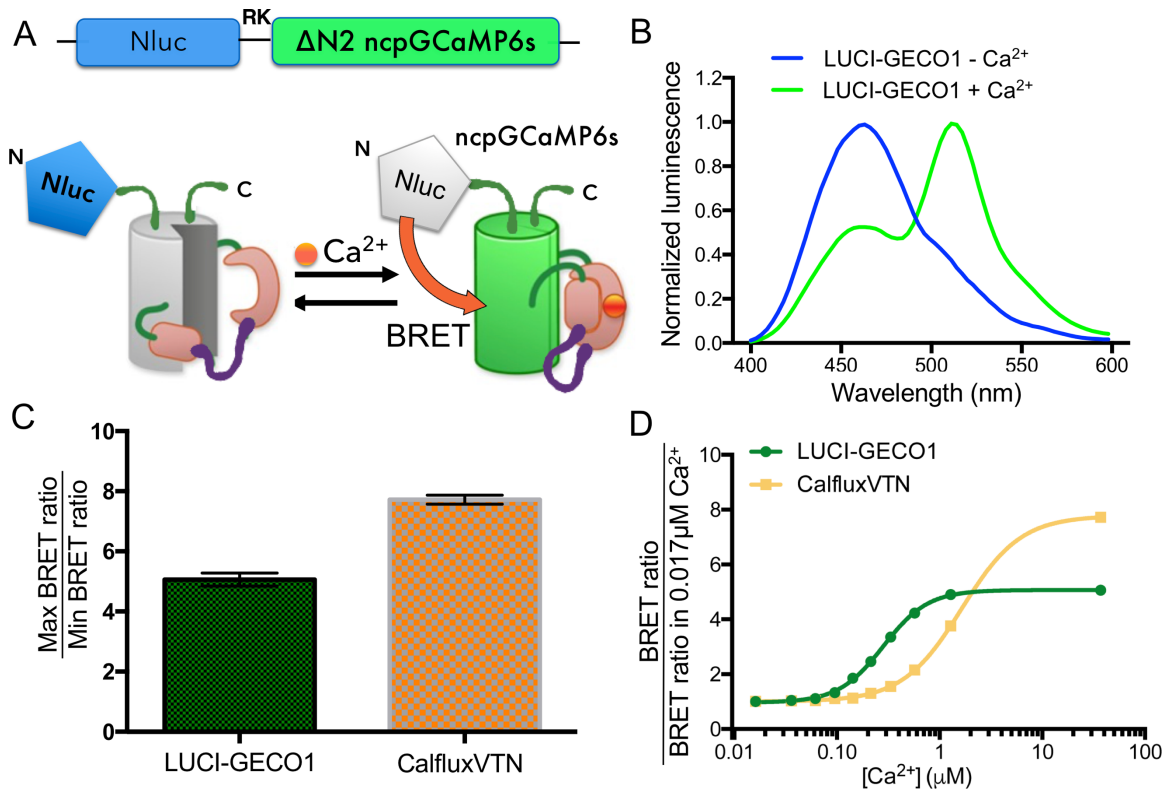


Figure 2.5. Design and *in vitro* characterization of LUCI-GECO1.

(A) Schematic representation of LUCI-GECO1. (B) Bioluminescence spectra of LUCI-GECO1 in 0 and 39 μM Ca^{2+} buffers. (C) Dynamic ranges of LUCI-GECO1 and CalfluxVTN. The values obtained in 0.017 and 39 μM Ca^{2+} buffers were recorded, and the dynamic ranges were calculated as defined in the BRET ratio in 39 μM Ca^{2+} divided by the BRET ratio in 0.017 μM Ca^{2+} . Data points are represented as means \pm standard deviation ($n = 3$). (D) Ca^{2+} titration curves of LUCI-GECO1 and CalfluxVTN. BRET ratio values were obtained by dividing the light emitted at the green peak (≈ 515 nm for LUCI-GECO1 and ≈ 525 nm for CalfluxVTN) by that emitted at the NanoLuc peak (≈ 460 nm). Values were normalized by dividing by the BRET ratio obtained in 0.017 μM Ca^{2+} . Data points are represented as means \pm standard deviation ($n = 3$).

MVFTLEDFVGDWRQTAGYNLDQVLEQGGVSSLFQNLGVSVTPIQRIVL
SGENGLKIDIHVIIPYEGLSGDQMGQIEKIFKVVYPVDDHHFKVILHYGTL
VIDGVTPNMIDYFGRPYEGIAVFDGKKITVTGTLWNGNKIIDERLINPDG
SLLFRVTINGVTGWRLCERILARKSKGEELFTGVVPILVELDGDVNGHKF
SVSGEGEGDATYGKLTCLKFICTTGKLPVPWPTLVTTLTYGVCFSRYPDH
MKQHDFFKSAMPEGYIQERTIFFKDDGNYKTRAEVKFEGDTLVNRIELK
GIDFKEDGNILGHKLEYNLPDQLTEEQIAEFKEAFSLFDKDGDTITTKEL
GTVMRS LGQNPTAEELQDMINEVDADGDGTIDFPEFLTMMARKMKY
RDTEEEIREAFGVFDKDGNGYISAAELRHVMTNLGEKLTDEEVDEMIRE
ADIDGDGQVNYEEFVQMMTAKGGGSDSSRRKWNKTGHAVRAIG
RLSSLENVYIKADKQKNGIKANFHIRHNIEDGGVQLAYHYQQNTPIGD
GPVLLPDNHYLSVQSKLSKDPNEKRDHMLLEFVTAAGITLGMDELYK-

Figure 2.6. Amino-acid-sequence of LUCI-GECO1.

The highlighted in blue and green are the NanoLuc moiety and ncpGCaMP6s moiety, respectively. Linker is shown as black.

As both LUCI-GECO1 and CalfluxVTN are ratiometric GEIs based on NanoLuc, we compared these two proteins *in vitro*. The dynamic range (*i.e.*, maximum ratio change) of LUCI-GECO1 is 5.06 ± 0.22 , which is smaller than that of CalfluxVTN (dynamic range of 7.72 ± 0.15). However, the K_d of LUCI-GECO1 (285 nm) is substantially lower than that of CalfluxVTN (1.1 μM ; **Figure 2.5C, D**). The lower K_d of LUCI-GECO, which is a property inherited from GCaMP6s, makes it more suitable for imaging physiologically relevant changes in Ca^{2+} concentration in environments such as the cytoplasm of cultured mammalian cells and primary neurons.

To demonstrate the utility of this new bioluminescent GEI in live cells, we expressed and characterized its Ca^{2+} response in HeLa cells, with manipulation of cytosolic Ca^{2+} concentration by addition of histamine¹⁴⁹. Histamine treatment causes the cytosolic Ca^{2+} concentration of HeLa cells to oscillate from <100 nM to several micromolar¹⁴⁹. The expression of LUCI-GECO1 in HeLa cells was under the control of CMV promoter. Fluorescence from ncpGCaMP6s and bioluminescence from NanoLuc after the addition of furimazine (diluted 100-fold from the Promega Nano-Glo Luciferase Assay System) can be easily detected (**Figure 2.7A**). Following stimulation with 20 μM histamine, Ca^{2+} oscillations were detected (**Figure 2.7A, B**). For LUCI-GECO1, the observed maximum dynamic range ($R_{\text{max}}/R_{\text{min}}$) is 3.32 ± 0.07 -fold ($n = 26$), which is larger than the 2.40 ± 0.06 -fold range of CalfluxVTN ($n = 13$; **Figure 2.7 C**). We conclude that, due to its higher

affinity for Ca^{2+} , LUCI-GECO1 performs better than CalfluxVTN for imaging Ca^{2+} dynamics in the cytoplasm of HeLa cells.

One of the most important applications of GECIs is to report Ca^{2+} concentration changes in neurons, as a proxy for neuronal action potentials. To test LUCI-GECO1 in neurons, we expressed it in dissociated rat cortical neurons and examined its performance four to six days after transfection. Expression of LUCI-GECO1 in neurons, under the control of human synapsin promoter (hSyn)¹⁵⁰, led to levels of fluorescence (ncpGCaMP6s) and bioluminescence (NanoLuc) that could be easily detected by using an electron-multiplying CCD camera (**Figure 2.8A, B**). After 20 mM KCl triggered neuron depolarization, the normalized BRET ratio (BRET ratio/ (BRET ratio)₀) of LUCI-GECO1 increased from 1 to 3.3 (**Figure 2.8C**); this indicated a large increase in Ca^{2+} concentration. To determine whether LUCI-GECO1 is able to report Ca^{2+} concentration changes in neurons when combined with optogenetic tools that could trigger excitatory cation fluxes after exposure to blue light, LUCI-GECO1 was co-expressed in neurons with CheRiff¹¹³. Following exposure to 2 s pulses of blue light (490/15 nm), a transient increase in the luminescent BRET ratio was observed, thus indicating that light stimulation of CheRiff elicits membrane depolarization, and subsequent Ca^{2+} flux was detected in neurons by LUCI-GECO1 (**Figure 2.8D**). Due to GCaMP6s' optimal sensitivity to Ca^{2+} , LUCI-GECO1 performs well in dissociated neurons.

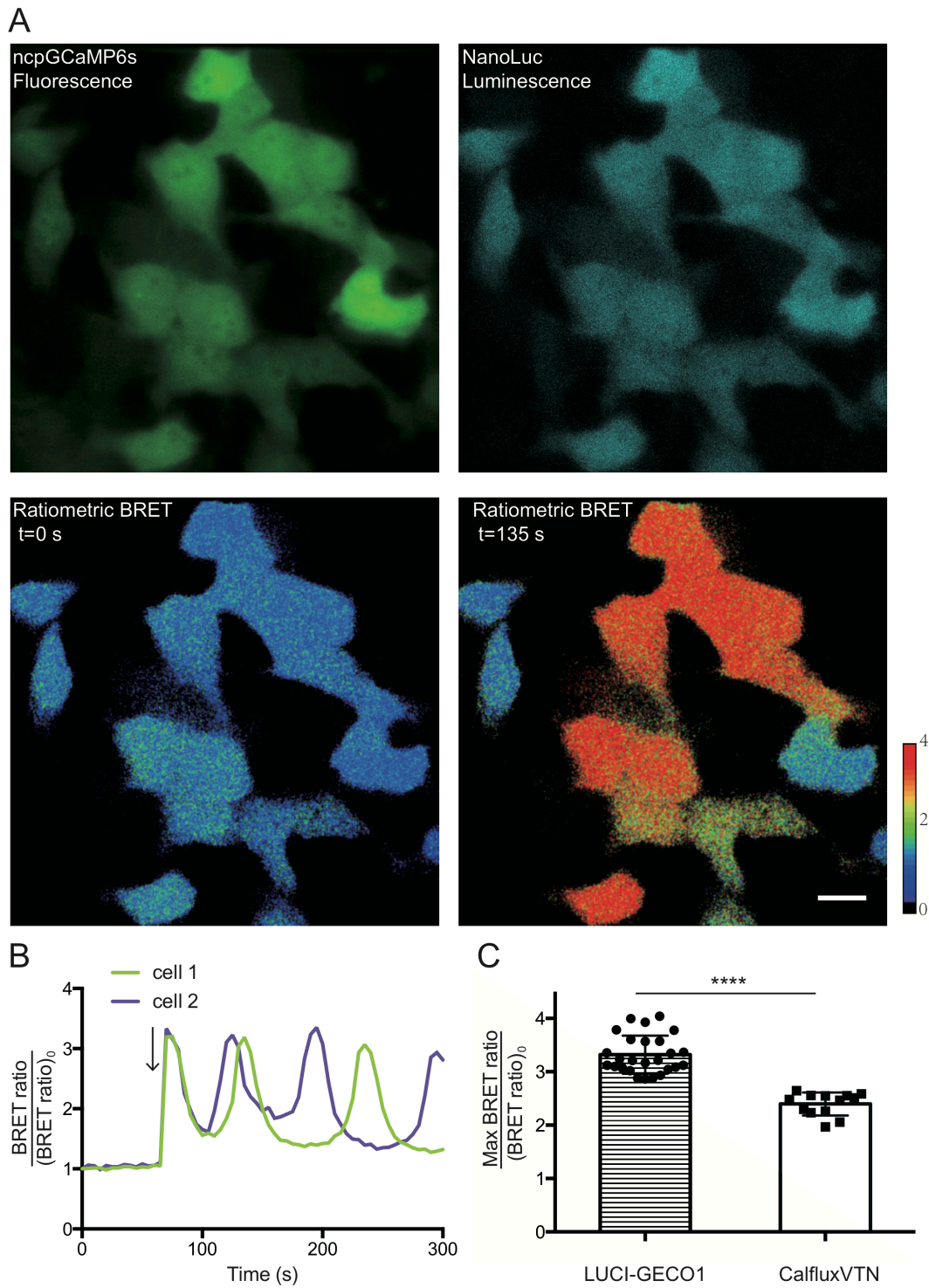


Figure 2.7. LUCI-GECO1 expressed in HeLa cells and its response to Ca^{2+} .

(A) HeLa cells expressing LUCI-GECO1. Top left: ncpGCaMP6s fluorescence image; top right: NanoLuc luminescence image. Lower left and lower right panels are pseudocolored ratiometric BRET images of HeLa cells at the start of image capture ($t = 0$ s) and at the first peak of the Ca^{2+} oscillation evoked by histamine ($t = 135$ s; scale bar: $20 \mu\text{m}$), respectively. **(B)** BRET ratio vs. time traces for HeLa cells transfected with LUCI-GECO1. The arrow indicates the addition of histamine. **(C)** Maximum BRET ratio changes following treatment with $20 \mu\text{M}$ histamine. For LUCI-GECO1, $n = 26$ from three independent experiments; for CalfluxVTN, $n = 13$ from three independent experiments. Data points are represented as mean \pm SEM. For comparison between LUCI-GECO1 and CalfluxVTN: * $p < 0.0001$, paired t-test.

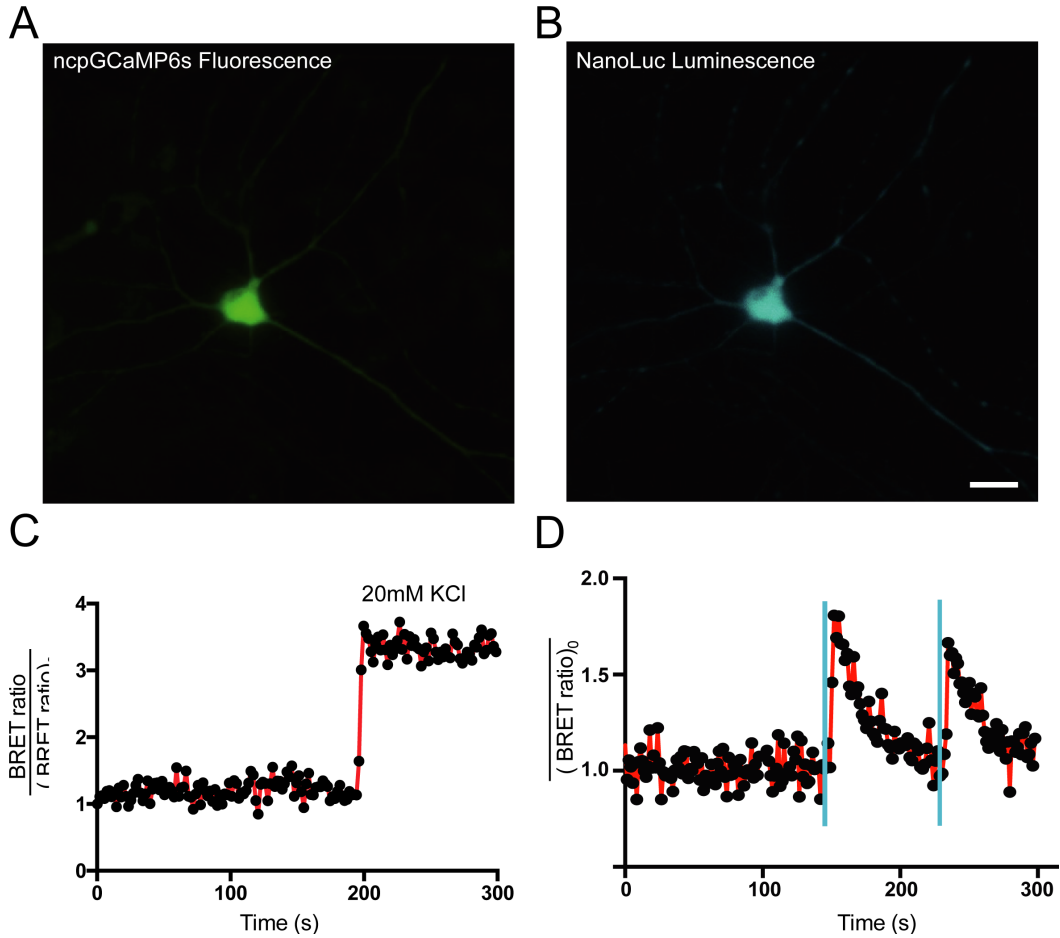


Figure 2.8. LUCI-GECO1 is sensitive to Ca^{2+} concentration changes in dissociated rat cortical neurons.

(A) Fluorescence of ncpGCaMP6s moiety, exposure time 20 ms. (B) Luminescence of the NanoLuc moiety, exposure time 5 s, scale bar: 20 μm . (C) The BRET ratio increase following the addition of 20 mM KCl, which triggered neuron depolarization, reported as an increase in cytosolic Ca^{2+} . (D) BRET ratio changes when neurons expressing LUCI-GECO1 and CheRiff are exposed to 2 s blue light (490/15 nm) pulses (imaged at 2 Hz). Blue bars indicate the time of the light pulses.

2.4 Conclusion

In summary, we have developed a topological variant of GCaMP6s, designated ncpGCaMP6s, in which the original N- and C- termini of EGFP have been restored. Fusion of the NanoLuc luciferase to the termini of ncpGCaMP6s resulted in higher BRET efficiency than fusion to the termini of GCaMP6s. This insight led us to develop the LUCI-GECO1 bioluminescent GEI. LUCI-GECO1 is useful for imaging Ca²⁺ signaling in cultured cells, including primary neurons, and is particularly advantageous for combined use with optogenetic tools such as channelrhodopsins, due to the lack of need for illumination for fluorescence excitation.

2.5 Materials and methods

2.5.1 General methods and materials

Synthetic DNA oligonucleotides used for cloning and library construction were purchased from Integrated DNA Technologies. Q5 high-fidelity DNA polymerase (New England BioLabs) was used for PCR amplifications in the buffer supplied by the respective manufacturer. PCR products and products of restriction digests were routinely purified using preparative agarose gel electrophoresis followed by DNA isolation using the GeneJET gel extraction kit (Thermo Fisher Scientific). Restriction endonucleases were purchased from Thermo Fisher Scientific and used according to the manufacturer's recommended protocol. Ligations were performed using T4 ligase in Rapid Ligation Buffer (Thermo Fisher Scientific).

Small-scale isolation of plasmid DNA was performed by GeneJET miniprep kit (Thermo Fisher Scientific). The cDNA sequences were confirmed by dye terminator cycle sequencing using the BigDye Terminator v3.1 Cycle Sequencing Kit (Applied Biosystems). Sequencing reactions were analyzed at the University of Alberta Molecular Biology Service Unit.

2.5.2 Construction and engineering of LUCI-GECO1

To engineer ncpGCaMP6s, a linker of Gly-Gly-Gly-Gly-Ser (**Figure 2.6**) was used to connect the N- and C-termini of the GCaMP6s, and the original N- and C-termini of the cpEGFP in GCaMP6s were used as the new N- and C-termini by overlap extension PCR. The resulting PCR products were digested by restriction enzymes XhoI and HindIII (Thermo Fisher Scientific). After digestion, these genes were ligated into a predigested pBAD/His B vector (Thermo Fisher Scientific). The ligation products were then transformed into DH10B *E. coli* which were then cultured on 10 cm LB-agar Petri dishes supplemented with 400 µg/mL ampicillin (Sigma) and 0.02% (wt/vol) L-arabinose (Alfa Aesar) at 37 °C overnight. On the next day, single colonies were picked and cultured in 4 mL liquid LB medium (100 µg/mL ampicillin) at 37 °C overnight. Plasmid DNA of ncpGCaMP6 was purified using GeneJET miniprep kit (Thermo Fisher Scientific), and was subjected to DNA sequencing for verification.

To assemble LUCI-GECO1, ncpGCaMP6s moiety was cloned by PCR using pBAD-ncpGCaMP6s as template DNA and NanoLuc moiety was cloned by PCR

using pNL1.1 (Promega) as template DNA and then these two fragments were connected by overlap extension PCR. The resulting PCR products were digested and ligated into a predigested pBAD/His B vector (Thermo Fisher Scientific). After replications in DH10B *E. coli*, plasmid DNA of LUCI-GECO1 was purified using GeneJET miniprep kit (Thermo Fisher Scientific), and was subjected to DNA sequencing for verification.

To improve BRET efficiency between NanoLuc and ncpGCaMP6s, different number of amino acids at the N-termini of ncpGCaMP6s were deleted by using QuikChange II Site-directed Mutagenesis Kit (Agilent Technologies). LUCI-GECO1 variants in the pBAD/His B vector (Thermo Fisher Scientific) were used for electroporation of *E. coli* strain DH10B (Thermo Fisher Scientific). *E. coli* containing these variants were then cultured on 10 cm LB-agar Petri dishes supplemented with 400 µg/mL ampicillin (Sigma) and 0.02% (wt/vol) L-arabinose (Alfa Aesar) at 37 °C overnight. During screening, colonies that showed the highest 0.1% green fluorescence intensities were picked and cultured in 4 mL liquid LB with 100 µg/mL ampicillin and 0.02% (wt/vol) L-arabinose at 37 °C overnight. Proteins were then extracted by B-PER (Thermo Fisher Scientific) from the liquid LB culture and subjected to a secondary test for BRET efficiency by using a SpectraMAX i3x plate reader (Molecular Devices).

2.5.3 Protein purification and *in vitro* characterization

To purify each protein sample for characterization, DH10B *E. coli* expressing each protein in pBAD/His vector were picked and cultured in 4 mL liquid LB medium (100 µg/mL ampicillin) at 37 °C overnight. This 4-mL culture was then inoculated into 500 mL liquid LB medium (100 µg/mL ampicillin, 0.0016% L-arabinose) and cultured at 28 °C for 24 h. After culture, bacteria were harvested by centrifugation and resuspended in 30 mM Tris-HCl buffer (pH 7.4). Proteins were extracted from bacteria by cell disruptor (Constant Systems Ltd), followed by Ni-NTA affinity chromatography (Agarose Bead Technologies) for purification. Purified proteins were subjected to buffer exchange to 10 mM MOPS, 100 mM KCl (pH 7.2) with centrifugal concentrators (GE Healthcare Life Sciences).

For determination of fluorescence quantum yields, GCaMP6s (saturation state) was used as a standard for ncpGCaMP6s. Briefly, the concentration of protein in a buffered solution (30 mM MOPS, pH 7.2, with either 10 mM EGTA or 10 mM Ca-EGTA) was adjusted such that absorbance at the excitation wavelength was between 0.2 and 0.6. A series of dilutions of each proteins solution and standard, with absorbance values ranging from 0.01 to 0.05, was prepared. The fluorescence spectra of each dilution of each standard and protein solution was recorded and the total fluorescence intensities obtained by integration. Integrated fluorescence intensity vs. absorbance was plotted for each protein and each standard. Quantum yield was determined from the slopes (S) of each line using the equation: $\Phi_{\text{protein}} = \Phi_{\text{standard}} \times (S_{\text{protein}}/S_{\text{standard}})$.

Extinction coefficients of ncpGCaMP6s were determined by first measuring the absorption spectrum of ncpGCaMP6s in Ca²⁺-free buffer (30 mM MOPs, 100 mM

KCl and 10 mM EGTA at pH 7.2) and Ca²⁺-buffer (30 mM MOPS, 100 mM KCl and 10 mM Ca-EGTA at pH 7.2). The concentration of ncpGCaMP6s were determined by measuring the absorbance following alkaline denaturation and assuming $\epsilon = 44,000 \text{ M}^{-1}\text{cm}^{-1}$ at 446 nm. Extinction coefficient of the protein were calculated by dividing the peak absorbance maximum by the concentration of protein. To determine the apparent pK_a for ncpGCaMP6s, a series of phosphate-free buffers was prepared as follows. A solution containing 30 mM trisodium citrate and 30 mM borax was adjusted to pH 11.5 and HCl (12 M and 1 M) was then added dropwise to provide solutions with pH values ranging from 11 to 3 in 1 pH unit intervals. The pH titration of Ca²⁺-free protein were performed by adding 1 μL of concentrated protein in Ca²⁺-free buffer (30 mM MOPS, 100 mM KCl, 10 mM EGTA, at pH 7.2) into 100 μL of each of the buffers described above. The pH titration of the Ca²⁺-bound protein was performed by adding 1 μL of protein in Ca²⁺ containing buffer (30 mM MOPS, 100 mM KCl and 10 mM CaCl₂, pH 7.2) into 100 μL of the pH buffers. The fluorescence of ncpGCaMP6s in each buffer condition was recorded using a Safire2 multiwell fluorescence plate reader (Tecan).

To determine Ca²⁺ apparent K_d of ncpGCaMP6s or GCaMP6s, concentrated protein solution was diluted (1:100) to a series of buffers which were prepared by mixing Ca²⁺-saturated and Ca²⁺-free buffers (30 mM MOPS, 100 mM KCl, 10 mM EGTA, pH 7.2, either with or without 10 mM Ca²⁺) to provide a series of solutions with free Ca²⁺ concentration ranges from 0 nM to 3,900 nM at 25 °C¹⁵¹. The fluorescence intensity of protein in each solution was determined and plotted as a function of Ca²⁺ concentration. Experiments were performed in triplicate and the

averaged data from the three independent measurements was fit to the Hill equation ($\theta = \frac{[L]^n}{K_d + [L]^n}$). A SX20 stopped-flow spectrometer (Applied Photophysics) was used to measure k_{off} . Briefly, protein samples with 10 mM CaCl_2 (in 10 mM MOPS, 100 mM KCl pH 7.2) were rapidly mixed with a solution with 10 mM EGTA (in 10 mM MOPS, 100 mM KCl pH 7.2) at room temperature. The k_{off} was determined by fitting the fluorescence decay curve to a single exponential equation. Each protein sample was measured 5' and the average value was taken as k_{off} .

To determine the bioluminescence spectra of LUCI-GECO1 or CalfluxVTN, SpectraMAX i3x plate reader (Molecular Devices) was used. To determine the apparent K_d of LUCI-GECO1 or CalfluxVTN, concentrated protein solution was diluted (1:100) to a series of buffers which were prepared by mixing Ca^{2+} -saturated and Ca^{2+} -free buffers (30 mM MOPS, 100 mM KCl, 10 mM EGTA, pH 7.2, either with or without 10 mM Ca^{2+}) to provide a series of solutions with free Ca^{2+} concentration ranges from 0 nM to 3,900 nM at 25 °C¹⁵¹. The bioluminescence spectra of protein in each solution was detected by SpectraMAX i3x plate reader (Molecular Devices) immediately after adding coelenterazine and the green peak to blue peak ratio (BRET ratio) was calculated and plotted as a function of Ca^{2+} concentration. Experiments were performed in triplicate and the averaged data from the three independent measurements was fit to the Hill equation.

We define the BRET ratio for LUCI-GECO1 as $\text{BRET ratio} = \frac{I_{516 \text{ nm}}}{I_{460 \text{ nm}}}$ and the BRET ratio for CalfluxVTN as $\text{BRET ratio} = \frac{I_{525 \text{ nm}}}{I_{460 \text{ nm}}}$, where I = bioluminescence intensity at the wavelength indicated by the subscript. We define the dynamic

range as the BRET ratio for the Ca^{2+} -saturated state divided by the BRET ratio for the Ca^{2+} -free state. The “green” bioluminescence peaks for LUCI-GECO1 and CalfluxVTN are at 516 nm and 525 nm, respectively.

2.5.4 Dissociated rat cortical neuron culture preparation

Neurons were dissociated at postnatal day (P0 - P2) from Sprague Dawley rats using TrypLE Express enzyme (Gibco) and were grown on poly-D-lysine (Sigma) coated 24-well glass bottom dish or on glass coverslips containing Neurobasal-A medium (Gibco), supplement B27 (2%) (Gibco), penicillin-streptomycin solution -10000 units penicillin/10000 μg streptomycin (1%) and GlutaMax (0.25%) (Sigma). Half of the culture medium was replaced every 4–5 days. All procedures for obtaining the cortical neuronal cultures were approved by the University of Alberta Animal Care and Use Committee and carried out in compliance with guidelines of the Canadian Council for Animal Care and the Society for Neuroscience's Policies on the Use of Animals and Humans in Neuroscience Research.

2.5.5 Electrophysiology and cytosolic Ca^{2+} imaging of GCaMP6s and ncpGCaMP6s in cultured cortical neurons

Neurons were transfected on days-in-vitro 7-8 using 50 μL of transfection medium (BrainBits) per one well containing Lipofectamine 2000 (Thermo Fisher Scientific) 1 μL and pcDNA 1 μg . The transfection medium with lipofectamine and pcDNA was added to 500 μL of the remaining medium in the well, maintained in

the incubator at 37 °C 5% CO₂, and replaced completely after 5 hours with fresh neuronal medium. The neuronal cultures were allowed to express the proteins and recover from transfection for 4-5 days. Prior to subsequent imaging, culture medium was replaced with Hanks' Balanced Salt Solution (HBSS, Thermo Fisher Scientific) or for patch clamp recording experiments with saline solution containing (in mM): 120 NaCl, 3 KCl, 1.5 CaCl₂, 1.5 MgSO₄, 1.25 NaH₂PO₄, 26 NaHCO₃ and 10 D-Glucose (pH adjusted to 7.4 by gassing with carbogen (95% O₂ + 5% CO₂)).

Fluorescence imaging during patch clamp recording was done using multiphoton laser-scanning microscopy (FV1000 MPE, Olympus). A MaiTai-BB Ti:sapphire femtosecond pulsed laser set to excite 920 nm was used for fluorescence excitation and an Olympus 20x immersion objective (NA: 1.00) was used to visualize the neurons for whole-cell recording and fluorescence imaging. The 'intracellular' patch electrode solution contained (in mM): 140 potassium gluconates, 1 NaCl, 2 MgCl₂, 1 ATP-Na₂, 10 HEPES, pH adjusted to 7.25-7.35. No Ca²⁺ buffer like BAPTA was added to the solution in order to avoid attenuation of cytosolic free Ca²⁺ rises by excessive buffering. Membrane potential was recorded using an EPC-10 amplifier (HEKA) and sampled at 10 kHz using a digital recorder (PowerLab 8/35, ADInstruments). Membrane potential was held by injection of constant dc current at -60 mV and action potentials were evoked by injecting positive rectangular current pulses through the patch electrode. The frame rate for multiphoton imaging recording during patch clamp was 1.8 - 2.5 Hz.

2.5.6 Live cell imaging of bioluminescent Ca²⁺ indicators in HeLa cells and cultured cortical neurons

The gene of each bioluminescent Ca²⁺ indicators was cloned into modified pcDNA vector by PCR. HeLa cells (40-60% confluent) on 24-well glass bottom plate (Cellvis) were transfected with 0.5 µg of plasmid DNA and 2 µl TurboFect (Thermo Fisher Scientific). Following 2 h incubation, the media was changed to DEME (Gibco Fisher Scientific) with 10% FBS (Sigma-Aldrich), 2 mM GlutaMax (Thermo Fisher Scientific) and 1% penicillin-streptomycin (Gibco) and the cells were incubated for 48 h at 37 °C in a CO₂ incubator. Prior to imaging, culture medium was changed to HBSS. For bioluminescence cytosolic Ca²⁺ oscillation imaging, furimazine from Promega (Nano-Glo® Luciferase Assay System) was added to medium (diluted 100') followed by addition of histamine to a final concentration of 5 µM.

For imaging of KCl-induced neuron depolarization, furimazine from Promega (Nano-Glo® Luciferase Assay System) was added to medium (diluted 100'times) followed by addition of KCl to a final concentration of 20 mM. To record CheRiff stimulated neuron activities, furimazine from Promega (Nano-Glo® Luciferase Assay System) was added to the medium before taking images and blue light pulse (490/15 nm) was then applied.

Fluorescence and bioluminescence images were acquired using a Nikon Eclipse Ti microscope that was equipped with a 75 W Nikon xenon lamp, a 16-bit 512SC QuantEM EMCCD (Photometrics), and a 60× objective and was driven by a NIS-Elements AR 4.20 software package (Nikon). To capture the BRET signals,

blue and green filters were rotated in the emitting light path of the microscope.

Filter sets: Blue channel 480/40 nm; green channel 525/50 nm. For cell imaging,

we define BRET ratio as $BRET\ ratio = \frac{\text{Luminescence intensity collected from green channel}}{\text{Luminescence intensity collected from blue channel}}$

Chapter 3: A genetically encoded near-infrared fluorescent calcium ion indicator

3.1 Abstract

Genetically-encoded calcium ion (Ca^{2+}) indicators (GECIs) are widely used as reporters of neuronal activities. Although GFP-based GECIs have allowed precise measurement of neural activity *in vivo* at high spatial and temporal resolution and RFP-based GECIs have facilitated dual-color imaging together with green fluorescent indicators, GECIs with near-infrared (NIR) excitation and emission have advantages for combination with optogenetic actuators, multi-color imaging with GFP and RFP-based indicators, and deep-site *in vivo* imaging. Here, we report an intensimetric, NIR fluorescent, genetically encoded Ca^{2+} indicator (GECI) with excitation and emission maxima at 678 and 704 nm, respectively. This GECI, designated NIR-GECO1, enables imaging of Ca^{2+} transients in cultured mammalian cells and brain tissue with sensitivity comparable to that of currently available visible-wavelength GECIs. We demonstrate that NIR-GECO1 opens up new vistas for multicolor Ca^{2+} imaging in combination with other optogenetic indicators and actuators.

3.2 Introduction

In neurons, triggering of action potentials (APs) or synaptic transmission is always concomitant with large and rapid changes of Ca^{2+} concentration¹⁵²⁻¹⁵⁵,

which makes genetically-encoded Ca^{2+} indicators (GECI) reliable tools for measuring neuronal spiking. Optically active, genetically encoded (optogenetic) actuators, on the other hand, are near-ideal tools for control of neural activity with high spatiotemporal resolution¹⁵⁶. Thus, GECIs are often used together with optogenetic actuators for simultaneous recording and control of biological processes with high spatiotemporal resolution. However, substantial spectral overlap among currently available fluorescent GECIs, optogenetic actuators, and other genetically encoded indicators, limits the possibilities for multiplexing. Although the palettes of both fluorescent GECIs and optogenetic actuators have been expanded to facilitate the combination of these two branches of optogenetic tools (as described in section **1.3**), currently popular GECI-actuator pairs are not completely cross talk-free and estimation of cross-stimulation is required to avoid experimental artefacts^{126,127}.

Bioluminescent GECIs are potential cross-stimulation-free partners to optogenetic actuators due to the lack of external excitation and the low-intensity photon-output. However, the requirement of substrates (*i.e.* luciferin) for photon production raises additional complications such as challenging substrate-delivery *in vivo* and toxicity caused by substrates. Furthermore, although the intrinsic brightness of bioluminescent GECIs is not sufficient to activate optogenetic actuators, the SNR and Ca^{2+} sensitivity of bioluminescent GECIs are much lower than that of fluorescent GECIs^{103,157}. Thus, redder fluorescent GECIs are in high demand to achieve zero spectral cross-talk with blue/green light excitable optogenetic actuators.

Most genetically encoded fluorophores fall into two classes: visibly fluorescent β -barrel fluorescent proteins that are homologs of the *Aequorea* green fluorescent protein (GFP)¹⁵⁸, and far-red to NIR fluorescent BV-binding FPs (BV-FPs) derived from bacteriophytochromes (BphPs)³⁰ or other BV-binding proteins³⁵. FPs have emission peaks in the visible range (~450–670 nm), and BV-FPs have emission peaks in the NIR range (~670–720 nm) (as described in section 1.1). While many GECIs and other indicators have been engineered from FPs, to the best of our knowledge there have been no published reports to date of NIR fluorescent BV-FP-based GECIs. Indeed, reported examples of BV-FP-based indicators for any sort of dynamic biochemical event have been relatively limited. Notable examples include the use of BV-FPs as donors and acceptors in FRET-based indicators^{159,160} and the use of split iRFP713 (Refs. 160,161) or IFP1.4 (Refs. 162,163) in protein complementation assays to detect protein-protein interactions.

To expand the spectral palette of fluorescent GECIs^{133,164} into the NIR optical window, we have now developed a BV-binding protein that exhibits a Ca^{2+} -dependent change in fluorescence. This protein, designated NIR-GECO1, is an inverse response indicator that can be readily imaged in cultured cells and intact tissues using light intensities and exposure times that are similar to that used for some β -FPs and bright BV-FPs. We demonstrate that NIR-GECO1 opens up new vistas for multicolor Ca^{2+} imaging in combination with β -FPs and optogenetic actuators.

3.3 Results and discussion

3.3.1 Rationale for an insertion-based design

The primary challenge of designing a single FP-based GECl is to engineer an allosteric connection between a Ca^{2+} -dependent conformational change (*e.g.*, by calmodulin (CaM), interaction of CaM¹⁶⁵ and a Ca^{2+} -CaM-binding peptide (CBP)^{51,166}, or Troponin C (TnC)¹⁴⁵) into a change in the FP fluorescence. Achieving this goal requires that the Ca^{2+} -binding domain be in close proximity to the FP chromophore, whether it is the autogenically synthesized chromophore of a β -FP, or the bound BV of a BV-binding FP. In the case of β -FPs this has been achieved by either fusing CaM and the CBP to the termini of the protein that has been circularly permuted such that the termini are in close proximity to the chromophore^{51,166}, or by directly inserting the Ca^{2+} -binding domain into β -FP at a position close to the chromophore^{145,165}. Single FP-based Ca^{2+} indicators with both circularly permuted (*i.e.*, Ca^{2+} -sensing domains fused to the termini of a circularly permuted FP) and non-circularly permuted (*i.e.*, a Ca^{2+} -sensing domain inserted into an FP) topologies have been reported. Examples of circularly permuted indicators include GCaMP^{51,53}, Pericam¹⁶⁶, R-GECO1(Ref. 133), RCaMP1 (Ref. 164), and K-GECO1 (Ref. 167) and derivatives thereof^{130,134,168-170}. There are fewer examples to date of non-circularly permuted indicators, with camgaroo¹⁶⁵, NTnC¹⁴⁵ and ncpGCaMP6s¹⁵⁷ serving as prototypical examples.

While the apparent success of the circularly permuted design suggests that it would be a good basis for designing a BV-FP GECl, we chose to pursue a non-

circularly permuted design based on Ca²⁺-binding domain insertion. There were two reasons for choosing this design. The first reason is that we have found that some circularly permuted indicators can be converted to non-permuted topologies, with minimal impact on their function. For example, non-circularly permuted iGluSnFR (Gncp-iGluSnFR) retains a fluorescence response and glutamate affinity that is very similar to iGluSnFR¹⁷¹. The second reason is that the N- and C-termini of BV-FPs are ~33 Å from each other (vs. ~ 24 Å for GFP) suggesting that a particularly long linker would be required to join the termini in a circularly permuted variant.

We suspect that the non-circularly permuted topology, in which the critical and biologically promiscuous CaM domain is genetically linked at both termini, may have two key advantages relative to a circularly permuted (*i.e.*, GCaMP-type) topology. The first advantage is that, in a non-circularly permuted topology, the CaM is directly connected with its binding partner RS20, which makes it less accessible for interaction with endogenous protein binding partners than circularly permuted topology. It has been reported previously that interactions between circularly permuted GCaMP and endogenous proteins could lead to perturbations of normal cell biology^{147,148}. The second advantage is that the non-circularly permuted topology leaves the original N- and C-termini of the FP available for genetic fusion to other proteins of interest or targeting motifs. This is in contrast to the circularly permuted topology, where the N- and C-termini are associated with RS20 and CaM, respectively, and fusions to these termini may adversely affect the performance of the indicator.

3.3.2 Engineering of NIR-GECO1

To engineer a BV-FP GECI with color into the NIR region, we initially started with mIFP³⁶, the first truly monomeric BV-FP, as template. We inserted a gene fragment encoding CaM-RS20 domain into the gene encoding mIFP at four sites chosen based on inspection of x-ray crystal structure of DrBphP (PDB ID: 2O9B)¹⁷², which is the parent protein of IFP1.4 (Ref. 30) sharing 35% of amino acid homology with mIFP³⁶. Selected insertion sites were between amino acid residues 9-10, 57-58, 138-139, and 170-176. It turned out that only the replacement of residues 171–175 with CaM-RS20 yielded a protein with a Ca²⁺-dependent change in fluorescence *in vitro* (a twofold decrease) (**Table 3.1, Figure 3.1D**). To improve the indicator properties, we systematically optimized the insertion site (leading to deletion of mIFP residues 176 and 177) and the N- and C-terminal linkers (ultimately the sequences GAL and RRHD, respectively) connecting CaM-RS20 to mIFP (**Figure 3.1A, B, C**).

Table 3.1. Summary of fluorescence intensity and fluorescence response to Ca²⁺ when CaM-RS20 were inserted to various sites of mIFP.

Insertion sites	Fluorescence	Response to Ca ²⁺
9A-10F	Strong	No
57N-58T	Moderate	No
138R-139I	Strong	No
170F-176G	Weak	Yes

Residue numbering is consistent with mIFP.

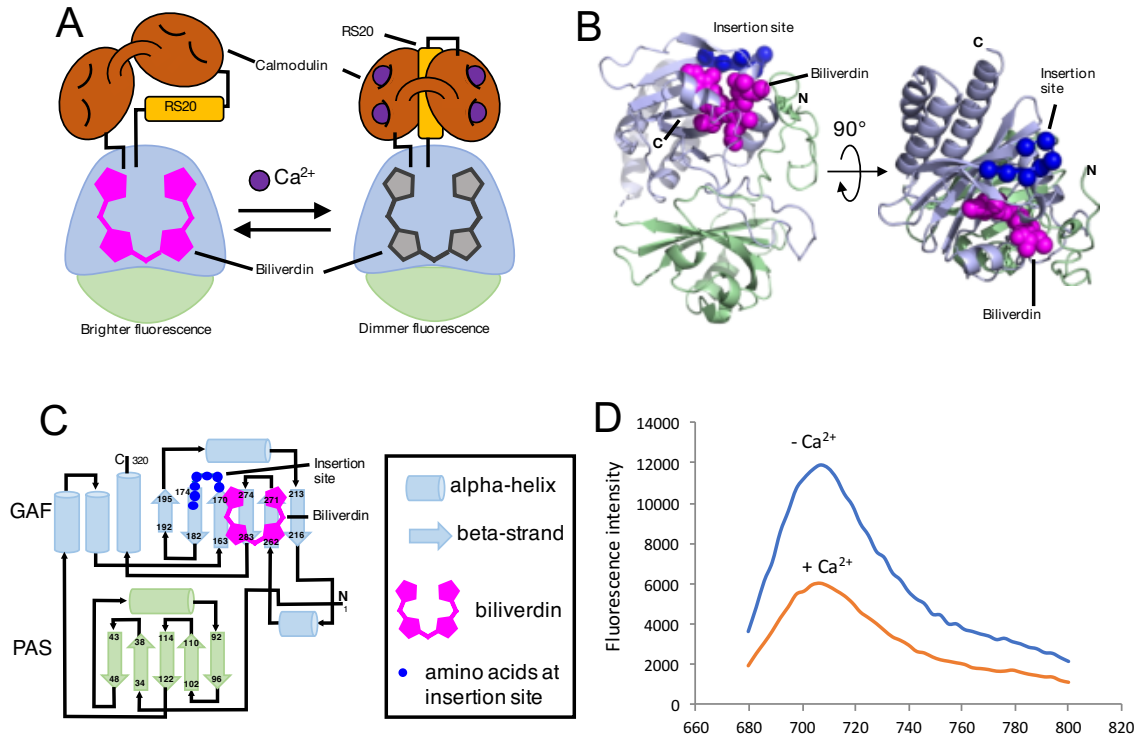


Figure 3.1. Design and Structure of mIFP-based GECl.

(A) Schematic representation of mIFP-based GECl and its mechanism of response to Ca^{2+} . The PAS domain is colored light green, and the BV-binding GAF domain is colored light blue. RS20 is the CaM-binding peptide of smooth muscle myosin light chain kinase. (B) Orthogonal views of the structure of *DrBphP* (PDB 2O9B)¹⁷², a close homolog of mIFP. The PAS and GAF domains are colored as in A, BV is shown as magenta spheres, and the $\text{C}\alpha$ atoms of the seven residues that were replaced with CaM-RS20 are shown as blue spheres. (C) The topology of mIFP (*i.e.*, bacteriophytochrome). Scheme is based on alignment of sequence of mIFP (320 residues; GenBank accession number AKH03689.1)³⁶, with the crystal

structure of the chromophore-binding domain of *Deinococcus radiodurans* BphP (PDB 2O9B)¹⁷². Representation is adapted from Takala *et al.*¹⁷³, with β -strands represented as arrows and α -helical regions represented as cylinders. The PAS domain is colored in light green, and the BV-binding GAF domain is colored in light blue, as in **A**, **B**. The approximate position of the bound BV is represented by a magenta structure. Numbers at the ends of β -strands correspond to mIFP numbering (see **Figures 3.2C, 3.3, 3.6**), based on alignment with the crystal structure. To engineer mIFP-based GECl, 5 residues (171–175, DEEGN) in the loop between the first two β -strands of the GAF domain were initially replaced with a 182-residue CaM-RS20 domain (a 3-residue linker followed by 147-residue CaM followed by a 5-residue linker followed by 23-residue RS20 followed by a 4-residue linker). Systematic optimization of the insertion site to improve the Ca²⁺-dependent fluorescence change led to the deletion of residues 176G and 177E of mIFP, resulting in an overall replacement of 7 residues (171–177, DEEGNGE) with the CaM-RS20 domain.

During the evolution, we noticed that there always existed trade-offs between brightness and Ca²⁺ dynamic range and brightness inconsistency between *E. coli* and mammalian cells (*i.e.*, HeLa cells). To facilitate iterative rounds of improvement on the basis of fluorescence screening of randomly mutated variants in bacterial colonies followed by functional tests in mammalian cells, we created a vector (pcDuex2) for expression in both *E. coli* and mammalian cells (**Figure 3.2A**). Based on pcDuex2, following screening procedures was used. Briefly, *E. coli* was

transformed with gene of a library and grew on LB plates, then bright colonies were picked and cultured followed by testing of both fluorescence and Ca^{2+} response on 384-well plates. Variants with reasonable brightness and Ca^{2+} response were selected and their gene were purified followed by expression of those genes in HeLa cells for the final screen based on cell brightness (**Figure 3.2B**). Following 12 rounds of library expression and screening (**Figure 3.3**), we designated our best variant as NIR genetically encoded Ca^{2+} indicator for optical imaging (NIR-GECO1, **Figure 3.3C**, and **Figure 3.5**).

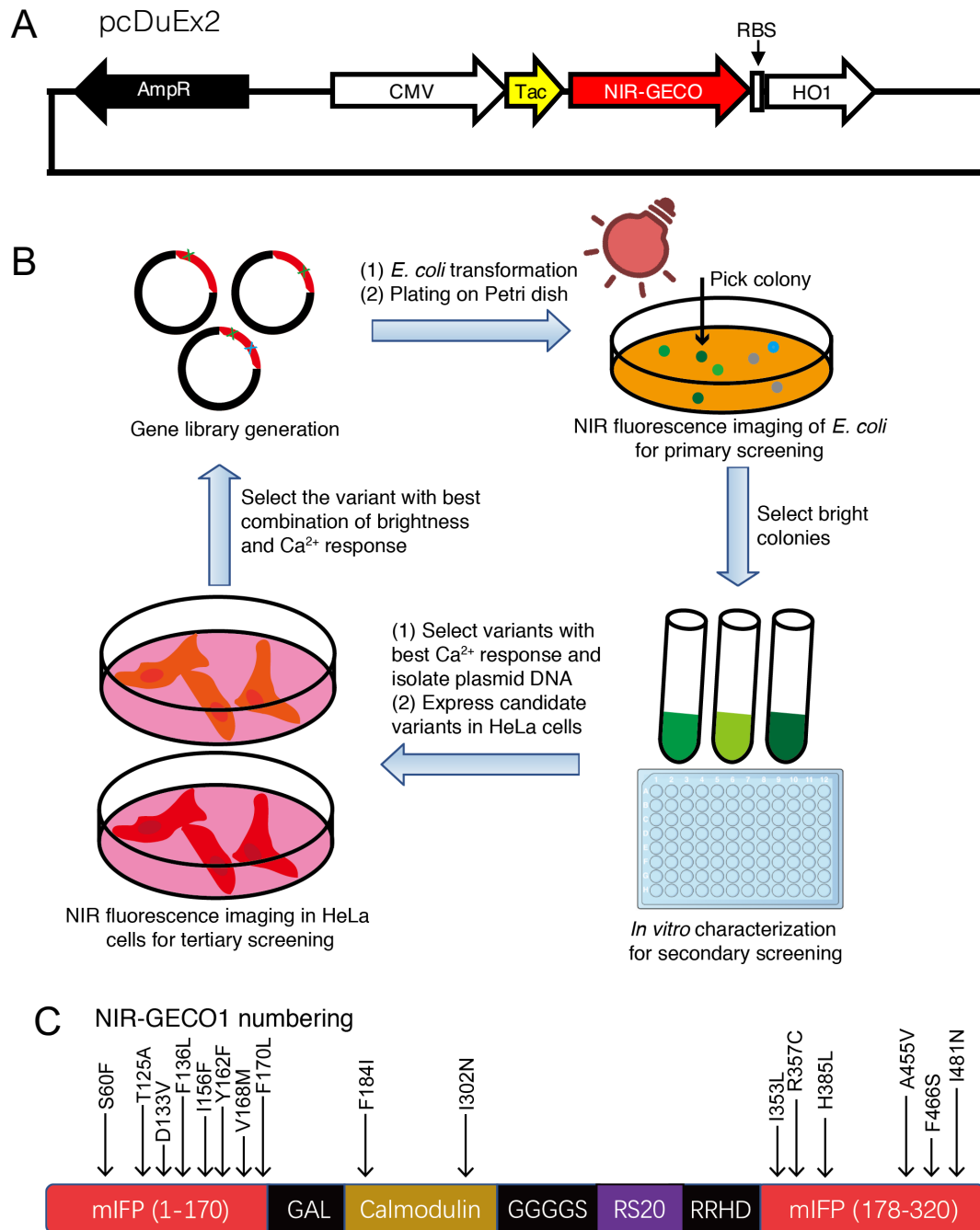


Figure 3.2. Directed evolution of NIR-GECO1 by library screening.

(A) Representation of the pcDuEx2 vector used for expression of genes in both bacteria and mammalian cells. Cytomegalovirus (CMV) promoter is used for mammalian expression, while the *Tac* promoter (a hybrid promoter derived from

the *trp* and *lac* promoters) is used for bacterial expression. HO1 is expressed in bacteria but, because of the presence of a stop codon after NIR-GECO1 and the lack of a promoter before HO1, it is not expressed in mammalian cells. RBS, ribosome binding site; HO1, heme-oxygenase 1. **(B)** Workflow of the screening process. Briefly, *E. coli* DH10B was transformed with a gene library in pcDuEx2 and grown on LB plates, and then bright colonies were picked and cultured. Proteins were extracted from overnight cultures of bacteria and then tested for fluorescence and Ca²⁺ response in 384-well plates. Variants with reasonable brightness and Ca²⁺ response were selected, and the corresponding plasmids were purified. HeLa cells were transfected with the selected plasmids, and live-cell fluorescence imaging was used to evaluate both brightness and Ca²⁺ response. HeLa cells were not supplemented with BV. **(C)** Mutations of NIR-GECO1 acquired during directed evolution.

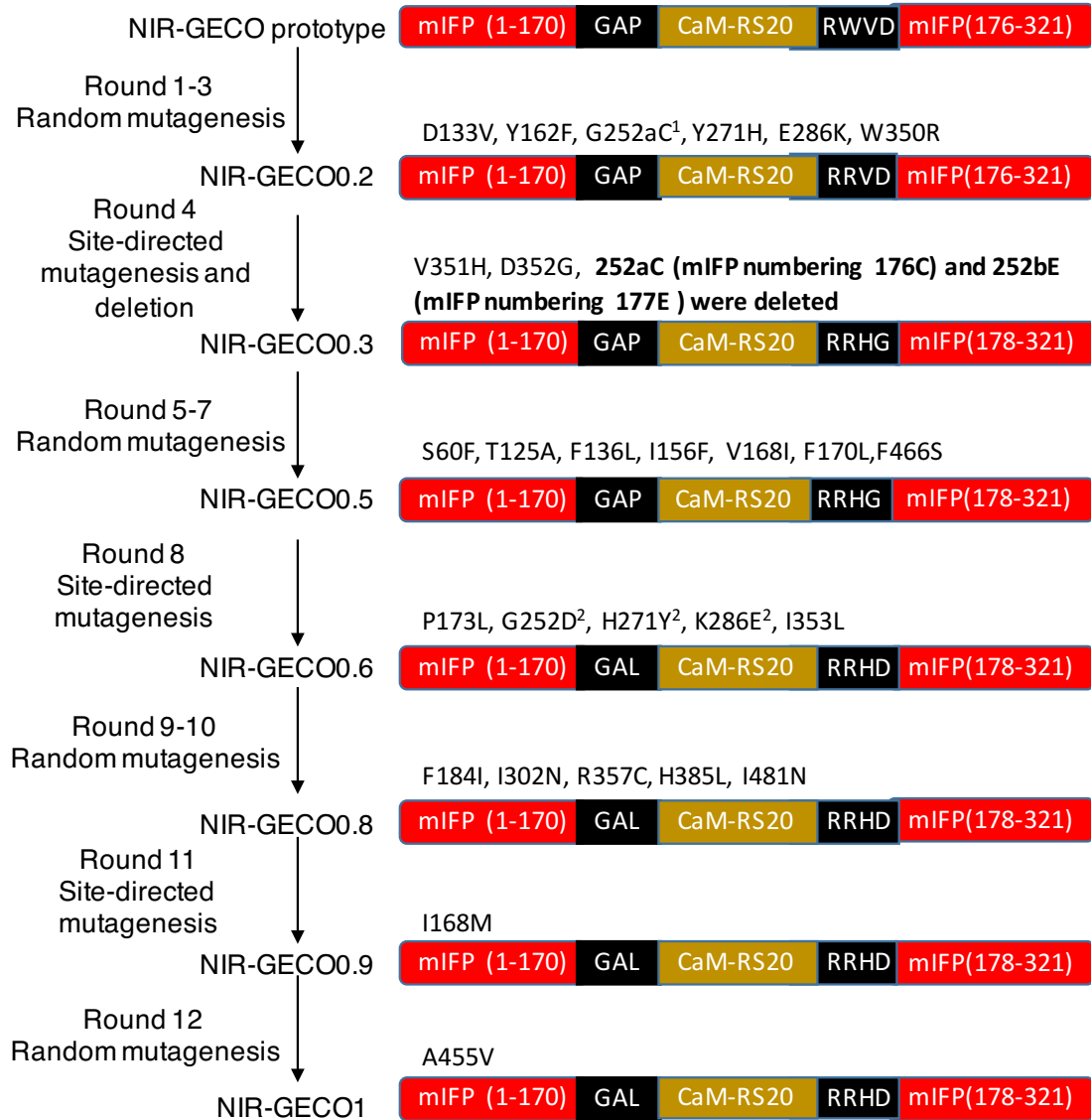
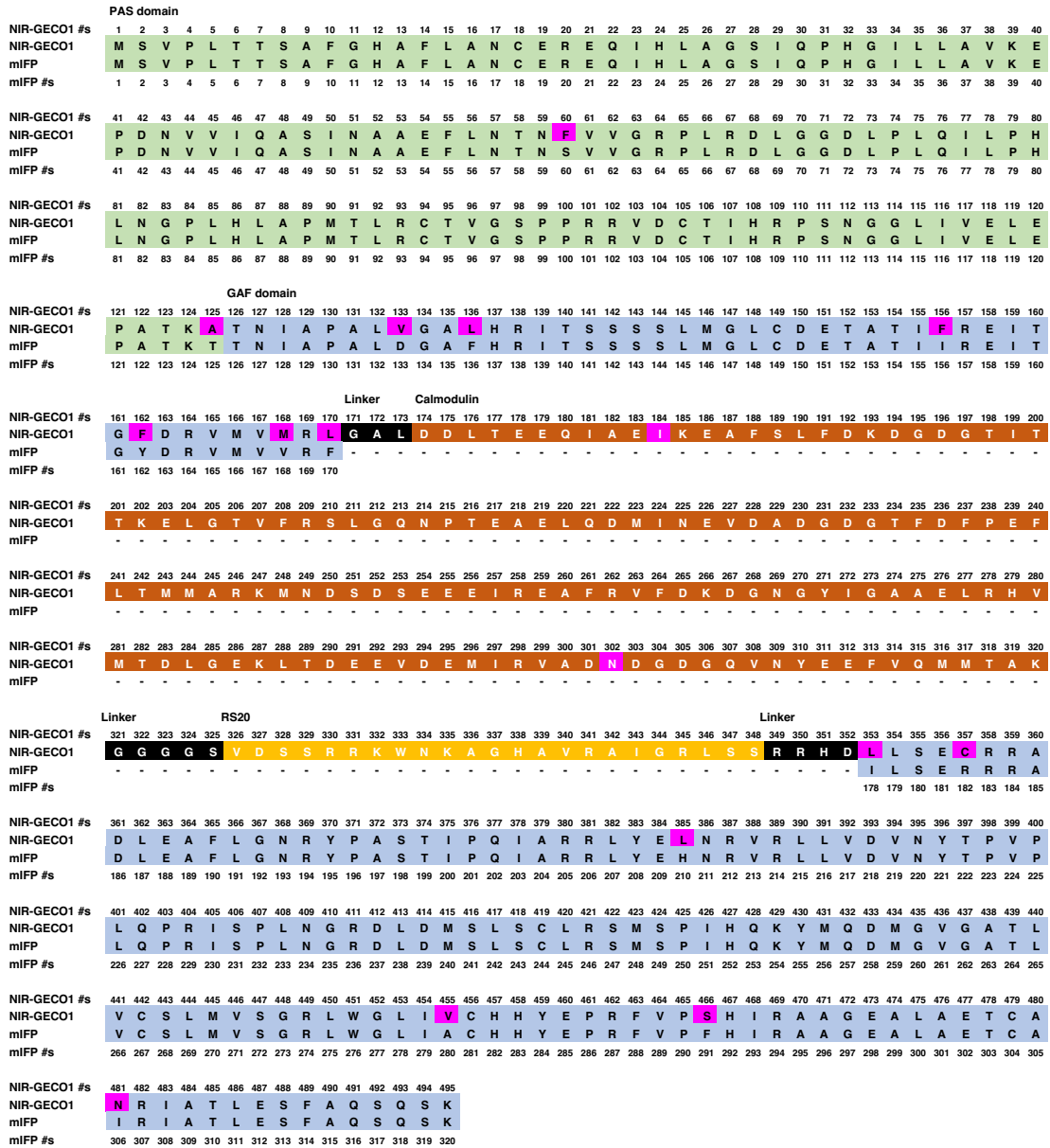


Figure 3.3. Lineage of improved NIR-GECO variants.

Key mutations included deletion of 252aC and 252bE, which substantially improved the Ca²⁺-dependent fluorescence change; F184I and I302N, which increased affinity for Ca²⁺; and W350R and R357C, A455V which substantially improved the brightness. Footnotes: ¹ This residue was deleted in round 4. ² These mutations were reversions.



3.3.3 Attempted engineering of a smURFP-based GECI

In a parallel effort, we attempted to engineer a smURFP-based³⁵ GECI using methods analogous to those used to develop NIR-GECO1 (**Figure 3.6**). smURFP has maximal excitation and emission at 643 nm and 670 nm, respectively, a quantum yield of 0.18, and an overall brightness that is comparable to that of EGFP due to its high extinction coefficient ($180,000 \text{ M}^{-1}\text{cm}^{-1}$). As with NIR-GECO1, our strategy involved inserting a CaM-RS20 domain in close proximity to the BV-binding pocket. After testing multiple candidate insertion sites, we identified a position (*i.e.*, between the fourth and fifth helix of smURFP) that both tolerated the insertion and rendered the fluorescence sensitive to Ca^{2+} . During each round of screening, the protein was tested for Ca^{2+} -dependent fluorescent response in crude bacterial lysate prepared with B-PER protein extraction reagent (Thermo Fisher). Under these conditions, this indicator exhibited a substantial fluorescence increase upon binding Ca^{2+} . Unfortunately, we were unable to achieve robust or functional expression of this indicator in cell culture. We suspect that the CaM-RS20 insertion may have substantially diminished the ability of the protein to bind to endogenous BV.

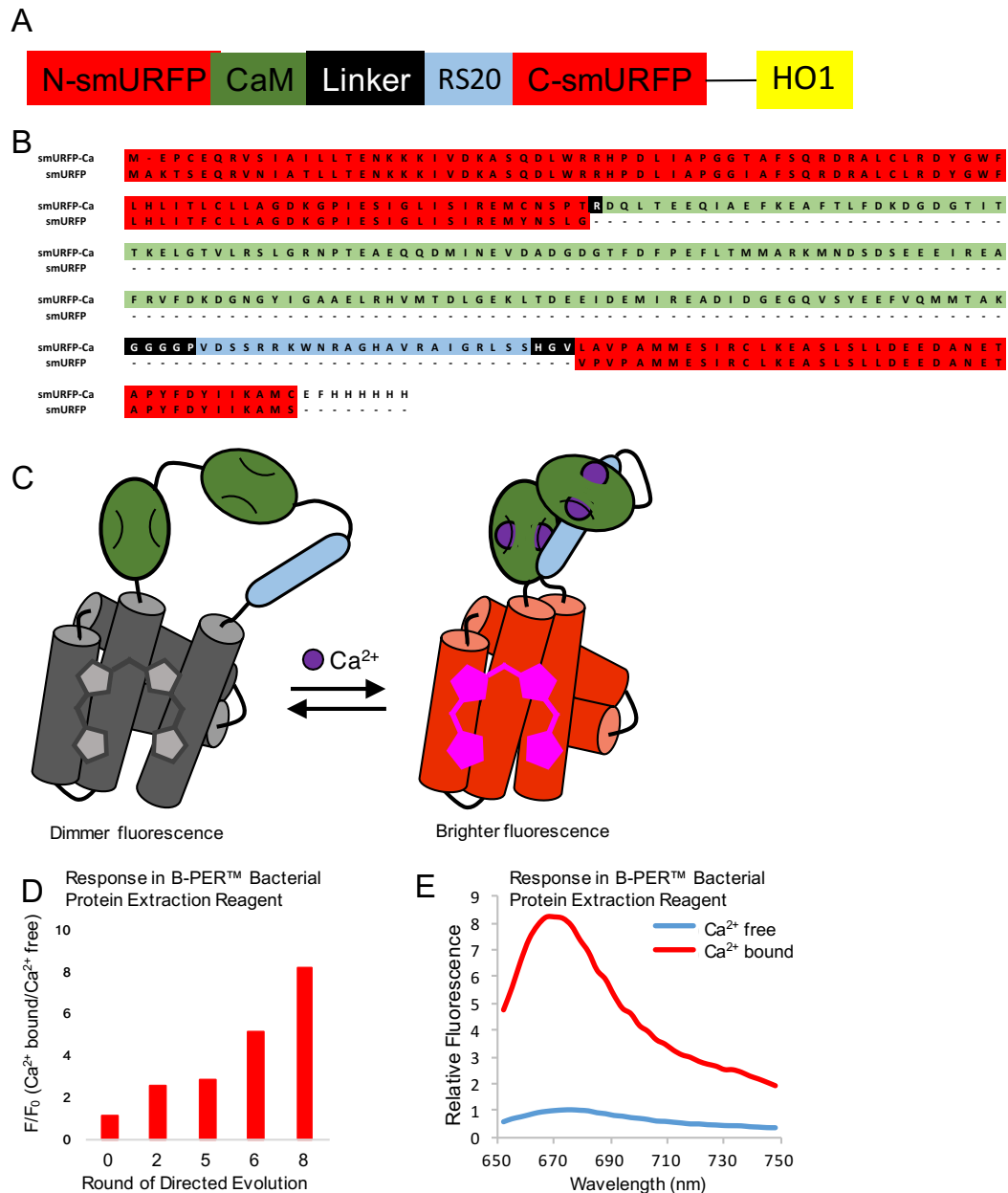


Figure 3.5. Attempted engineering of a smURFP-based Ca²⁺ indicator.

(A) Schematic representation of the smURFP-based Ca²⁺ indicator structure. (B) Sequence of the indicator after the eighth round of directed evolution. (C) Schematic representation of the protein structure and response. CaM-RS20 was inserted between the fourth and fifth helix of smURFP. The best variant exhibited

an approximately eight-fold change in fluorescence intensity (Ca^{2+} -bound/ Ca^{2+} -free) at the maximum emission (670 nm). **(D)** Improvement in Ca^{2+} change of smURFP-based Ca^{2+} indicator variants during directed evolution represented as a ratio of response amplitude at the maximum emission ($\lambda_{\text{max}} = 670 \text{ nm}$) of Ca^{2+} -bound and Ca^{2+} -free state. **(E)** Emission spectra for the protein after the eighth round, normalized to the Ca^{2+} -free state. Repeated independently more than 3 times with similar results.

3.3.4 *In vitro* characterization of NIR-GECO1

NIR-GECO1 has an absorbance peak at 678 nm, and emission peak at 704 nm in both Ca^{2+} -free and Ca^{2+} -bound form (**Figure 3.6A, B**). Upon binding to Ca^{2+} , the fluorescence of NIR-GECO1 undergoes a 90% decrease due to decreases in both extinction coefficient and quantum yield (**Table 3.2**). The K_d for Ca^{2+} is 215 nM, the apparent pK_a is 6.0, and Hill coefficient is 1.03 (**Table 3.2**). Overall, the key properties in terms of fluorescence change and K_d are comparable to those of GCaMP3 ($F_{\text{max}}/F_{\text{min}} = 13.6$; $K_d = 405 \text{ nM}$), which was the first broadly useful single-fluorescent-protein-based GECI⁵². Key differences include the opposite directions of the responses to Ca^{2+} , and the more linear fluorescent response to Ca^{2+} (GCaMP3 vs NIR-GECO1 in Hill coefficient :2.3 vs 1.03). As an inverse response indicator, NIR-GECO1 is in its more brightly fluorescent form in resting cells (low Ca^{2+}), and is therefore more susceptible to photobleaching under continuous illumination. In addition, excitation of resting cells above and below the imaging

plane will contribute to an increased background signal. As expected when comparing an FP to a BV-FP, the Ca^{2+} -bound state of GCaMP3 is approximately six-fold brighter than the Ca^{2+} -free state of NIR-GECO1 (**Table 3.2**)⁵².

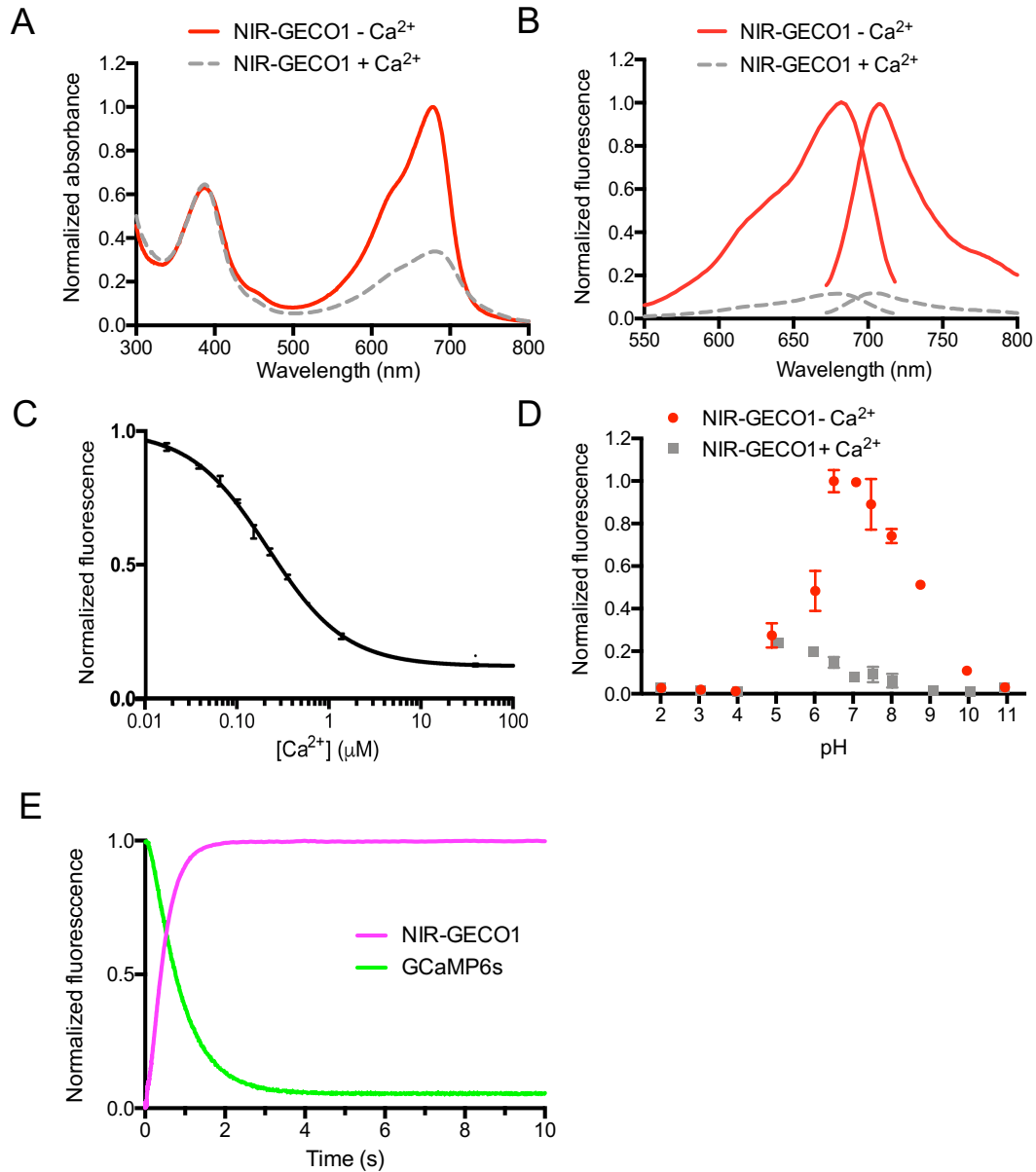


Figure 3.6. *In vitro* characterization of NIR-GECO1.

(A) Absorbance spectra in the presence (39 μM) and absence of Ca^{2+} . Representative of $n > 3$ independent experiments. (B) Fluorescence excitation and emission spectra in the presence (39 μM) and absence of Ca^{2+} . Representative of $n > 3$ independent experiments. (C) Fluorescence of NIR-GECO1 as a function of Ca^{2+} concentration. Center values are the mean, and error bars are s.d. $n=3$ independent experiments. (D) pH titration curves of NIR-GECO1 in the presence and absence of Ca^{2+} . $n = 3$ independent experiments; values are mean \pm s.d. (E) Ca^{2+} dissociation kinetics of NIR-GECO1 (magenta) and GCaMP6s (green). Data is the mean value of $n = 5$ replicates from one experiment.

Table 3.2. Spectral, photochemical and biochemical properties of NIR-GECO1 in comparison with iRFP682, miRFP, GCaMP6s and GCaMP3.

Protein	[Ca ²⁺] (mM)	Ex (nm)	Em (nm)	EC ($\times 10^3$ mM ⁻¹ cm ⁻¹)	QY (%)	Photo- stability $t_{1/2}^a$ (s)	pK _a	Dynamic range ^b	Hill coeff. (n)	K _d (nM)	k _{off} (s ⁻¹)
NIR- GECO1	0 ^c	678	704	62	6.3	480	6.03	8×	1.03	215	1.93
	5	678	704	20	1.9		4.68				
iRFP682 ^d	N/A	670	682	69	11.3	1860 ^e	4.6	N/A	N/A	N/A	N/A
miRFP ^d	N/A	674	703	92	9.7	2040 ^e	4.3	N/A	N/A	N/A	N/A
GCaMP6s	0 ^c	498	515	4.5	ND	ND	9.77	30×	2.4	144 ^f	1.08
	5	498	512	73.4	61		6.00				
GCaMP3 ^g	0 ^c	496	513	ND	ND	ND	8.40	13×	2.1	405	ND
	1	496	513	37.0	65		6.97				

Abbreviations: Ex, fluorescence excitation maximum; Em, fluorescence emission maximum; EC, extinction coefficient; QY, quantum yield; $t_{1/2}$, half-time; pK_a, pH corresponding to 50% of the maximal fluorescence brightness measured at optimal pH; K_d, K_d for Ca²⁺; k_{off}, Ca²⁺-dissociation kinetics measured by stopped-flow spectrometer; N/A, not applicable. ND, not determined.

^aMeasured in cultured neurons under continuous 631/28 nm wide-field illumination at 38 mW/mm².

^b $F(\text{zero free Ca}^{2+})/F(\sim 39 \mu\text{M free Ca}^{2+})$ for NIR-GECO1 and $F(\sim 39 \mu\text{M free Ca}^{2+})/F(\text{zero free Ca}^{2+})$ for GCaMP6s. NIR-GECO1 is not completely saturated in 39 $\mu\text{M free Ca}^{2+}$. The value of $F(\text{zero free Ca}^{2+})/F(5 \text{ mM Ca}^{2+})$ is 10.6.

^cIn presence of 10 mM EGTA (zero free Ca^{2+}).

^dData from Ref. 37.

^eExtrapolated using the data shown in **Fig. 3.7C**.

^fData from Ref. 53.

^gData from Ref.174.

3.3.5 Characterization of NIR-GECO1 in dissociated neuron culture.

To evaluate the performance of NIR-GECO1 in cultured neurons, we compared intracellular fluorescence brightness and photostability to those of the spectrally similar BV-FPs, iRFP682 (Ref. 34) and miRFP³⁷ under both one- and two-photon microscopy. iRFP682 was previously shown to be the brightest dimeric iRFP under one-photon excitation in mammalian neurons in culture and *in vivo* by Piatkevich *et al.*¹⁷⁵ and miRFP is one of the brightest monomeric BV-FPs that are spectrally similar to NIR-GECO1 (**Table 3.2**). In our hands, all three BV-FPs distributed evenly within the cytosol, dendrites and nucleus of neurons, with no apparent puncta or localized accumulations (**Figure 3.7A**). Quantification of the NIR fluorescence under wide-field excitation showed that mean value of the NIR-GECO1 baseline brightness was similar to that of miRFP and 2.5-fold lower than that of iRFP682 (**Figure 3.7B**). To estimate a fraction of the NIR-GECO1 apoprotein (without binding to BV) expressed in neurons, we administrated a saturating concentration of 25 μ M exogenous BV to the neuronal cultures for 3 h and then measured the NIR fluorescence. While the BV supplementation did not affect NIR-GECO1 localization (**Figure 3.7A**), it resulted in an approximately fivefold increase in the mean value of NIR-GECO1 baseline fluorescence (**Figure 3.7B**), indicating that ~80% of expressed NIR-GECO1 was not bound to BV. The addition of BV also resulted in a slight increase in the mean value of the NIR-GECO1 fluorescence changes during spontaneous activity ($16 \pm 6\%$ versus $20 \pm 8\%$ $-\Delta F/F_0$ for NIR-GECO1 and NIR-GECO1 + BV, respectively; mean \pm s.d. throughout; **Figure 3.8A, B**). This BV-free fraction is not fluorescent but

presumably participates in contra-productive Ca^{2+} buffering. Co-expression of heme-oxygenase 1 (HO1) with NIR-GECO1 using bicistronic vector, previously described approach to boost mIFP fluorescence *in vivo*³⁶, resulted in only a 1.4-fold enhancement of the NIR-GECO1 fluorescence intensity (**Figure 3.8C, D**). Under continuous wide-field illumination at 38 mW/mm^2 (about two to four times higher than typically used for NIR-GECO1 imaging), the photobleaching rate of NIR-GECO1 was approximately fourfold higher than those of miRFP and iRFP682 (**Figure 3.7C, Table 3.2**).

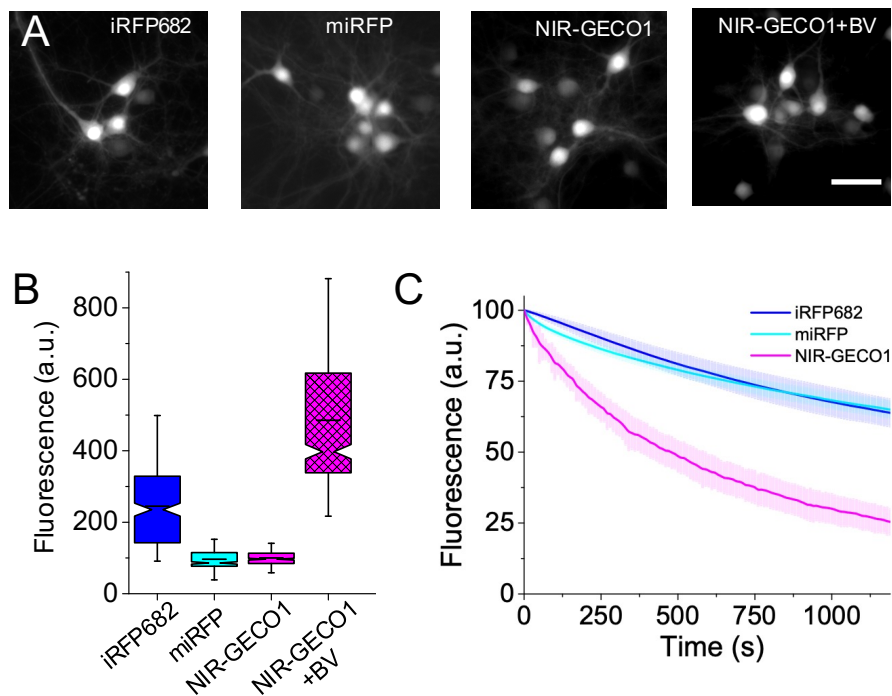


Figure 3.7. Brightness and photostability of NIR-GECO1 compared to iRFP682 and miRFP.

(A) Representative wide-field fluorescence images (631/28 nm excitation (Ex) at 38 mW/mm^2 and 664LP emission (Em)) of mouse neurons expressing iRFP682,

miRFP, NIR-GECO1, and NIR-GECO1 supplemented with exogenous BV (25 μ M) ($n = 263, 326, 367,$ and 473 neurons for iRFP682, miRFP, NIR-GECO1 and NIR-GECO1 + BV, respectively, from two cultures). The dynamic ranges of these images have been normalized to facilitate visual comparison of protein localization. Fluorescence brightness quantification provided in **B**. Scale bar, 50 μ m. **(B)** Relative fluorescence intensity for neurons shown in **A**. Box plots with notches are used. The narrow part of notch is the median; the top and bottom of the notch denote the 95% confidence interval of the median; the horizontal line is the mean; the top and bottom horizontal lines are the 25th and 75th percentiles for the data; and the whiskers extend $1.5 \times$ the interquartile range from the 25th and 75th percentiles. **(C)** Photobleaching curves for iRFP682, miRFP, and NIR-GECO1 ($n = 84, 69,$ and 88 neurons, respectively, from two cultures; 631/28 nm Ex at 38 mW/mm⁻²; solid lines represent mean value, shaded area represents standard deviation).

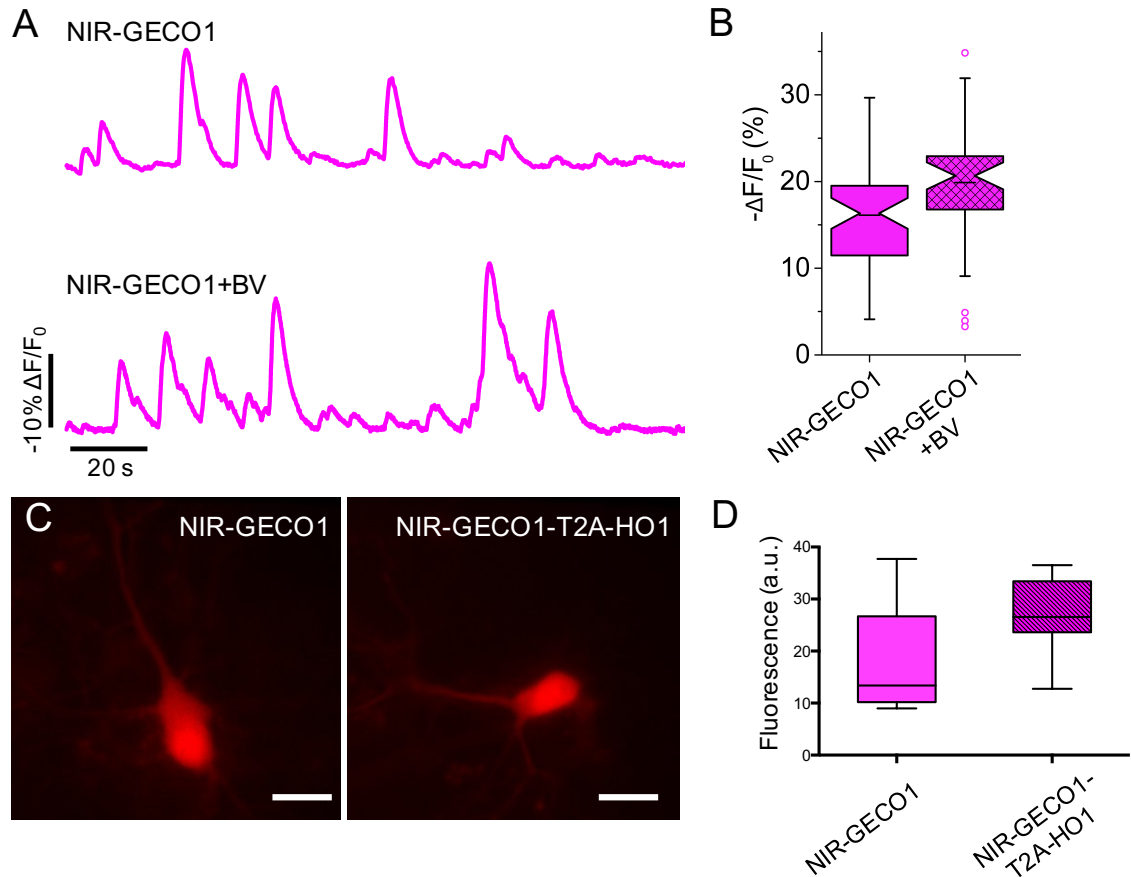


Figure 3.8. Increasing intracellular BV concentration has a modest effect on NIR-GECO1 brightness.

(A) Representative fluorescence traces of NIR-GECO1 (top) and NIR-GECO1 supplied with 25 μM exogenous BV (bottom) in response to neuronal spontaneous activities. Representative of $n = 51$ neurons for NIR-GECO1 and $n = 39$ neurons for NIR-GECO1+BV. (B) Quantification of $-\Delta F/F_0$ corresponding to the experiment of A. Values are $16 \pm 6\%$ for NIR-GECO1 and $20 \pm 8\%$ for NIR-GECO1 + BV (mean \pm standard deviation). Box plots are used as described in **Figure 3.7B**. (C) Representative wide-field fluorescence images of neurons expressing NIR-GECO1 (left) and NIR-GECO1-T2A-HO1 (right). The human HO1 gene was used.

Scale bar, 20 μm . **(D)** Relative normalized fluorescence of NIR-GECO1 ($n = 15$ neurons) and NIR-GECO1-T2A-HO1 ($n = 15$ neurons). Values are 18.3 ± 10.2 (a.u.) for NIR-GECO1 and 27.1 ± 7.0 (a.u.) for NIR-GECO1-T2A-HO1 (mean \pm standard deviation). Fluorescence was normalized by co-expression of EGFP (NIR channel, 650/60 nm Ex and 720/60 nm Em; green channel, 490/15 nm Ex and 525/50 nm Em). Box plots are used where the top and bottom horizontal lines mark the 25th and 75th percentiles for the data; whiskers extend to the maximum and minimum for the data; and the black horizontal bar is the median.

To characterize the fluorescence response of NIR-GECO1 to electric field stimulation-evoked action potentials (APs), field stimuli (50 V, 83 Hz, 1 ms) were delivered in trains of 1, 2, 3, 5, 10, 20, 40, 80, 120 and 160 to transfected neurons (**Figure 3.9A**). The resulting fluorescence changes, recorded from cell bodies, revealed that $-\Delta F/F_0$, signal-to-noise ratio (SNR), rise time, and decay time, all increased with the number of stimuli (**Figure 3.10A-D**). Relative to GCaMP3, NIR-GECO1 has similar $-\Delta F/F_{\text{min}}$ for 1-10 APs and a ~ 2 -fold higher SNR, but these values are ~ 10 -fold lower than those for GCaMP6s (**Figure 3.11A-D**). The near-linear stimulus-response over the range of ~ 2 to 40 stimuli is consistent with the near-unity Hill coefficient¹⁷⁰. In cells, the rise and decay times of NIR-GECO1 appear substantially slower than GCaMP6s. This observation is inconsistent with the fast Ca^{2+} -dissociation kinetics measured *in vitro* ($k_{\text{off}} = 1.93 \text{ s}^{-1}$ for NIR-GECO1 vs. 1.08 s^{-1} for GCaMP6s; **Figure 3.6E**). With no targeting sequence attached, NIR-GECO1 distributes throughout the cytoplasm and nucleus. Measuring from

the cell body, we found that nuclear-excluded NIR-GECO1 (NES-NIR-GECO1) exhibited similar kinetics to NIR-GECO1, ruling out slow Ca^{2+} diffusion in and out of the nucleus as an explanation for slower response kinetics (**Figure 3.11C, D**). When co-expressed in cultured neurons, NIR-GECO1 and GCaMP6s both reliably report spontaneous oscillations in Ca^{2+} concentration with opposite fluorescence changes (**Figure 3.12A, B**).

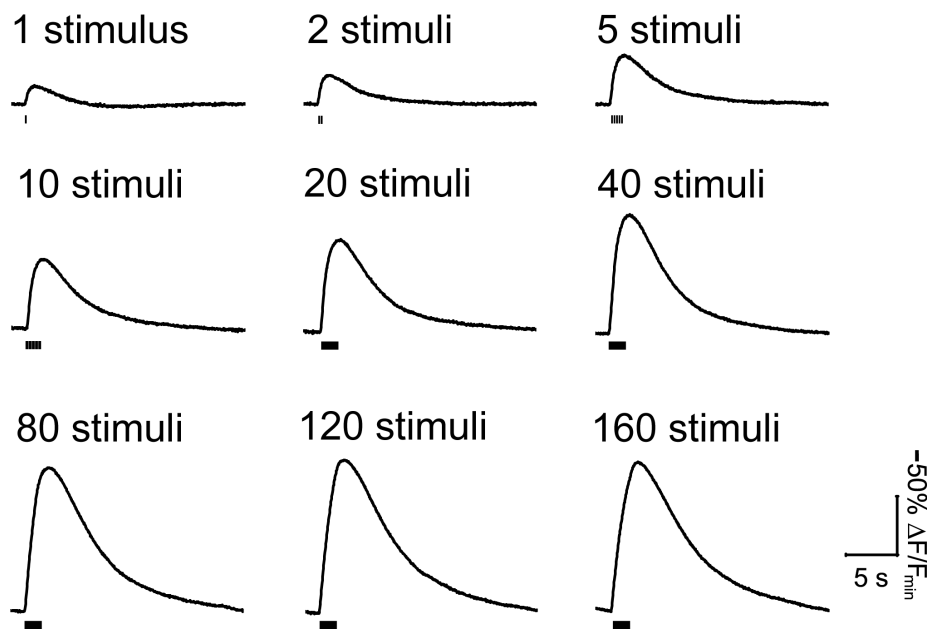


Figure 3.9. Representative traces of single trial NIR-GECO1 fluorescence responses to field stimulation in cultured mouse hippocampal neurons.

Neurons were stimulated and imaged simultaneously. Black bars under each peak indicate the time point of stimulation. Numbers of stimuli are shown on the top of each peak.

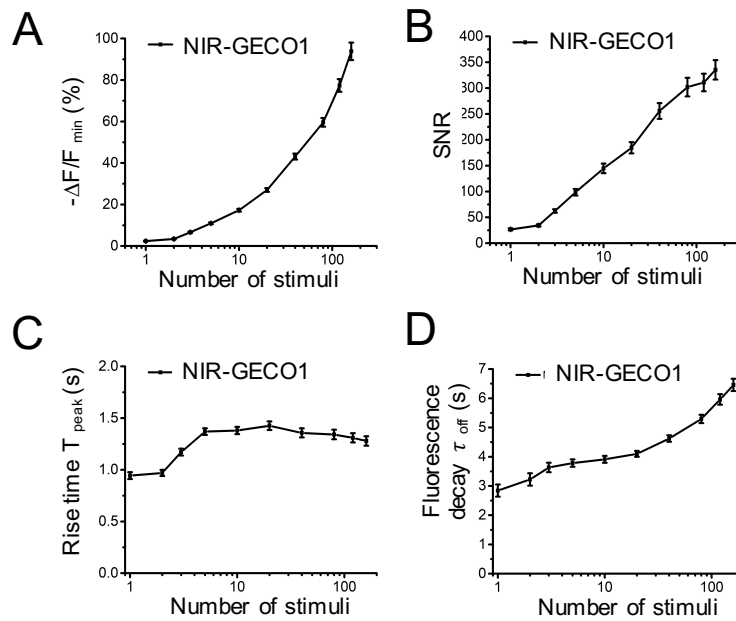


Figure 3.10. Quantification data of NIR-GECO1 fluorescence responses to field stimulation in cultured mouse hippocampal neurons.

NIR-GECO1 response amplitude (A), signal-to noise ratio (SNR) (B), rise time (actually a fluorescence decrease) for Ca^{2+} binding dissociation (C) and decay time (actually a fluorescence increase) for Ca^{2+} dissociation (D), as a function of the number of field stimulation-induced action potentials. Center values are mean, and error bars are s.e.m. $n = 55$ neurons.

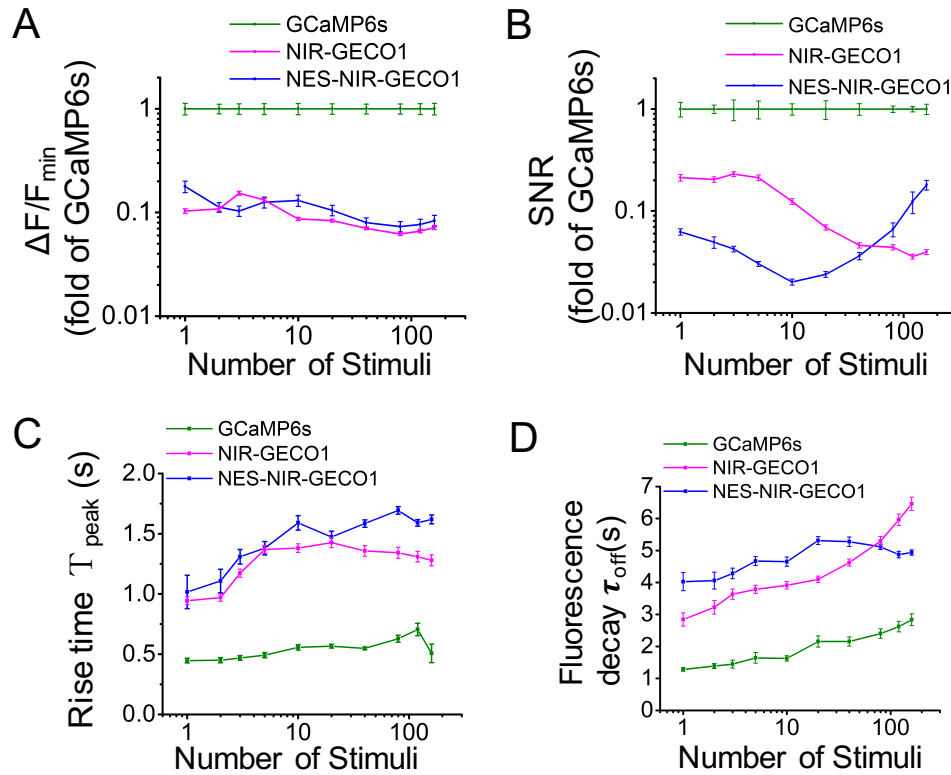


Figure 3.11. Fluorescence-response comparison of NIR-GECO1, NES-NIR-GECO1 and GCaMP6s in cultured mouse hippocampal neurons.

(A) Response amplitude of NIR-GECO1 ($n = 55$ neurons) and NES-NIR-GECO1 ($n = 147$ neurons) as a fraction of GCaMP6s ($n = 31$ neurons). The average $\Delta F/F_{\min}$ of NIR-GECO1 was $2.4 \pm 0.12\%$, $3.4 \pm 0.16\%$, $6.6 \pm 0.29\%$, $11 \pm 0.44\%$, $17 \pm 0.65\%$, $27 \pm 0.9\%$, $43 \pm 1.4\%$, $60 \pm 2.0\%$, $77 \pm 3.0\%$, and $94 \pm 4.2\%$ for 1, 2, 3, 5, 10, 20, 40, 80, 120 and 160 APs, respectively. Relative to GCaMP6s, the $\Delta F/F_{\min}$ of NIR-GECO1 was 10% of GCaMP6s for 1 and 2 APs and increased to 15% and 13% for 3 and 5 APs and then went down to 7% for APs from 10 to 160 APs. Elsewhere in the chapter, we have consistently used $\Delta F/F_0$ to describe fluorescence changes. Here we use $\Delta F/F_{\min}$ to enable the values for NIR-GECO1

and GCaMP6s to be easily compared. **(B)** Signal-to-noise ratio (SNR) of NIR-GECO1 and NES-NIR-GECO1 compared to GCaMP6s. The SNR of NIR-GECO1 was 26.7 ± 1.98 , 34.4 ± 2.15 , 62.2 ± 3.42 , 98.6 ± 6.37 , 145 ± 9.29 , 185 ± 10.9 , 256 ± 15.3 , 302 ± 18.0 , 311 ± 16.9 and 335 ± 18.8 for 1, 2, 3, 5, 10, 20, 40, 80, 120 and 160 APs, respectively. Relative to GCaMP6s, the SNR of NIR-GECO1 was 20% of GCaMP6s for APs from 1 to 5 and then goes down to 12% to 4% of GCaMP6s for APs from 10 to 100. **(C)** Fluorescence rise time of NIR-GECO1 and NES-NIR-GECO1 (actually a fluorescence decrease) compared to GCaMP6s for binding of Ca^{2+} . The average rise time of NIR-GECO1 was 0.94 ± 0.033 s, 1.4 ± 0.038 s, 1.4 ± 0.044 s for 1, 10 and 40 APs. **(D)** Fluorescence decay time of NIR-GECO1 and NES-NIRGECO1 (actually a fluorescence increase) compared to GCaMP6s for dissociation of Ca^{2+} . The average decay time of NIR-GECO1 was 2.8 ± 0.21 s, 3.9 ± 0.12 s, 4.6 ± 0.11 s for 1, 10 and 40 APs. For **A–D**, the NIR-GECO1 data are identical to data represented in **Fig. 3.10 A–D**. For **A–D**, center values are the mean, and error bars are s.e.m. $n = 55$ neurons for NIR-GECO1, $n = 147$ neurons for NES-NIR-GECO1, and $n = 31$ neurons for GCaMP6s.

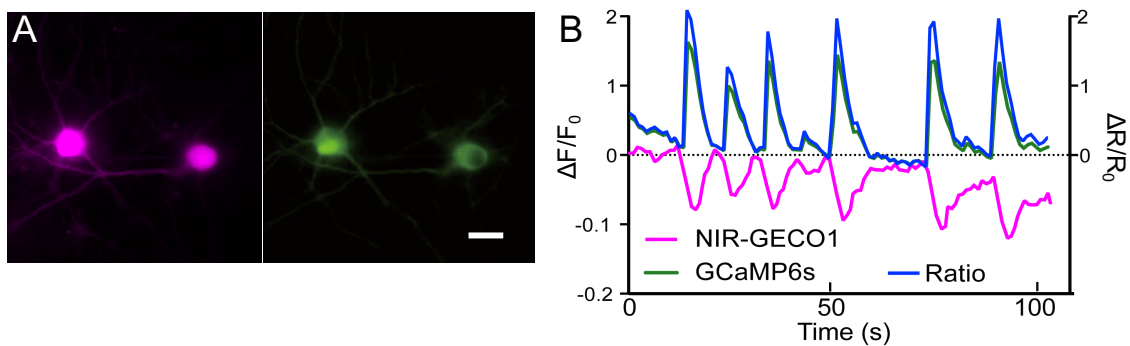


Figure 3.12. Co-expression of NIR-GECO1 and GCaMP6s in cultured rat cortex neurons.

(A) Representative wide-field fluorescence images of coexpressed NIR-GECO1 (left) and GCaMP6s (right). $n = 5$ neurons from two cultures. Scale bar, 20 μm . (B) Spontaneous Ca^{2+} oscillations in dissociated cortical neurons coexpressing NIR-GECO1 and GCaMP6s (NIR channel, 650/60 nm Ex and 720/60 nm Em; green channel, 490/15 nm Ex and 525/50 nm Em; acquisition rate is 1 Hz). Also shown is $\Delta R/R_0$, where R is the normalized GCaMP6s intensity divided by normalized NIR-GECO1 intensity. $n = 5$ neurons from two cultures.

3.3.6 Imaging of *in vivo* expressed NIR-GECO1

To evaluate *in vivo* expression of NIR-GECO1, we induced expression of the gene in layer 2/3 (L2/3) of mouse motor cortex via *in utero* electroporation (IUE). Imaging of brain slices revealed fluorescence through neuronal cell bodies and processes (**Figure 3.13A** and **Figure 3.13C**) and no punctate structures. Stimulation of action potentials with whole-cell patch-clamp electrophysiology gave $-\Delta F/F_0$ of $7.2 \pm 2.8\%$, $13.4 \pm 3.8\%$ and $27.6 \pm 2.8\%$ for 5, 10 and 20 action potentials, respectively (**Figure 3.13B** and **Figure 3.13D**). We next investigated the performance of NIR-GECO1 under pharmacological stimulation by 4-aminopyridine (4-AP), which blocks voltage-gated K^+ channels and facilitates Ca^{2+} influx through voltage sensitive Ca^{2+} channels^{176,177}. Upon treatment of 4-

aminopyridine, neurons expressing NIR-GECO1 underwent mean maximal $-\Delta F/F_0$ of $\sim 20\%$ and mean averaged $-\Delta F/F_0$ of $\sim 10\%$ (**Figure 3.14A, B**).

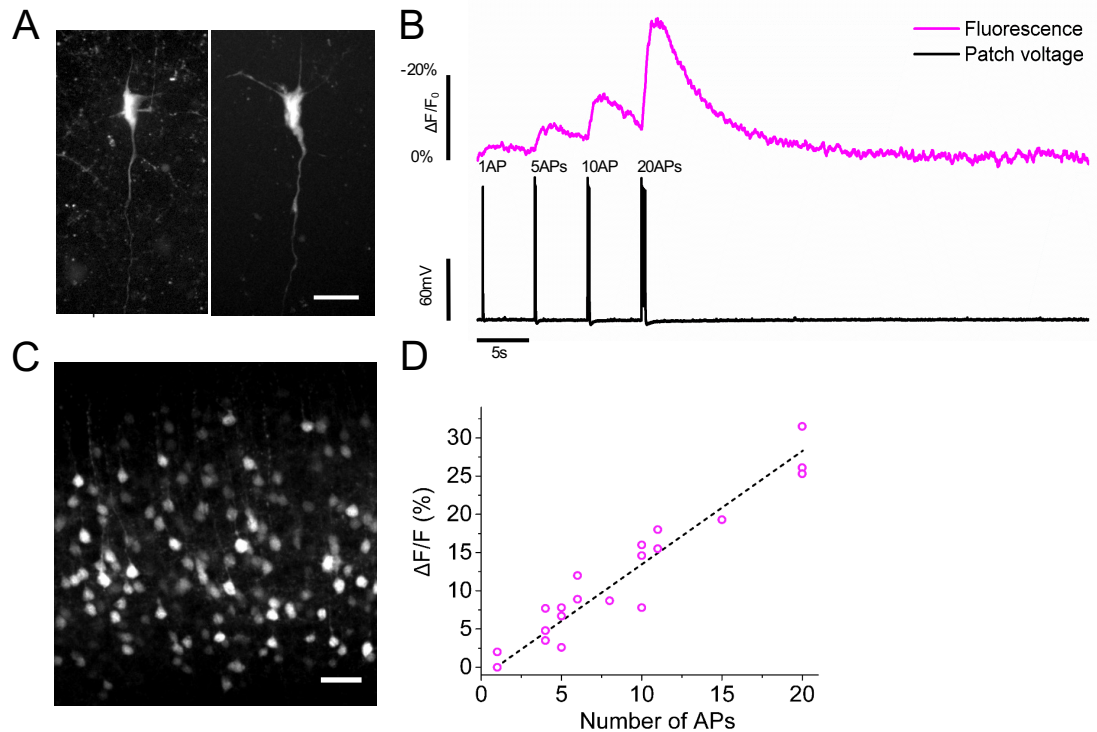


Figure 3.13. Characterization of NIR-GECO1 in intact brain tissues using whole-cell-patch clamp electrophysiology.

(A) Representative confocal images of neurons in L2/3 of motor cortex expressing NIR-GECO1 (641 nm Ex and 664LP Em; $n = 4$ slices from 2 mice). Scale bar, 15 μm . Such neurons were imaged during electrophysiological current injections as in B. (B) Representative single-trial wide-field optical recording of NIR-GECO1 fluorescence responses (magenta; 631/28 nm Ex and 664LP Em; acquisition rate 50 Hz) to 1, 5, 10, and 20 action potentials trains evoked by current injections in neurons in L2/3 of motor cortex (as in b; $n = 6$ neurons from 4 mice at P11-22). Patch voltage is shown in black. (C) Representative confocal image of live brain

slice expressing NIR-GECO1 (641 nm Ex; 664LP Em; $n = 4$ slices from two mice at P11–22). Scale bar, 50 μm . **(D)** NIR-GECO1 fluorescence responses to action potential (AP) trains evoked by current injections ($n = 6$ neurons from four mice at P11–22; dashed line indicates linear regression). For experiments **A–D**, NIR-GECO1 was expressed *in vivo* by IUE at 15.5.

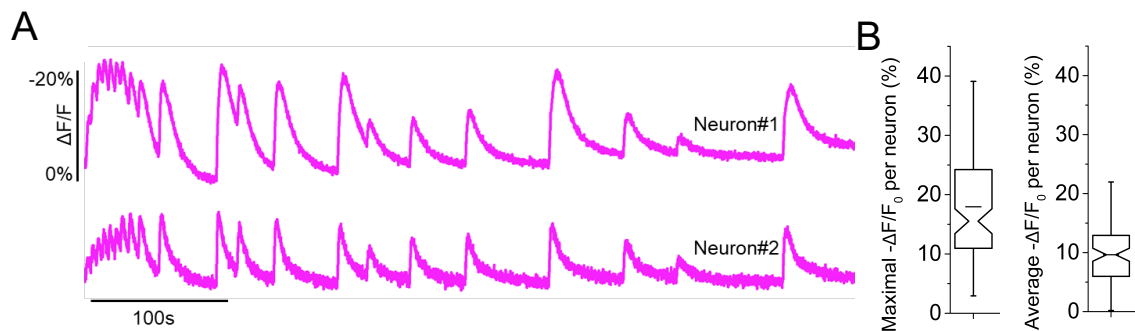


Figure 3.14. Characterization of NIR-GECO1 in intact brain tissues under pharmacological stimulation.

(A) Single-trial wide-field imaging of 4-aminopyridine (1 mM final concentration) evoked neuronal activity from the cell bodies of two representative neurons (631/28 nm Ex and 664LP Em; acquisition rate 20 Hz; $n = 129$ neurons from two slices from one mouse). **(B)** Maximal (left) and average (right) $-\Delta F/F_0$ for the experiment of **A**. Box plots are used as described in **Figure 3.7B**. For experiments in **A** and **B**, NIR-GECO1 was expressed *in vivo* by IUE at E15.5.

To determine whether NIR-GECO1 could be used for one-photon *in vivo* imaging, we injected adeno-associated virus (AAV) carrying the NIR-GECO1 gene (AAV2/9-hSyn1-NIR-GECO1) in the sensorimotor cortex of mice. Mesoscale

fluorescence imaging through the intact skin (hair removed) and skull of anesthetized mice during two paradigms of paw stimuli revealed transient stimuli- and NIR-GECO1-dependent fluorescence changes (decreases). Specifically, when a single 50-ms pulse (0.5 mA) was applied, we observed ~0.12% fluorescence decrease (**Figure 3.15B-D**), and when 10 pulses within 700 ms (0.5mA, 20ms on, 50ms off) was applied, the decrease of NIR-GECO1 fluorescence went up to ~0.3% (**Figure 3.15E-G**). Under similar conditions, GCaMP6s exhibited approximately tenfold greater fluorescence changes (increases) (**Figure 3.16 B, C**). We attribute the better performance of GCaMP6s to its inherently larger Ca^{2+} -dependent fluorescence response ($\times 30$ versus $\times 8$ under identical conditions; **Table 3.2**), its higher Hill coefficient (2.4 versus 1.0) and lower K_d (144 versus 215 nm) that has been empirically optimized for neuronal activity imaging. As expected, miRFP expressed mice and PBS injected mice (both were negative controls) showed no fluorescence changes after similar stimulations (**Figure 3.15 D-G**).

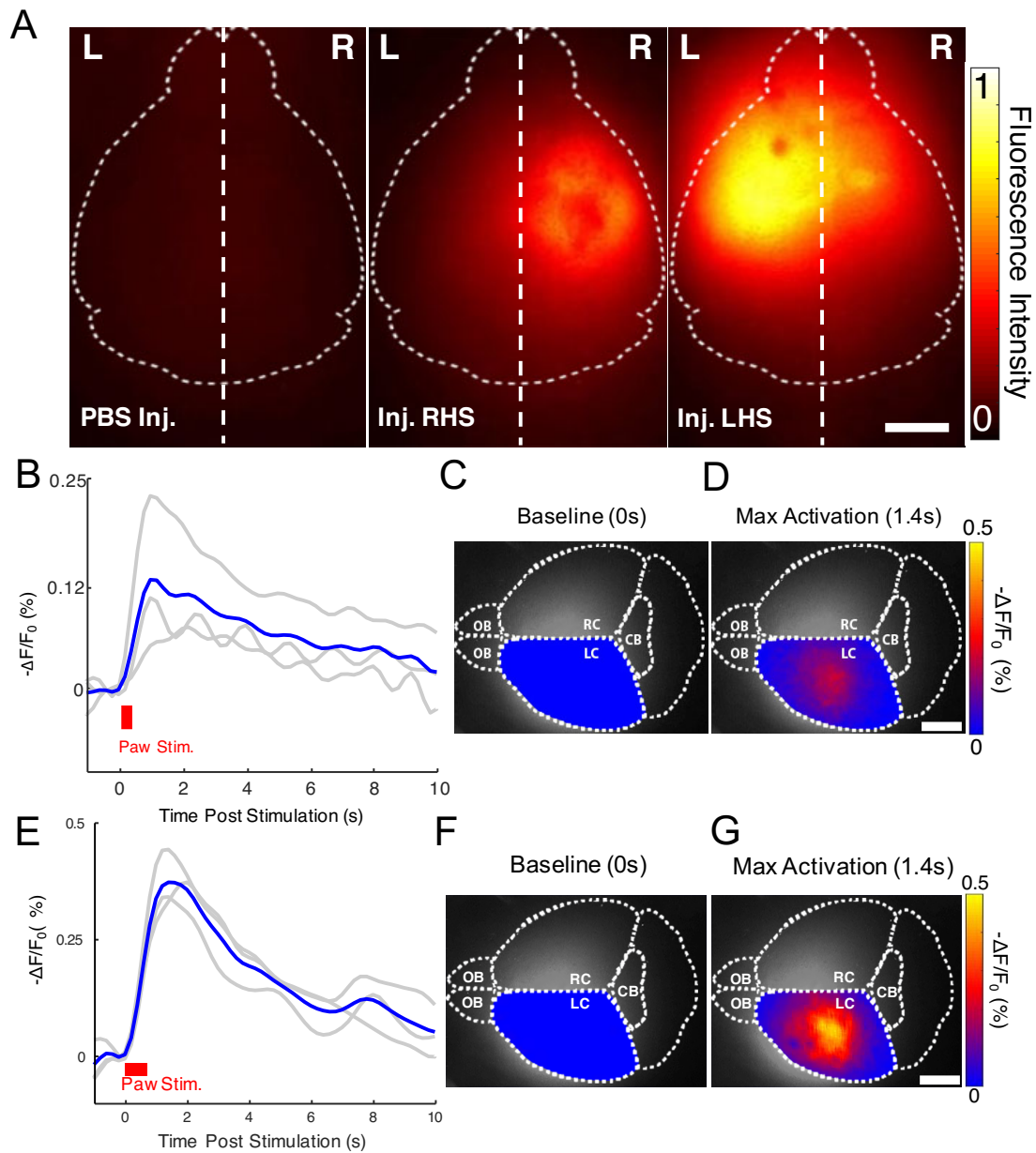


Figure 3.15. *In vivo* mesoscale imaging of footshock responses in mice using NIR-GECO1.

Three mice (4 weeks old) were injected with AVV2/9-hSyn1-NIR-GECO1 in either the right or the left side of the brain and imaged (671 nm Ex; 721/42 nm Em) 10–21 days later. **(A)** Mesoscale fluorescence images (671 nm Ex and 721/42 nm Em) of the mouse sensorimotor cortex injected with AAV2/9-hSyn1-NIR-GECO1). Left,

negative control with no viral expression on the right side of mouse brain (PBS injection). Middle, viral expression of NIR-GECO1 on the right side of mouse brain. Right, viral expression of NIR-GECO1 on the left side of mouse brain. Scale bar, 2 mm. **(B)** Fluorescence response of NIR-GECO1 in response to a paw stimulation paradigm with a single 50-ms pulse (0.5 mA). Each gray line represents the averaged response of a mouse across 19 cycles, and the blue line represents the mean response from all 3 mice ($n = 3$, or $3 \times 19 = 57$ cycles). **(C)** Activation map of mouse brain before stimulation from experiments in **B**. The estimated brain outline was manually superimposed onto the fluorescence images to facilitate determining the site of injection and activation in relation to bregma and the sensorimotor cortex. **(D)** Activation map of mouse brain at max activation from experiments in **B**. Scale bar, 2 mm. **(E)** Response to a paw stimulation paradigm of ten pulses in 700 ms (0.5 mA, 20 ms on and 50 ms off). As in **B**, each gray line represents the averaged response of a mouse across 19 cycles, and the blue line represents the mean response from all three mice ($n = 3$; that is, 57 cycles). **(F)** Activation map of mouse brain, injected in left cortex, before stimulation from experiments in **E**. Diffuse fluorescence in the right cortex is attributed to diffusion of viral particles and light scattering. **(G)** Activation map of mouse brain at max activation 1.4 s after stimulation from experiments in **E**. Scale bar, 2 mm. OB, olfactory bulb; CB, cerebellum; L/RC, left or right cortex.

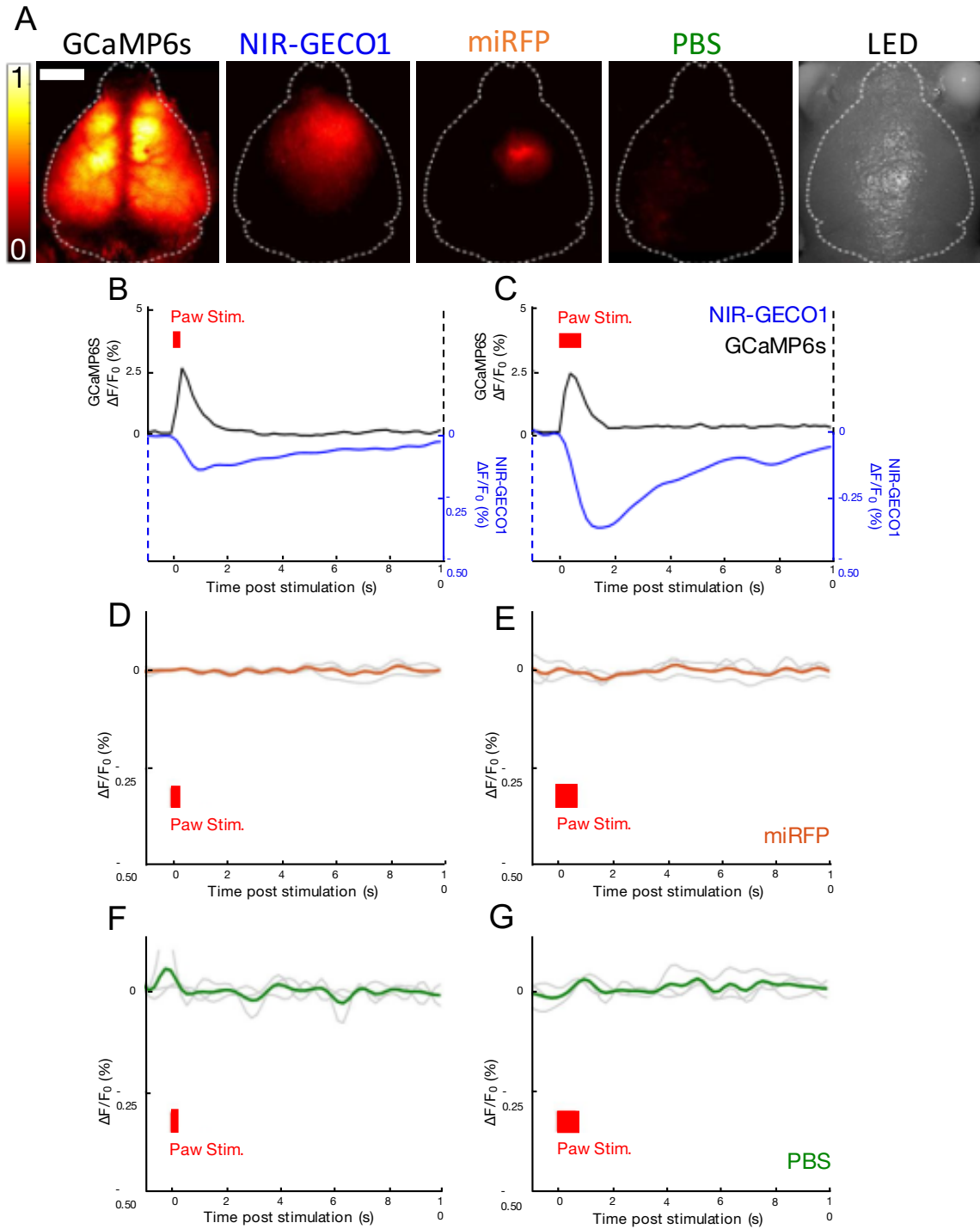


Figure 3.16. Control experiments for *in vivo* mesoscale imaging using GCaMP6s and miRFP.

(A) Comparative fluorescence images of a transgenic B16-GCaMP6s mouse and FoxN1 nude NIR-GECO1, miRFP and PBS injected mice. All fluorescence images are normalized to the GCaMP image shown. Direct comparison of the NIR-GECO1 and miRFP brightness is complicated by the fact that the AAVs were different serotypes (AAV2/9 and AAV2, respectively) and the NIR-GECO1 stock had 10 \times more genome copies/mL. Also shown is a representative white light image of the imaging area. Scale bar, 2 mm. (B, C) Positive control experiment with imaging of GCaMP6s in response to paw stimulations. For B, a stimulation paradigm of a single 50-ms pulse (0.5 mA) was used. For C, a stimulation paradigm of 10 pulses in 700 ms (0.5 mA, 20 ms on and 50 ms off) was used. The mean value from 3 mice is shown in each case. NIR-GECO1 curves are the same as in **Figure 3.14B** and **3.14E**. (D, E) A negative control experiment with imaging of miRFP fluorescence in response to paw stimulations. Stimulations in D and E are the same as in B and C, respectively. Orange line represents the mean value from 3 mice, and gray lines represent the average response of 1 mouse across 19 cycles. (F, G) A negative control with fluorescence imaging PBS-injected mouse in response to paw stimulations. Filter set is the same as for NIR-GECO1. The green line represents the mean value of 3 measurements (an average of 19 cycles) from 2 mice, and the gray lines represent the average response averaged for 1 mouse measured once and 1 mouse measured twice. Stimulations in F and G are the same as in B and C, respectively. The GCaMP6s mice are a transgenic line, and the mice were approximately 2 months older than other mice used in these experiments.

3.3.7 Multiplexed imaging of NIR-GECO1 in combination with optogenetic actuators and fluorescent-protein-based indicators.

Owing to its spectrally distinct fluorescence, NIR-GECO1 should be particularly useful for *in vitro* imaging in combination with optogenetic actuators and fluorescent-protein-based indicators. To explore such applications, we attempted two-photon imaging of NIR-GECO1 and GCaMP6f. NIR-GECO1 two-photon brightness at both 1,250 nm and 880 nm excitation is sufficient to image neurons in culture and in mouse brain tissue *ex vivo* and *in vivo* (**Figure 3.17 A, B** and **Figure 3.18**). With 1,250 nm excitation we observed neuronal-activity-dependent changes in NIR-GECO1 fluorescence in cultured neurons, as confirmed by coexpression of GCaMP6f, with average $-\Delta F/F_0$ of $48 \pm 28\%$ ($n = 37$ neurons from one culture; **Figure 3.17C**). With two-photon excitation at 880 nm (11.4 mW of total light power), both the intracellular brightness and the photostability of NIR-GECO1 ($t_{1/2} = 20$ s) were slightly higher than those of mRFP, but lower than those of iRFP682 (**Figure 3.18A, B**). However, when we used 880 nm excitation, we did not observe characteristic fluorescence changes of NIR-GECO1 associated with neuronal Ca^{2+} dynamics in neurons either in culture or in live brain slices (**Figure 3.18C**). We have not succeeded in demonstrating *in vivo* imaging of neuronal activity using NIR-GECO1 with either 880 nm or 1,250 nm two-photon excitation.

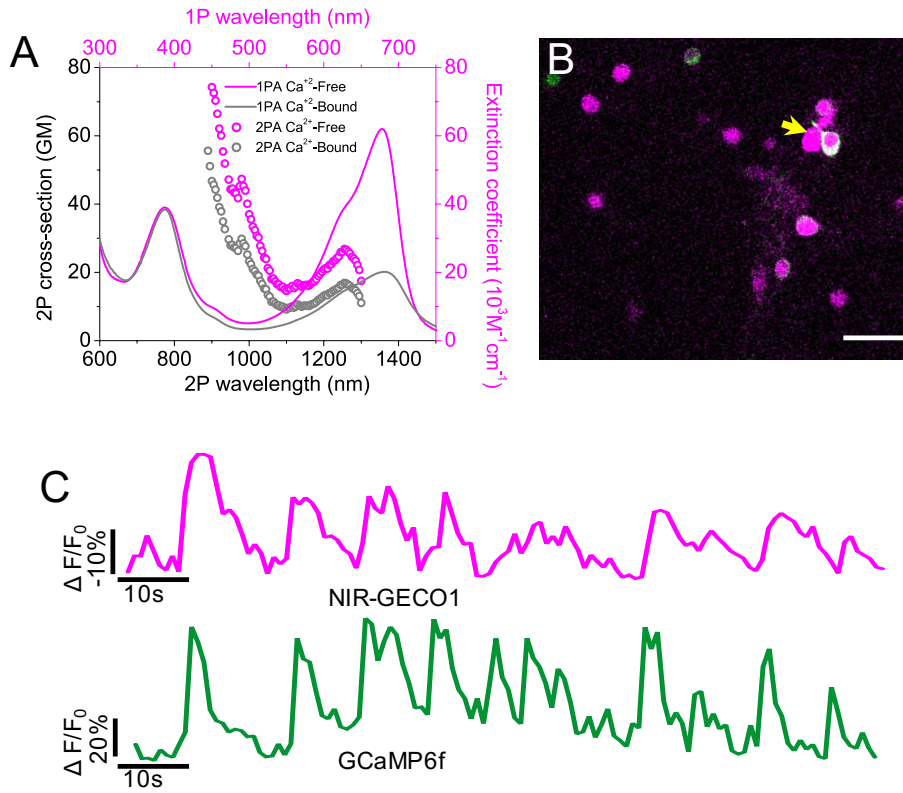


Figure 3.17. Two photon imaging of NIR-GECO1 with GCaMP6f in cultured mouse hippocampal neurons.

(A) One-photon (solid line; identical to Figure 3.6A) and two-photon (open circles) absorption spectra of NIR-GECO1 in the presence and absence of Ca²⁺. Two-photon absorption spectra are presented versus laser wavelength used for excitation. GM, Goeppert–Mayer units. (B) Representative fluorescence image of cultured neurons expressing NIR-GECO1 (magenta) and GCaMP6f (green) acquired under two-photon excitation (imaging condition: NIR-GECO1 1,250 nm Ex, 705/90 nm Em; GCaMP6f 920 nm Ex, 518/45 nm Em; *n* = 2 cultures). Scale bar, 50 μm. (C) Representative single-trial fluorescence recording of 4-aminopyridine (1 mM final concentration) evoked neuronal activity using NIR-

GECO1 and GCaMP6f under imaging conditions as in **B** ($n = 32$ neurons from two cultures; yellow arrow indicates the neuron the fluorescence traces were obtained from; image acquisition rate, 1 Hz).

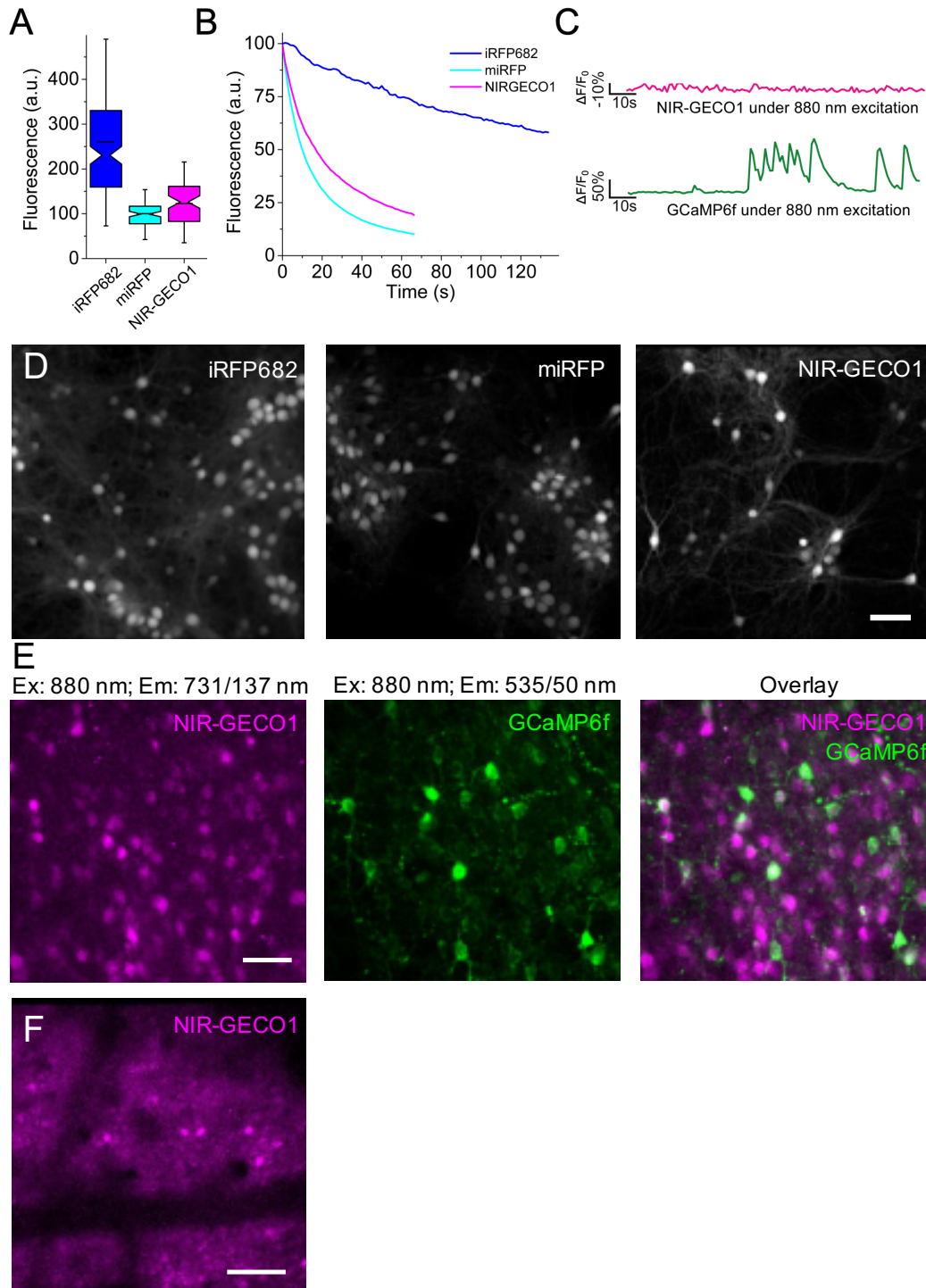


Figure 3.18. Two-photon fluorescence microscopy of NIR-GECO1.

BV-FPs can be visualized using two-photon fluorescence microscopy¹⁷⁵, a widely used technique for *in vivo* Ca²⁺ imaging. **(A)** Relative normalized fluorescence and **(B)** raw photobleaching curves for iRFP682 (blue), miRFP (cyan), and NIR-GECO1 (magenta) in cultured mouse neurons ($n = 184, 106, \text{ and } 77$ cells, respectively, from one culture) under 880 nm two-photon excitation and 4.05 mW of total light power. For **A**, a box plot with notches is used as described in **Figure 3.7B**. **(C)** Representative fluorescence recording of 4-aminopyridine (1 mM final concentration)-evoked neuronal activity using NIR-GECO1 and GCaMP6f fluorescence under 880 nm two-photon excitation. Excitation for both NIR-GECO1 and GCaMP6f was 880 nm, and emission filters for NIR-GECO1 and GCaMP6s were 705/90 nm and 518/45 nm, respectively. **(D)** Representative two-photon fluorescence images of cultured mouse neurons expressing iRFP682 (left), miRFP (middle) and NIR-GECO1 (right), under 880 nm two-photon excitation (731/137 nm Em; $n = 184, 106, \text{ and } 77$ cells, respectively, from one culture). Scale bar, 50 μm . **(E)** Two-photon fluorescence images of live mouse brain slice coexpressing NIR-GECO1 (left; magenta) and GCaMP6s (middle; green) under 880 nm excitation (right, overlay). $n = 2$ slices from one mouse. Scale bar, 50 μm . **(F)** *In vivo* two-photon microscopy of NIR-GECO1-expressing neurons in mouse primary visual cortex. $n = 3$ fields of view from one mouse. Scale bar, 50 μm .

Due to its highly red-shifted spectral properties (**Figure 3.6 A, B**), the excitation light required for NIR-GECO1 fluorescence is completely separated from the action

spectra of commonly used blue/cyan-light activated optogenetic actuators (*i.e.*, CoChR, **Figure 3.19 A**). To explore the combined use of NIR-GECO1 and an optogenetic actuator, we prepared live brain slices expressing NIR-GECO1 and the high-photocurrent channelrhodopsin CoChR^{114,178} (**Figure 3.19 A**). Activation of CoChR with cyan-colored light produced Ca²⁺ transients that were reliably reported by NIR-GECO1 (**Figure 3.19 B, C**), suggesting that combination of NIR-GECO1 and CoChR is feasible for all-optical controlling and imaging neural activity.

In cultured mouse hippocampal neurons coexpressing NIR-GECO1 and CoChR, we demonstrated that both cyan-color light (475/34 nm, common light source for excitation of green fluorescent indicators) and orange-colored light (562/40 nm, common light source for excitation of red fluorescent indicators) could trigger neuronal Ca²⁺ transients and there was no evidence of photophysical artifacts attributable to the illumination conditions¹⁷⁹, which suggests that both green and red fluorescent GECIs are not practical for combination with cyan-color light activated optogenetic actuators (*i.e.*, CoChR) (**Figure 3.20A-C**).

We also coexpressed NIR-GECO1 with another cyan-color light activated channelrhodopsin CheRiff¹³¹ in cultured neurons and observed robust Ca²⁺ transients after 10 ms cyan light (490/20 nm) illumination (**Figure 3.21A, B**).

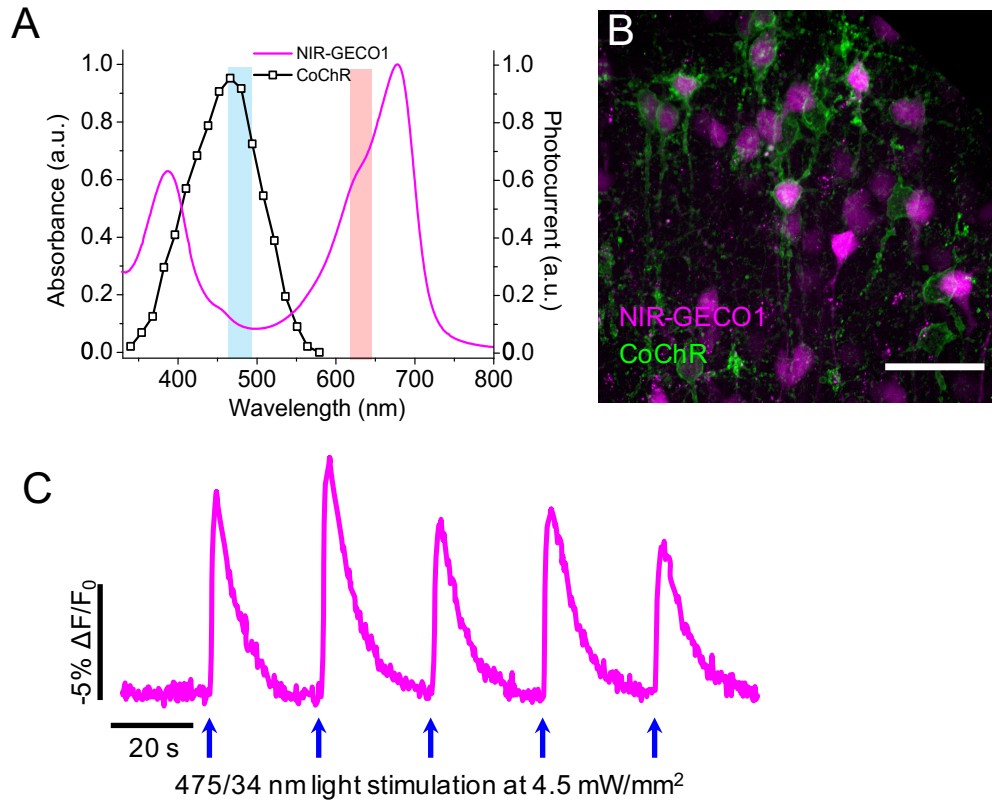


Figure 3.19. Combined use of CoChR and NIR-GECO1 in acute brain slices for optogenetic stimulation and imaging of activity.

(A) Action spectrum of channelrhodopsin from *Chloromonas oogama* (CoChR) (black line; adapted with permission from Ref. 178) and NIR-GECO1 absorbance spectrum (magenta line; identical to **Figure 3.6A** with no free Ca^{2+}) with wavelengths used for CoChR activation (475/34 nm; cyan bar) and NIR-GECO1 excitation (638/14 nm; orange bar). (B) Representative confocal images of neurons in L2/3 of motor cortex coexpressing NIR-GECO1 (magenta) and CoChR-mTagBFP2-Kv2.2motif (green) targeted by IUE at E15.5 (imaging conditions: NIR-GECO1, 641 nm Ex, 664LP Em; CoChR-mTagBFP2-Kv2.2motif, 405 nm Ex and 452/45 nm Em). Scale bar, 50 μ m. Representative of $n = 9$ slices from 2 mice. (C)

Single-trial wide-field imaging of NIR-GECO1 responses to CoChR activation (fluorescence excitation and activation as in d; 664LP Em; blue arrows, CoChR stimulation with 200 ms light pulses; image acquisition rate 5 Hz). Representative of $n = 9$ slices from 2 mice.

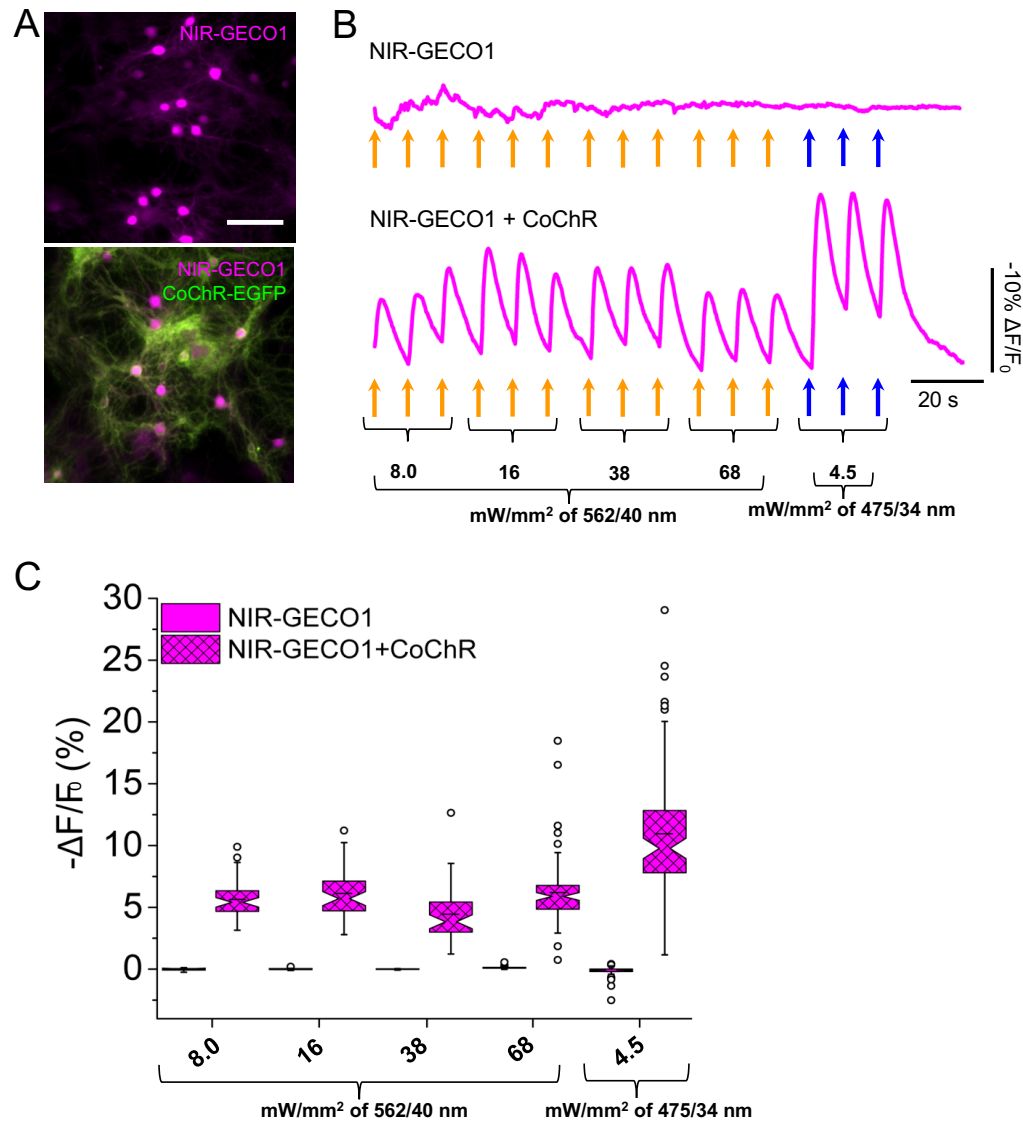


Figure 3.20. Combined use of CoChR and NIR-GECO1 in cultured neurons for optogenetic stimulation and imaging of activity.

(A) Representative wide-field fluorescent images of cultured hippocampal mouse neurons expressing NIR-GECO1 (top; magenta; 631/28 nm Ex and 664LP Em), and both NIR-GECO1 (magenta; 631/28 nm Ex and 664LP Em) and CoChR-EGFP (green; bottom; 475/34 nm Ex and 525/50 nm Em). Scale bar, 50 μ m. (B) Representative single trial traces for single neurons (as in a; $n = 45$ and 93 neurons for NIR-GECO1 and NIR-GECO1 + CoChR-EGFP, respectively, from two cultures) illuminated with 562/40 nm (orange arrows) or 475/34 nm (blue arrows) at indicated light intensities with 200-ms duration per pulse. (C) Quantification of NIR-GECO1 fluorescence changes in response to activation of CoChR under the conditions described in B ($n = 45$ and 93 neurons for NIR-GECO1 and NIR-GECO1 + CoChR-EGFP, respectively, from 2 cultures). Box plots with notches are used as described in **Figure 3.7B**.

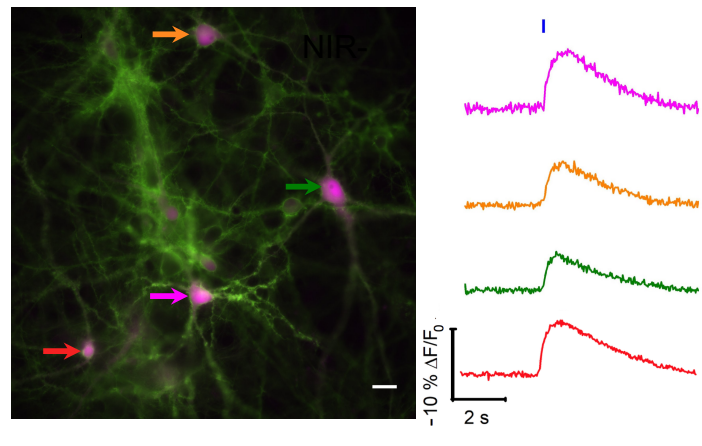


Figure 3.21. Combined use of CheRiff and NIR-GECO1 in cultured neurons for optogenetic stimulation and imaging of activity.

(A) Image of cultured mouse hippocampal neurons expressing CheRiff-EGFP (green, 480 nm Ex and 525/36 nm Em) and NIR-GECO1 (magenta, 640 nm Ex and 705/50 nm Em). CheRiff is localized to the plasma membrane, whereas NIR-GECO1 fills the cytoplasm and nucleus of the neurons. Scale bar, 20 μm . **(B)** NIR-GECO1 fluorescence traces from 4 neurons, indicated with correspondingly colored arrows in **A**, in response to optical stimulation. Blue bar indicates a 10-ms blue light (490/20 nm at 4 mW/mm²) illumination. Experiments were repeated more than 10 times with similar results.

To demonstrate NIR-GECO1's utility for use with β -FP-based indicators, we performed three-indicator (four-color) imaging using NIR-GECO1, the CFP and YFP-based protein kinase A indicator AKAR4¹⁸⁰, and the RFP-based cAMP indicator Pink Flamindo¹⁸¹ to visualize multiple intracellular parameters simultaneously. In eukaryotic cells, both cAMP and Ca²⁺ are ubiquitous second messengers that regulate many cellular functions (*i.e.*, exocytosis, gene expression, cell migration, cardiac contractility and memory formation) through the interaction with various kinases (*i.e.*, protein kinase A), and the dynamics of cAMP, Ca²⁺ and kinases activity are often temporally correlated¹⁸²⁻¹⁸⁴. Therefore, real-time co-imaging of cAMP, Ca²⁺ with protein kinase A might be essential in determining the relative kinetics of cellular responses to extracellular stimuli. MIN6 β -cells expressing NIR-GECO1, AKAR4 and Pink Flamindo were pharmacologically stimulated with TEA (tetraethylammonium chloride, a K⁺ channels inhibitor that induces depolarization-dependent Ca²⁺ oscillations in insulin-secreting β -cell-like

cell lines¹⁸⁵) and rapid, synchronous oscillations of Ca^{2+} , cAMP and PKA activity were observed (**Figure 3.22**, **Figure 3.23**), indicating a close temporal coupling between Ca^{2+} , cAMP and PKA.

We next co-expressed GCaMP6f⁵³, RCaMP1.07 (Ref. 186) and NIR-GECO1 in cultured mouse hippocampal neurons (**Figure 3.24A**) and obtained three-color Ca^{2+} imaging reporting neuronal spontaneous activity (**Figure 3.24B**). One possible use of combination of NIR-GECO1 with other GECIs is to get ratiometric images by dividing signals from positively changed green or red GECIs by that of negatively changed NIR-GECO1 (as demonstrated in **Figure 3.12B**).

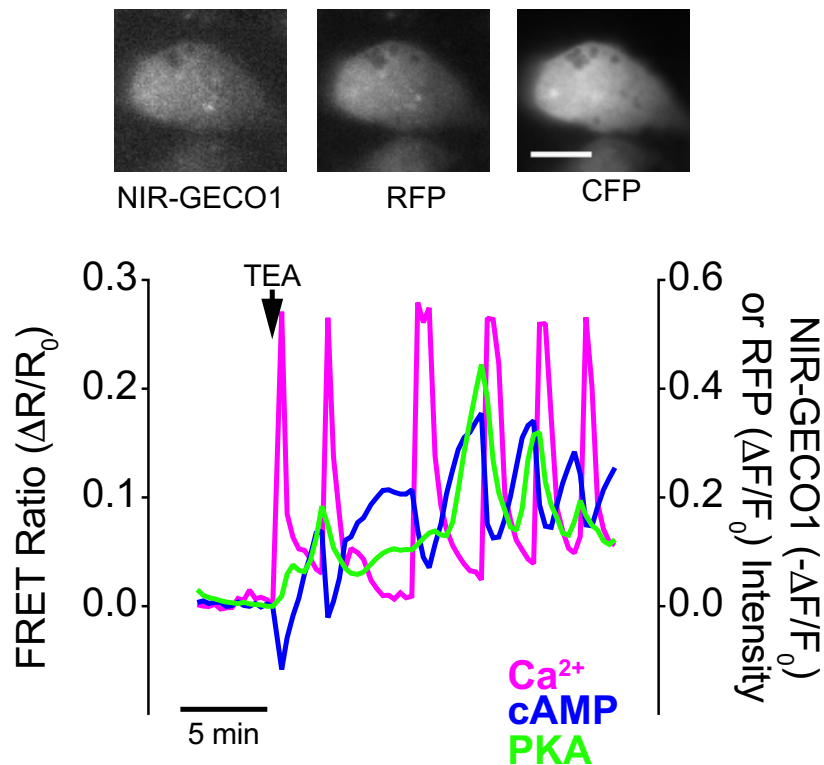


Figure 3.22. Multi-color imaging of NIR-GECO1 in combination with AKAR4 and Pink Flamindo.

Top, representative fluorescence images of MIN6 β -cell coexpressing AKAR4 (left, 420/20 nm Ex and 475/40 nm Em for CFP and 535/25 nm Em for YFP), NIR-GECO1 (middle, 640/30 nm Ex and 700/75 nm Em) and Pink Flamindo (right, 555/25 nm Ex and 605/52 nm Em). Scale bar, 10 μ M. Bottom, simultaneous visualization of Ca^{2+} (NIR-GECO1; $-\Delta F/F_0$, magenta line), cyclic AMP (Pink Flamindo; $\Delta F/F_0$, blue line), and PKA (AKAR4; FRET emission ratio $\Delta R/R_0$, green line) in a MIN6 cell treated with 20 mM tetraethylammonium chloride (TEA) at $t = 0$ (arrow)

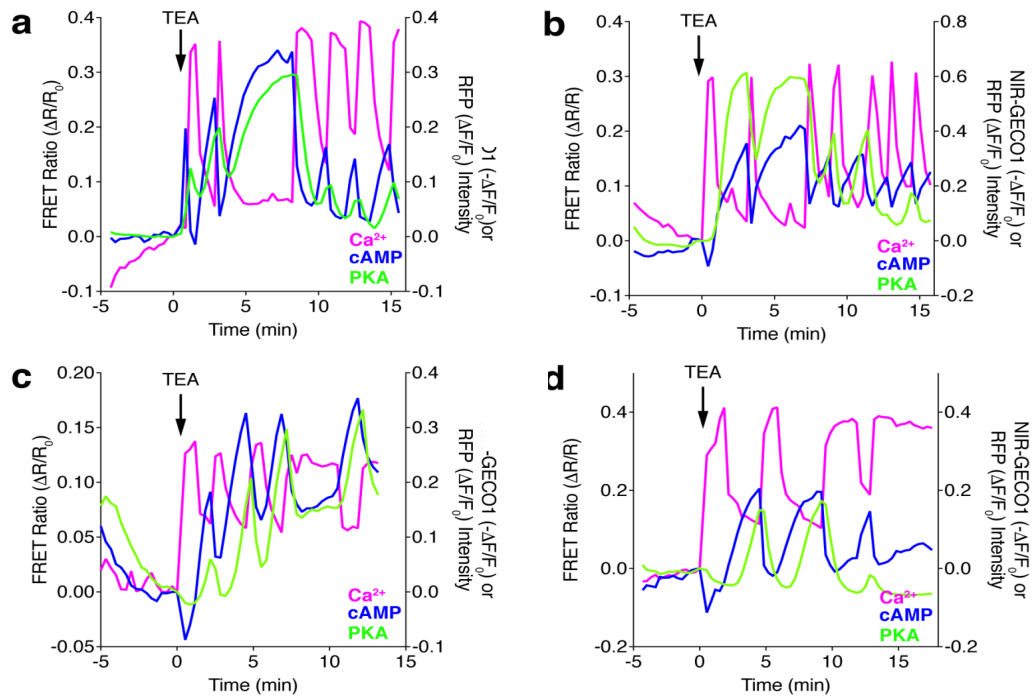


Figure 3.23. Additional representative single-cell traces for multiplexed imaging of MIN6 β -cells.

Conditions are identical to those described for Figure 3.21.

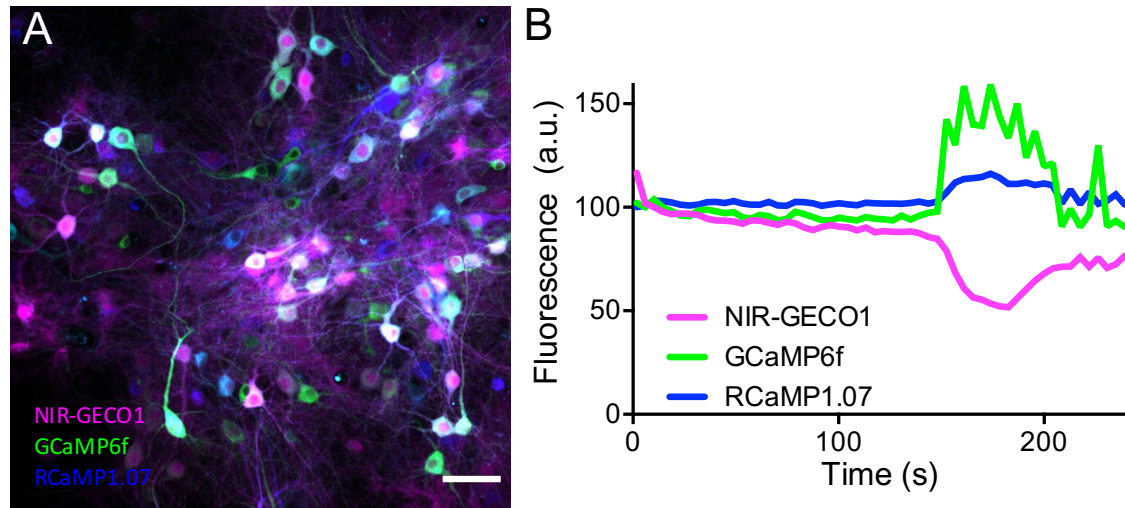


Figure 3.24. Multi-color imaging of NIR-GECO1 in combination with GCaMP6f and RCaMP1.07.

(A) Representative overlaid fluorescence image of dissociated neurons coexpressing NIR-GECO1, GCaMP6f and RCaMP1.07. (B) Simultaneous detection of spontaneous neuronal activity reported by GCaMP6f, RCaMP1.07 and NIR-GECO1, in a single cell as in A. The percentage of responding cells (during a 3-min imaging session) was 92% for GCaMP6f ($n = 271$ neurons), 79% for RCaMP1.07 ($n = 178$ neurons) and 59% for NIR-GECO1 ($n = 331$ neurons).

3.4 Conclusion

We have demonstrated that NIR-GECO1 is a useful new addition to the GEC1 palette. As a first-generation indicator, NIR-GECO1 falls short of the most extensively optimized fluorescent-protein-based GECs in several critical performance parameters. Accordingly, NIR-GECO1 is not generally useful for *in vivo* imaging of neuronal activity. However, NIR-GECO1 does provide a robust

inverse response to Ca^{2+} concentration changes in cultured cells, primary neurons and acute slices roughly on par with GCaMP3. In addition, because of its highly red-shifted excitation maximum, it is the preferred Ca^{2+} indicator for pairing with blue light-activated optogenetic actuators, to minimize actuator activation during imaging¹³⁰. Finally, it creates a multitude of new opportunities for multiparameter imaging in conjunction with multiple fluorescent-protein-based intensimetric or ratiometric FRET-based indicators. Much as how the β -FP-domain of R-GECO1 has been transplanted to create red fluorescent voltage¹⁸⁷, redox¹⁸⁸, cAMP¹⁸¹ and glutamate¹⁴⁶ indicators, the BV-FP domain of NIR-GECO1 should prove similarly versatile and lead to a new generation of far-red and NIR indicators for a wide variety of biochemical parameters.

As with many BV-FPs, NIR-GECO1 is substantially dimmer than state-of-the-art fluorescent-protein-derived GECIs such as GCaMP6s (10.7 times brighter)¹¹⁹ and jRGECO1a (three times brighter)¹³⁰. To enable general utility for *in vivo* imaging, future iterations of NIR-GECO1 should be optimized for brighter fluorescence (for example, improved BV-binding efficiency could provide up to an approximately five-fold increase), increased affinity for Ca^{2+} , increased photostability and faster kinetics. We expect NIR-GECO1 to be just as amenable to further improvements as the GCaMP series, and for these advancements to be soon realized through protein-engineering efforts.

3.5 Materials and methods.

3.5.1 General methods and materials.

Synthetic DNA oligonucleotides used for cloning and library construction were purchased from Integrated DNA Technologies. Q5 high-fidelity DNA polymerase (New England BioLabs) was used for routine PCR amplifications and Taq DNA polymerase (New England BioLabs) was used for error-prone PCR. QuikChange Mutagenesis Kit (Agilent Technologies) was used for site-specific mutagenesis. Restriction endonucleases were purchased from Thermo Fisher Scientific. PCR products and products of restriction digests were routinely purified using preparative agarose gel electrophoresis followed by DNA isolation using the GeneJET gel extraction kit (Thermo Fisher Scientific). Ligations were performed using T4 ligase in Rapid Ligation Buffer (Thermo Fisher Scientific). Small-scale isolation of plasmid DNA was performed by GeneJET miniprep kit (Thermo Fisher Scientific). All DNA sequences were confirmed by dye terminator cycle sequencing using the BigDye Terminator v3.1 Cycle Sequencing Kit (Applied Biosystems). Sequencing reactions were analyzed at the University of Alberta Molecular Biology Service Unit. Absorbance measurements were made with a DU-800 UV-visible spectrophotometer (Beckman) and fluorescence spectra were recorded on a Safire2 platereader (Tecan). AAVs were produced at the University of Laval Molecular Tools Platform.

3.5.2 Engineering of NIR-GECO1

The gene encoding mIFP (a gift from Michael Davidson and Xiaokun Shu; Addgene plasmid #54620)³⁶ was inserted between BamHI and EcoRI of a pBAD vector (Life Technologies) that expressed cyanobacteria *Synechocystis* HO-1 to convert an endogenous heme in bacteria into BV, as previously described^{35,189}. The DNA sequence encoding CaM and RS20 (a peptide that corresponds to the CaM-binding peptide of smooth muscle myosin light chain kinase; VDSSRRKWNKAGHAVRAIGRLSS) portions of REX-GECO1 (Ref. 134), with mutations Q306D and M339F borrowed from jRGECO1a¹³⁰, were genetically fused by overlap extension PCR using a DNA sequence that encodes for the flexible peptide linker GGGGS¹⁹⁰.

For each site (X) of mIFP targeted for CaM-RS20 insertion, the full-length gene (encoding mIFP_{1 to X}-CaM-RS20-mIFP_{X+1 to 320}) was assembled by overlap extension PCR and then inserted into the pBAD vector. Variants were expressed in *E. coli* strain DH10B (Thermo Fisher Scientific) in LB media supplemented with 100 µg ml⁻¹ ampicillin and 0.0016% L-arabinose. Proteins were extracted using B-PER bacterial protein extraction reagent (Thermo Fisher Scientific) and tested for fluorescence brightness and Ca²⁺-dependent response.

The most promising variant was subjected to an iterative process of library generation and screening in *E. coli*. The pBAD vector was used in the first three rounds. From the fourth round, pcDuEx2 was used to enable expression in both *E. coli* and mammalian cells. Libraries were generated by error-prone PCR of the whole gene¹⁹¹ or site-directed mutagenesis using Quikchange (Agilent Technologies) and degenerate codons at the targeted positions.

For libraries generated by random mutagenesis, approximately 10,000 colonies were screened in a given round. For libraries generated by randomization of one or more codons, a number of colonies that was approximately threefold the theoretical number of gene variants were screened. For each round, the top 2% of colonies with high fluorescence intensity were picked, cultured and tested on 396-well plates. Approximately 25% of those picked variants were further screened in HeLa cells on the basis of fluorescence. In a given round, screening was stopped when a substantially improved variant was identified. There were 12 rounds of screening before NIR-GECO1 was identified.

3.5.3 NIR-GECO1 expression vectors.

pcDuEx2 was constructed based on the pcDNA3.1 backbone. The Tac promoter and a gene sequence containing Kpn2I and XbaI sites was inserted immediately after CMV promoter by overlap extension PCR. A DNA fragment containing the T7 promoter, the gene encoding NIR-GECO1, and the gene encoding cyanobacteria *Synechocystis* HO-1, was amplified from the pBAD vector and inserted into the Kpn2I and XbaI sites.

For HeLa cell expression, the pcDuEx2 vector was used. For expression in dissociated neurons, either an AAV2 vector or a lentivirus containing NIR-GECO1 was used. For AAV2 vector preparation, NIR-GECO1 was cloned from pcDuEx2 into BamHI and HindIII sites of AAV2 vector (a gift from Roger Tsien; Addgene plasmid no. 50970)¹⁹². To create lentivirus expressing NIR-GECO1, the gene for

NIR-GECO1 or NIR-GECO1-T2A-HO1 was cloned into the BamHI and EcoRI sites of FCK lentivirus vector (Addgene plasmid no. 22217). HEK293FT cells at 80% confluency in 35-mm cell-culture dishes (Corning) were transfected with 1.5 µg FCK-CMV-NIR-GECO1 or FCK-CMV-NIR-GECO1-T2A-HO1, 1.0 µg psPAX2 (a gift from D. Trono, Addgene plasmid no. 12260), 0.5 µg pMD2.G (a gift from D. Trono, Addgene plasmid no. 12259), and 0.2 µg pAdvantage (Promega), with 9 µL Turbofect transfection reagent in 2 mL Opti-MEM medium (Thermo Fisher Scientific). Opti-MEM medium containing Turbofect and DNA mix were replaced with 2 mL complete cell-culture medium containing 110 mg/mL sodium pyruvate at 24 h post-transfection. At 48 h post-transfection, the virus-containing supernatant was collected, spun at 400g (relative centrifugal force (RCF)) for 5 min and filtered through a 0.45-µm PVDF Syringe Filter Unit (EMD Millipore) to get rid of pellet cellular debris. Dissociated neurons in 24-well plates were transduced with 2 mL virus-containing supernatant.

3.5.4 Protein purification and *in vitro* characterization

The gene encoding NIR-GECO1, with a poly-histidine tag on the C terminus, was expressed from the pBAD vector. Bacteria were lysed with a cell disruptor (Constant Systems Ltd) and then centrifuged at 15,000g for 30 min, and proteins were purified by Ni-NTA affinity chromatography (Agarose Bead Technologies). The buffer was typically exchanged to 10 mM MOPS, 100 mM KCl (pH 7.2) with centrifugal concentrators (GE Healthcare Life Sciences). We determined extinction

coefficients by comparing the absorbance value at 678 nm to the absorbance value at the 391 nm and assuming an extinction coefficient of $39,900 \text{ M}^{-1} \text{ cm}^{-1}$ at 391 nm^{30,36}. For determination of quantum yields (Φ), purified mIFP ($\Phi = 0.08$) was used as a standard. The concentration of NIR-GECO1 (Ca^{2+} -free), NIR-GECO1 (Ca^{2+} -saturated) and mIFP was adjusted to have absorbance of 0.2–0.6 at 650 nm. A series of dilutions, with absorbance ranging from 0.01 to 0.05, were prepared, and integrated emission intensity versus absorbance was plotted. Quantum yields were determined from the slopes (S) of each line using the equation $\Phi_{\text{protein}} = \Phi_{\text{standard}} \times (S_{\text{protein}}/S_{\text{standard}})$. We carried out pH titrations by diluting protein into buffers (pH from 2 to 11) containing 30 mM trisodium citrate, 30 mM sodium borate and either 10 mM CaCl_2 or 10 mM EGTA. Fluorescence intensities as a function of pH were then fitted by a sigmoidal binding function to determine the apparent pK_a . Ca^{2+} titrations were carried out using EGTA-buffered Ca^{2+} solutions (Calcium Calibration Buffer Kit no. 1, Life Technologies). We prepared buffers by mixing a CaEGTA buffer (30 mM MOPS, 100 mM KCl, 10 mM EGTA, 10 mM CaCl_2) and an EGTA buffer (30 mM MOPS, 100 mM KCl, 10 mM EGTA) to give free Ca^{2+} concentrations ranging from 0 nM to $39 \mu\text{M}$ at $25 \text{ }^\circ\text{C}$ ¹⁵¹. Fluorescence intensities were plotted against Ca^{2+} concentrations and fitted by a sigmoidal binding function to determine the Hill coefficient and K_d . To determine k_{off} , we used an SX20 stopped-flow spectrometer (Applied Photophysics). Briefly, protein samples with $10 \mu\text{M}$ CaCl_2 (30 mM MOPS, 100 mM KCl, pH 7.2) were rapidly mixed with 10 mM EGTA (30 mM MOPS, 100 mM KCl, pH 7.2) at room temperature, and an absorption growth curve was measured and fitted by a single exponential equation.

3.5.5 Two-photon spectral measurements.

Two-photon spectra and cross sections were measured using femtosecond excitation of fluorescence relative to known standards. The optical setup consists of a tunable femtosecond laser (DeepSee, InSight) coupled with a PC1 ISS fluorometer operating in photon-counting mode. The sample solution was continuously stirred in a 1 cm cuvette (Starna), and the laser beam was focused onto the sample with an achromatic lens ($f = 60$ mm, Qioptiq) close to the edge of the cuvette (~ 1 mm) to minimize the effects of solvent absorption. LDS798 (Exciton) in slightly alkaline CDCl_3 was used to correct for the two-photon spectral shape¹⁹³. LDS798 in CHCl_3 served as the standard for two-photon cross section measurements¹⁹³. Fluorescence of both the sample and the standard was excited at 1000 nm and recorded with the PC1 ISS monochromator at 720 nm. To eliminate possible errors resulting from independent measurements of the ECs and optical

densities of dilute solutions, the Strickler-Berg approach was used to calculate the cross sections, using Equation 9 in the Supplementary Information of Ref.¹⁹⁴. This approach relies on the fluorescence lifetime (τ) of the sample and the QY and EC of the two-photon standard (LDS798 in CHCl_3 , $\text{EC} = 41,000 \text{ M}^{-1}\text{cm}^{-1}$)¹⁹³. Rose Bengal (Sigma Aldrich) in MeOH served as a lifetime standard ($\tau = 0.519$ ns)¹⁹⁵. The fluorescence lifetimes of the samples were measured with the digital frequency domain technique (ChronosDFD, ISS) implemented with the PC1 ISS

fluorometer (NIR-GECO1 Ca^{2+} -saturated $\tau = 0.48$ ns, Ca^{2+} -free $\tau = 0.42$ ns). Fluorescence was excited at 450 nm with a diode laser and recorded through a 700/13 bandpass filter. The fluorescence QY of LDS798 in CHCl_3 was measured with an integrating sphere (Quantaury-QY Absolute PL quantum yield spectrometer, Hamamatsu) (QY = 0.16; 640 nm Ex).

As shown in **Figure 3.16A**, two-photon absorbance spectrum of NIR-GECO1 is similar to that of other iRFPs¹⁷⁵. That is, the cross-sectional value for the Soret band at <950 nm (50-75 GM) is substantially larger than for the Q band at ~1255 nm (<27 GM)

3.5.6 Animal care

For experiments performed at Massachusetts Institute of Technology (MIT), all methods for animal care and use were approved by the MIT Committee on Animal Care and were in accordance with the National Institutes of Health Guide for the Care and Use of Laboratory Animals. Four time pregnant Swiss Webster mice (Taconic) were used for this study, as were five C57BL/6 mice (Taconic), ages 4–12 weeks. Mice were used without regard to gender.

For experiments performed at Technical University of Munich, all animal *in vivo* experimentation was done in full compliance with the institutional guidelines of the Institute for Biological and Medical Imaging and with approval from the Government District of Upper Bavaria. A total of 12 mice were used for these experiments: 3 female FOXN1 nude mice that were injected with the NIR-GECO1

virus, 3 female FOXN1 nude mice that were injected with the miRFP virus, 3 female Black6 (C57BL/6J) transgenic mice expressing GCaMP6s, and 3 mice (2 female FOXN1 and 1 female Black6) that were injected with PBS as negative controls.

All experiments at University of Alberta for obtaining the cortical neurons were approved by the University of Alberta Animal Care and Use Committee and carried out in compliance with guidelines of the Canadian Council for Animal Care and the Society for Neuroscience's Policies on the Use of Animals and Humans in Neuroscience Research.

For experiments at HHMI Janelia Research Campus, all surgical and experimental procedures were in accordance with protocols approved by the HHMI Janelia Research Campus Institutional Animal Care and Use Committee and Institutional Biosafety Committee.

3.5.7 Imaging of NIR-GECO1 in HeLa cells and dissociated neuron cultures

HeLa cells (40–60% confluent) in 24-well glass-bottom plates (Cellvis) were transfected with 0.5 µg of the NIR-GECO1-pcDuEx2 plasmid and 2 µl of TurboFect (Thermo Fisher Scientific) in Dulbecco's modified Eagle's medium (DMEM; Gibco Fisher Scientific). Following 2 h of incubation, the media was changed to DMEM supplemented with 10% fetal bovine serum (FBS; Sigma-Aldrich), 2 mM GlutaMax (Thermo Fisher Scientific) and 1% penicillin–streptomycin (Gibco). The cells were then incubated for 48 h at 37 °C in a CO₂ incubator. Before imaging, culture medium was changed to Hanks' Balanced Salt Solution (HBSS).

For dissociated hippocampal mouse neuron culture preparation, postnatal day 0 or 1 Swiss Webster mice (Taconic Biosciences) were used as described in Ref. 37. Briefly, dissected hippocampal tissue was digested with 50 units of papain (Worthington Biochem) for 6–8 min at 37 °C, and the digestion was stopped by incubation with ovomucoid trypsin inhibitor (Worthington Biochem) for 4 min at 37 °C. Tissue was gently dissociated with Pasteur pipettes, and dissociated neurons were plated at a density of 20,000–30,000 per glass coverslip coated with Matrigel (BD Biosciences). Neurons were seeded in 100 µl of plating medium containing MEM (Life Technologies), glucose (33 mM; Sigma), transferrin (0.01%; Sigma), HEPES (10 mM; Sigma), Glutagro (2 mM; Corning), insulin (0.13%; Millipore), B27 supplement (2%; Gibco) and heat-inactivated FBS (7.5%; Corning). After cell adhesion, additional plating medium was added. AraC (0.002 mM; Sigma) was added when glia density was 50–70% of confluence. Neurons were grown at 37 °C and 5% CO₂ in a humidified atmosphere. We transduced cultured neurons at 4–5 days *in vitro* (DIV) by administering ~10¹⁰ viral particles of rAAV8-hSyn-iRFP682, rAAV8-hSyn-miRFP (both from Vector Core, University of North Carolina) or rAAV9-hSyn-NIR-GECO1 (Department of Biochemistry and Microbiology, University of Laval) per well (the rAAV genome titer was determined by dot blot). For coexpression of the GECIs, the rAAV8-hSyn-GCaMP6f, rAAV8-hSyn-RCaMP1.07 (both from Vector Core, University of North Carolina) and rAAV9-hSyn-NIR-GECO1 viral particles were added in a 1/1/3 ratio, respectively. A BV hydrochloride (Sigma-Aldrich) solution in dimethylsulfoxide (25 mM) was used as

a 1,000× stock (25 μM final concentration) for the experiments shown in **Figure 3.7** and **Figure 3.8A, B**. All measurements on neurons were taken after DIV 16.

For dissociated rat cortical neuron culture preparation, postnatal day 0 or 1 Sprague Dawley rats were used. Dissected cortices were digested in Papain solution (50 units; Sigma) for 10 min at 37 °C and then incubated with DNase (0.15 mg/ml; Sigma) for 5 min at 37 °C. After washing the tissue with FBS (Sigma) and removing supernatant, we added neurobasal B27 (Thermo Fisher Scientific) to tissue. Tissue was then gently dissociated with Pasteur pipettes, and dissociated neurons were plated at a density of $\sim 1.5 \times 10^5$ on collagen-coated 24-well glass-bottom dishes containing NbActiv4 culture medium (BrainBits LLC) supplemented with 2% FBS, penicillin-G potassium salt (50 units/ml), and streptomycin sulfate (50 mg/ml). Half of the culture media was replaced every 4–5 d. Neuronal cells were infected using the NIR-GECO1 lentivirus on day 8. Before imaging, the culture medium was changed to HBSS.

Wide-field fluorescence imaging of cultured neurons was performed using an epifluorescence inverted microscope (Eclipse Ti-E, Nikon) equipped with a Photometrics QuantEM 512SC camera and a 75-W Nikon xenon lamp or a Zyla5.5 sCMOS (scientific complementary metal-oxide semiconductor) camera (Andor) and a SPECTRA X light engine (Lumencor). NIS-Elements Advanced Research (Nikon) was used for automated microscope and camera control. Cells were imaged with 60×/1.49-NA (numerical aperture) oil or 20×/0.75-NA air objective lenses (Nikon) at room temperature. For dual-color imaging with GCaMP6s, NIR (650/60 nm Ex and 720/50 nm Em) and green (490/15 nm Ex and 525/50 nm Em)

filter sets were rotated into the emission light path. Three-color Ca²⁺ imaging with GCaMP6f and RCaMP1.07 was performed using an inverted Nikon Eclipse Ti microscope equipped with a spinning disk sCSUW1 confocal scanner unit (Yokogawa), 488, 561, and 642 nm solid state lasers, 525/25 nm, 579/34 nm and 664LP emission filters, a 20×/0.75-NA air objective lens (Nikon) and a 4.2 PLUS Zyla camera (Andor), controlled by NIS-Elements AR software. One cautionary note for confocal imaging is that gallium-arsenide-phosphide photomultiplier tube detectors have poor sensitivity at wavelengths greater than 700 nm.

Two-photon imaging (as shown in **Figure 3.16 B, C** and **Figure 3.17C**) was performed using an Olympus FVMPE-RS equipped with two lasers for fluorescence excitation. An InSight X3 laser (Spectra-Physics) tuned to 1,250 nm at 8.0% transmissivity was used to excite NIR-GECO1, and a Mai-Tai HP Ti:Sapphire laser (Spectra-Physics) tuned to 920 nm at 17.4% transmissivity was used to excite GCaMP6f. The laser beams were focused by a 25×/1.05-NA water-immersion objective lens (Olympus). NIR-GECO1 emission was separated using a 660–750 nm filter, GCaMP6f emission was separated using a 495–540 nm filter, and signals were collected onto separate photomultiplier tubes. Imaging was performed at a sampling speed of 2.0 μs per pixel with one-way galvano scanning. Raw scanner data were converted to an image z-stack using ImageJ (NIH).

Two-photon imaging for **Figure 3.17A, B, D–F** was performed using a two-photon laser scanning microscope (Ultima IV, Prairie Technologies) with a mode-locked Ti:Sapphire laser (Mai-Tai, Spectra-Physics) and a 16×/0.8-NA water-

immersion objective (CFI75 LWD 16; Nikon). For image acquisition, the laser was set to emit 880 nm at a total light power of 11.4 mW, and 535/50 nm and 731/137 nm emission filters (Semrock) were used. The microscope was operated using the ScanImage 3.8 software package¹⁹⁶.

3.5.8 Electrophysiology and Ca²⁺ imaging in dissociated hippocampal neurons

The genes encoding NIR-GECO1 and GCaMP6s were expressed under the control of a synapsin promoter in cultured rat hippocampal neurons. Neurons were stimulated using a custom-built field stimulator using a stimulus isolator (A385, World Precision Instruments) with platinum wires. Field stimuli (50 V, 83 Hz, 1 ms) were delivered in trains of 1, 2, 3, 5, 10, 20, 40, 80, 120 and 160 to the cultured neurons. Neurons were imaged using a Nikon Eclipse Ti2 inverted microscope equipped with a 40×/1.4-NA objective (Nikon). A quad bandpass filter (set number, 89,000; Chroma) was used along with a 480 nm light-emitting diode (LED) (Spectra X light engine, Lumencor) or a 640 nm LED (Spectra X light engine, Lumencor) to image GCaMP6s or NIR-GECO1, respectively. Fluorescence was collected using an sCMOS camera (Orca-Flash4.0, Hamamatsu) at 34 Hz. For GCaMP6s, the response amplitude ($\Delta F/F_{\min}$) was quantified as the change in fluorescence divided by baseline fluorescence over the 0.5-s period preceding the stimulus. For NIR-GECO1, the response amplitude was quantified as the change in fluorescence divided by peak fluorescence during the stimulus ($-\Delta F/F_{\min}$). SNR

was quantified as the peak change in fluorescence over the s.d. of the signal over the 0.5-s period preceding stimulation.

3.5.9 Multiplexed live-cell imaging with NIR-GECO1 in MIN6 β -cells

MIN6 pancreatic β -cells were cultured in DMEM containing 4.5 g l^{-1} glucose, supplemented with 10% (v/v) FBS, 1% (v/v) Pen-Strep and $50 \text{ }\mu\text{M}$ β -mercaptoethanol, and maintained at $37 \text{ }^\circ\text{C}$ with a 5% CO_2 atmosphere. Cells were plated onto 35-mm glass-bottom dishes, grown to 40–60% confluence and then transfected with $0.5 \text{ }\mu\text{g}$ each of plasmids encoding AKAR4, Pink Flamingo and NIR-GECO1 using Lipofectamine 2000 (Invitrogen). After 48 h, cells were washed twice with HBSS (Gibco) and imaged in HBSS at $37 \text{ }^\circ\text{C}$ using a Zeiss AxioObserver Z1 inverted epifluorescence microscope (Carl Zeiss) equipped with a $40\times/1.3\text{-NA}$ objective, a Lambda 10–2 filter-changer (Sutter Instruments) and a Photometrics Evolve 512 EMCCD (electron-multiplying charge-coupled device) (Photometrics) controlled by METAFLUOR v.7.7 software (Molecular Devices). Filters for cyan/yellow emission ratio were a 420DF20 excitation filter, a 450DRLP dichroic mirror and two emission filters (475DF40 for CFP and 535DF25 for YFP). Filters for RFP were a 555DF25 excitation filter, a ZT568RDC dichroic mirror and a 605DF52 emission filter. Filters for NIR-GECO1 were a 640DF30 excitation filter, a 700DF75 excitation filter and a T660LPXR dichroic mirror. Exposure times ranged between 50 and 500 ms, with EM gain set from 10–50, and images were acquired every 20 s. Fluorescence intensities were corrected by background

subtraction. The emission ratio change ($R - R_0$) or fluorescence intensity change ($F - F_0$) was divided by the initial ratio or intensity to obtain $\Delta R/R_0$ or $\Delta F/F_0$, with time zero defined as the time point immediately preceding drug addition. Graphs were plotted using GraphPad Prism 7 (GraphPad Software).

3.5.10 *In utero* electroporation

Embryonic day (E) 15.5 timed-pregnant female Swiss Webster (Taconic) mice were deeply anesthetized with 2% isoflurane. Uterine horns were exposed and periodically rinsed with warm sterile PBS. A plasmid encoding NIR-GECO1 or a mixture of plasmids encoding NIR-GECO1 and CoChR (pCAG-NIR-GECO1-WPRE, pCAG-CoChR-mTagBFP2-Kv2.2motif-WPRE; at a total DNA concentration of $\sim 1-2 \mu\text{g } \mu\text{l}^{-1}$) diluted with PBS were injected into the lateral ventricle of one cerebral hemisphere of an embryo. Five voltage pulses (50 V, 50-ms duration, 1 Hz) were delivered using round plate electrodes (ECM 830 electroporator, Harvard Apparatus). Injected embryos were placed back into the dam, and allowed to mature to delivery. The P0 pups were screened for corresponding fluorescence and negative pups were excluded for further experiments. All experimental manipulations were performed in accordance with protocols approved by the Massachusetts Institute of Technology Committee on Animal Care, following guidelines described in the US National Institutes of Health Guide for the Care and Use of Laboratory Animals.

3.5.11 Acute brain slice preparation

Acute brain slices were obtained from Swiss Webster (Taconic) mice at P11 to P22, using standard techniques. Mice were used without regard for sex. No statistical methods were used to estimate sample size for animal studies throughout. No randomization or blinding were used for animal studies throughout. Mice were anaesthetized by isoflurane inhalation, decapitated and cerebral hemispheres were quickly removed and placed in cold choline-based cutting solution consisting of (in mM): 110 choline chloride, 25 NaHCO₃, 2.5 KCl, 7 MgCl₂, 0.5 CaCl₂, 1.25 NaH₂PO₄, 25 glucose, 11.6 ascorbic acid and 3.1 pyruvic acid (339–341 mOsm per kg; pH 7.75 adjusted with NaOH) for 2 min, blocked and transferred into a slicing chamber containing ice-cold choline-based cutting solution. Coronal slices (300 µm thick) were cut with a Compressstome VF-300 slicing machine, transferred to a holding chamber with artificial cerebrospinal fluid (ACSF) containing (in mM) 125 NaCl, 2.5 KCl, 25 NaHCO₃, 2 CaCl₂, 1 MgCl₂, 1.25 NaH₂PO₄ and 11 glucose (300–310 mOsm/kg; pH 7.35 adjusted with NaOH) and recovered for 10 min at 34 °C followed by another 30 min at room temperature. Slices were subsequently maintained at room temperature until use. Both cutting solution and ACSF were constantly bubbled with 95% O₂ and 5% CO₂.

3.5.12 Concurrent electrophysiology and Ca²⁺ imaging in acute brain slice

Slices were transferred to a recording chamber on an Olympus BX51WI upright microscope and superfused (2–3 ml/min) with ACSF at room temperature.

Whole-cell patch-clamp recordings were acquired via an Axopatch 700B amplifier (Molecular Devices) and Digidata 1440 digitizer (Molecular Devices). For recordings, borosilicate glass pipettes (Warner Instruments) with an outer diameter of 1.2 mm and a wall thickness of 0.255 mm were pulled to a resistance of 3–5 M Ω with a P-97 Flaming/Brown micropipette puller (Sutter Instruments) and filled with a solution containing 155 mM K-gluconate, 8 mM NaCl, 0.1 mM CaCl₂, 0.6 mM MgCl₂, 10 mM HEPES, 4 mM Mg-ATP and 0.4 mM Na-GTP. The pipette solution pH was adjusted to 7.3 with KOH and the osmolarity was adjusted to 298 mOsm with sucrose. Cells were visualized through a 40 \times /0.8-NA water-immersion objective with epifluorescence. Whole-cell current-clamp recordings were obtained from NIR-GECO1-positive neurons in layer 2/3 of motor cortex. Fluorescence was excited by a SPECTRA X light engine (Lumencor) with 638/14 nm excitation filter (Semrock), fluorescence was collected through the same objective, passed through a 664 LP emission filter and imaged onto an Orca-Flash4.0 v.2 sCMOS camera (Hamamatsu) at 50-Hz acquisition frequency.

3.5.13 *In vivo* two-photon microscopy

AAV injection protocol

For two-photon *in vivo* imaging for **Figure 3.17F**, we expressed NIR-GECO1 in the mouse cortex via AAV and installed a chronic head plate with optical window above the corresponding brain area. Anesthesia was induced using isoflurane (induction, 3%; maintenance, 1-2%). We administered meloxicam (2 mg/kg i.p.)

and slow-release buprenorphine (1 mg/kg) as analgesics. After animals were placed in a stereotaxic frame (Kopf Instruments), sterile eye lubricant (Puralube, Fisher Scientific) was administered to prevent corneal drying, and a heating pad was used to maintain body temperature. The scalp was opened using a midline incision, and the region to be imaged (primary visual cortex) was identified using stereotaxic coordinates (2.5 mm anterior to bregma, 2.55 mm lateral from the midline). A small craniotomy was opened in the skull using a 0.5-mm burr (Fine Science Tools) and a high-speed hand dental drill. The AAV (AAV2/9-hSyn1-NIR-GECO1, 500 nL) was injected 200 μ m beneath the surface of the brain at a rate of 150 nL/min using a Nanofil syringe (World Precision Instruments) with a 33 G beveled needle (World Precision Instruments) and pump (World Precision Instruments). After the injection, the needle was kept in place for two minutes to allow time for diffusion of the virus prior to removing the needle from the brain. The scalp was closed using Vetbond.

Cranial window surgery

We allowed animals to recover from AAV injection surgeries before placing cranial windows. Anesthesia was induced using isoflurane (induction, 3%; maintenance, 1-2%). We administered meloxicam (2 mg/kg i.p.) and slow-release buprenorphine (1 mg/kg) as analgesics. After animals were placed in a stereotaxic frame (Kopf Instruments), sterile eye lubricant (Puralube, Fisher Scientific) was administered to prevent corneal drying, and a heating pad was used to maintain body temperature. Scalp fur was trimmed and a small circular section of skin (~1

cm in diameter) was excised using surgical scissors (Fine Science Tools). The periosteum was removed using fine forceps (Fine Science Tools). A custom-made circular head plate was attached to the skull using dental cement (C&B Metabond, Parkell Inc.) and centered around the region to be imaged. The head plate was then screwed into a custom-built fork fixed to a solid metal base. Under a continuous gentle flow of phosphate-buffered saline (137 mM NaCl, 27 mM KCl, 10mM phosphate buffer), a ~4-mm circular section of the skull, slightly larger than the window and centered over the injection site, was removed using a 0.5-mm burr (Fine Science Tools) and a high-speed hand dental drill, taking great care not to compress brain tissue or damage the underlying vasculature. Sterile sugi swabs (John Weiss & Son, Ltd) were used to absorb trace bleeding. A 3-mm glass coverslip (Warner Instruments) was gently placed over the brain. Veterinary adhesive (Vetbond, Fisher Scientific) was used to form a seal between the coverslip and the skull. A layer of Metabond was then applied for added durability. Meloxicam (2 mg/kg i.p.) was administered as an analgesic 24 hours after surgery, and as needed thereafter. After allowing two weeks for expression, we imaged NIR-GECO1 in anesthetized, head-fixed mice using the two-photon microscope described in **3.5.7**

3.5.14 *In vivo* meso-scale imaging

AAV injection protocol.

Four-week-old athymic female nude mice (Envigo, New Jersey, USA; stock number *Foxn1^{nu}069*) were injected with one of the following: 3 μ L of AAV2/9-hSYN1-NIR-GECO1 virus at a concentration of 10^{13} genome copies/mL (Neurophotonics Centre, Université Laval, Canada); 3 μ L of AAV2-hSyn1-miRFP virus at a concentration of 10^{12} genome copies/mL (UNC Vector core facility); or 3 μ L of Dulbecco's Phosphate Buffered Saline solution (PBS) (D8357, Sigma-Aldrich, Taufkirchen, Germany). For analgesia, mice were administered a single oral drop of a 125 mg/mL Metamizole solution (Novalgin[®], Sanofi-Aventis Deutschland GmbH, Frankfurt am Main, Germany) directly before and 4 hours after the injection. Anesthesia was induced via isoflurane (Isothesia[®], Henry Schein[®], NY, USA) at 3% v/v in 100% O₂. The mouse was placed into a custom head holder (SGM-4, Narishige International Limited, London, United Kingdom) connected to an anesthesia unit (Sigma Delta Vaporize, Penlon, UK). This head holder employs three points of fixation to hold the head in place: the incisors are placed into an opening in the metal holder, an anesthesia mask then covers the nose and an ear bar is placed into respective ears. Fixation in this way allows for easy access to the top of the head whilst allowing adjustment of head height, tilt and rotation. All of this is achieved without the need for implantation of external components on the skull of the mouse¹⁹⁷. Once correctly positioned, a small incision was made down the middle of the scalp using a scalpel. Both sides of the scalp were pulled aside to allow access to the skull. Hemostatic sponges (Gelfoam[®], Pfizer Pharmaceutical, NY, USA) were used to contain any bleeding during the procedure. A hole approximately 1 mm in diameter was carefully drilled into the skull, above the

primary somatosensory cortex hind limb region (S1HL), using a micro-drill (110-4103, CircuitMedic, MA, USA). This hole was used to inject virus into the brain. Injections were carried out via a glass capillary connected to a wireless nanoinjector (Neurostar, Tuebingen, Germany). To consistently inject into S1HL, the capillary was placed above bregma, defining this point as 0 for all axes. Then the capillary was moved using a joystick to the aforementioned drilled hole and lowered to the entry of the hole. The injection site was located at 0.02 mm anterior to bregma and 2 mm from the midline. From here the capillary was lowered 1.4 mm into the brain at a rate of 0.2 mm/s. Once at the required depth, the capillary was retracted 100 μ m to an injection depth of 1.3 mm. Injection of the virus was carried out at this location (S1HL region) at a rate of 2.5 nL/s. Five minutes after the injection was completed the capillary was retracted from the brain. The hole in the brain was sealed using adhesive luting cement (S380, Parkell Inc., NY, USA). The scalp was closed via suturing and tissue glue (Histoacryl[®], Braun, Germany). For all experiments, the physiologic status of the mice including heart rate, body temperature and blood oxygenation were constantly monitored using the PhysioSuite[®] physiological monitor (Kent Scientific, Torrington, CT, USA). A rectal thermometer and a feedback-controlled heating pad were used to ensure the body temperature of the mice were constant and at a physiological condition (PhysioSuite[®], Kent Scientific, Torrington, CT, USA). During surgical procedures anesthesia was maintained using isoflurane at a concentration of 1.0% to 1.5% v/v in 100% O₂ with a flow rate of approximately 0.7 L/min. After the surgery mice were closely monitored for signs of pain and when needed were treated with another

drop of Metamizole. All mice removed stitches themselves once the tissue glue had dissolved after 3 days.

Electrical Hindpaw Stimulation

Stainless steel needle electrodes were connected to the mouse paw by carefully inserting them under the skin of the foot pad. The electrodes were connected to a World Precision Instruments Stimulus Isolator (A365, World Precision Instruments, FL, USA). In all cases the applied voltage was set to 0.5 mA. The entire experiment was started via an external trigger that ensured the synchronization of the image acquisition and the paw stimulus. The outputs of the paw stimulus generator were connected to the electrodes in the paw of the mouse via a BNC cable. For single paw stimuli, a 50 ms electrical pulse was applied once every 25 s, at $t = 5$ s. For stimulation trains 10 pulses with a 20 ms on and 50 ms off duration were applied every 25 s, at $t = 5$ s. For both paradigms, this allowed the first 5 s of the cycle to be used for baseline activity determination. In both cases the stimulation paradigm was repeated every 25 seconds (1 cycle) for a total of 20 cycles. The fluorescence recording was synchronized with the paw stimulation via the initial trigger. Anesthesia levels were kept at 1-1.2% isoflurane v/v in 100% O₂ during paw stimulation experiments, head fixation and monitoring were the same as above.

Imaging

NIR-GECO1 transfected mice were imaged at 10 and 12 days post-injection, while miRFP and PBS injected mice were imaged 14 days post-injection. For virally induced fluorescence, the expression was consistent until ~21 days post injection at which point the fluorescence began to subside. This may be due to increased thickening of the skull and/or skin due to the aging of the mice. The same anesthesia method, head fixation and monitoring was used as outlined above for *in vivo* mesoscale AAV injections. Fluorescent illumination was achieved using a continuous wave 671 nm laser (FPYL-671-50T, Frankfurt Laser Company, Germany) coupled into a multimode fiber bundle (CeramOptec, Germany). The output at the distal end of the fiber was measured to be 41 mW (82% coupling efficiency) and was held in place at an angle of 45° at a distance of 8 cm from the head of the mouse. This setup ensured the entire head of the mouse was evenly illuminated. Fluorescence of NIR-GECO1 was detected by a sCMOS camera (LucaEM®, Andor Technology Ltd., UK) at a rate of 5 Hz. Light was collected through a macro lens (Micro-NIKKOR 105 mm, Nikon, Japan) and filtered using a 700 nm Long Pass (Andover, NH, USA) and 721/42 nm Band pass (Andover, NH, USA) held in place using a filter wheel (LTFW6, Thorlabs, NJ, USA). GCaMP6s mice (C57BL/6J-Tg(Thy1-GCaMP6s) GP4.12 Stock no. 025776, The Jackson Laboratory, ME, USA) were imaged at 90 and 93 days old in the exact same manner as above aside from laser and filter changes. Prior to imaging and where applicable, the fur above the scalp was removed by firstly shaving the area and then applying hair removal cream (Veet Sensitive Skin Hair Removal Cream, Reckitt Benckiser, Heidelberg, Germany). Application time was approximately 2

minutes per area and all remaining fur was carefully removed using cotton swabs and water. Both the skin and skull remained intact during imaging and were not damaged during the process. Fluorescence excitation was provided by a continuous wave laser at 473 nm (FPYL-473-50T, Frankfurt Laser Company, Germany) coupled into the same fiber with an output of 43 mW at the distal end. In this case a 525/39 nm band pass filter was used to collect emitted light (BrightLine Basic™ Fluorescence Filter, Semrock, NY, USA).

Data Analysis

All data sets were analyzed using custom code in Matlab (Matlab 2017b, Mathworks, MA, USA). The entire recording was imported into Matlab and concatenated into a single matrix. A cycle is defined as a 25 s-time period within which a stimulation of the paw occurs. For all stimulation paradigms of the 20 stimulation cycles the first was removed and the remaining 19 were averaged into a single cycle. Background subtraction was then carried out across the cycle from a 50×50-pixel region of interest (ROI) outside the fluorescent area. The images were smoothed using the *imfilter* function in Matlab with a kernel size of 25. Due to the photobleaching of the protein the entire cycle was detrended using linear detrending on a pixel by pixel basis. Next, $\Delta F/F_0$ values were determined by dividing the entire cycle by the baseline activity which was defined from a 50×50-pixel region of interest (ROI) from the first 5 seconds of the cycle. The cycle was multiplied by 100 to get the change values in %. The response of the protein across the averaged cycle was calculated from an averaged 50×50-pixel ROI within the

fluorescent area. A low pass filter was applied to all traces. For *in vivo* mesoscale activation figures, manual segmentation was applied to highlight the injected brain hemisphere.

3.5.15 Statistics and reproducibility

All data are expressed as mean \pm s.d. or mean \pm s.e.m., as specified in figure legends. Box plots with notches¹⁹⁸ are used for **Figures 3.7B, 3.8B, 3.13B, 3.17A** and **3.19C**. In these plots, the narrow part of the notch is the median; the top and bottom of the notch denote the 95% confidence interval of the median; the horizontal line is the mean; the top and bottom horizontal lines are the 25th and 75th percentiles for the data; and the whiskers extend 1.5 times the interquartile range from the 25th and 75th percentiles. Sample sizes (n) are listed with each experiment. No samples were excluded from analysis and all experiments were reproducible. No randomization or blinding was used. All attempts at replication of the experiments were successful.

Chapter 4: Improved genetically encoded near-infrared fluorescent calcium ion indicator for *in vivo* imaging

4.1 Abstract

Near-infrared (NIR) genetically-encoded calcium ion (Ca^{2+}) indicators (GECIs) have great advantages over GFP- and RFP-based GECIs in terms of multi-color imaging, reduced phototoxicity, less cross-talk with optogenetic actuators, and decreased scattering and absorption in mammalian tissues. However, the only NIR GECI currently available, NIR-GECO1, suffers from lower brightness and decreased dynamic range compared to the state-of-art GFP-based GCaMP series and RFP-based R-GECO and jRCaMP series when used for imaging of neural activity. Here, we report an improved NIR GECI evolved from NIR-GECO1. We characterized the performance of the new NIR GECI in cultured neurons, in acute mouse brain slices, and in *C. elegans in vivo*. The new NIR GECI, which is designated NIR-GECO2, enables more sensitive Ca^{2+} imaging in neurons compared to NIR-GECO1.

4.2 Introduction

BV-binding FPs are members of the broad family of fluorescent proteins (FPs) that have far-red (or NIR) excitation and emission (>650 nm). BV-binding FPs extend the spectra of FPs into the NIR region where tissue absorbance, scattering, and autofluorescence are substantially reduced relative to the visible wavelength

region. Many BV-FPs with different biophysical, biochemical, and spectral properties have been developed since 2009, and are now widely used as markers for multicolor fluorescence imaging (As discussed in **1.1.2**).

As with traditional β -barrel FPs, BV-FPs have been converted to indicators for visualizing cell dynamics, but the strategies for making BV-FP-based indicators has been generally limited to BIFC and FRET (as discussed in **1.1.3**). In chapter 3, we have described how a single BV-FP can be converted to an intensimetric indicator using the strategy of allosteric modulation of BV fluorescence¹⁹⁹. This is analogous to the most widely used strategy to generate single β -FP-based indicators. By inserting the Ca^{2+} -responsive domain CaM-RS20 into the protein loop between residues 170 and 177 of mIFP, we developed the first NIR Ca^{2+} indicator, NIR-GECO1. NIR-GECO1 provided robust inverse response to Ca^{2+} concentration changes in cultured cells, primary neurons, and acute slices²⁰⁰. However, as a first generation intensimetric NIR indicator, NIR-GECO1 suffers from insufficient brightness and sensitivity, which have hampered its widespread application for *in vivo* brain imaging. Following the example of how GCaMP was improved through multiple rounds of evolution and optimization, we felt it was highly likely that further optimization could greatly improve the performance of NIR-GECO1.

Directed evolution is a powerful technique for protein engineering. This technique was first employed in early to mid 1990s by Frances Arnold and coworkers to create enzymes with improved functions²⁰¹. At approximately the same time, directed evolution was also being applied to improving the performance

of β -barrel FPs⁶, helping to usher in a new era for fluorescence imaging. By combining random or site-directed mutation of a gene with human-defined selection of proteins encoded by the mutated genes, new proteins with improved function or new properties can be created. Although the mutation of genes is simple and similar for every directed evolution method, the selection part of directed evolution can be technically challenging. Library screening approaches can range from bacterial colony screening to mammalian cell screening, and can be performed largely through human-labor or with the assistance of robotic methods.

The development of GECIs has also greatly benefited from the use of directed evolution, particularly in recent years as screening technologies have continued to advance and improve. The state-of-the-art green fluorescent GECIs (*i.e.*, the GCaMP6 series) and red fluorescent GECIs (*i.e.*, jRGECO and jRCaMP series) were all generated with the assistance of a neuron-based screening platform²⁰², which is specifically designed for optimization indicators for *in vivo* imaging of neuronal activity in model organisms. In this modern era of protein engineering, the rationality and validity of the selection aspect of a directed evolution workflow generally determines how good the produced proteins will be for their desired application. In addition to GECIs, other successful examples include the engineering of the high quantum yield CFP mCerulean and the RFP mScarlet via lifetime-based bacterial colony screening^{203,204}. Yet another successful example was the optimization of NIR voltage indicators through robotic multidimensional mammalian screening³⁷. Based on the precedent of these examples, and many

others in the literature and in our own lab, we suspected that further improvement of NIR-GECO could be made by extensive directed evolution, provided we had a proper screening strategy.

To improve the performance of NIR-GECO1 for reporting neural activity, we performed directed evolution based on NIR-GECO1 using the screening strategy described in Chapter 3, which was demonstrated to be very effective for screening NIR-GECO variants. Following 3 additional rounds of selection a new variant, designated as NIR-GECO2, was identified. NIR-GECO2 enables more sensitive Ca^{2+} imaging of neural activity compared to its first-generation progenitor.

4.3 Results and discussion

4.3.1 Engineering and *in vitro* characterization of NIR-GECO2

In an effort to develop a brighter NIR GECI, we found that the mIFP (engineered from PAS and GAF domain of *Bradyrhizobium* bacteriophytochrome)³⁶ domain of NIR-GECO1 could be replaced with miRFP³⁷. miRFP is another monomeric BV-FP that was derived from *Rps. palustris* bacteriophytochrome and shares 57% amino acid homology with mIFP (**Figure 4.1, 4.2**). In principle, the miRFP³⁷ version on NIR-GECO1 could have served as a template for making improved NIR fluorescent Ca^{2+} indicators (**Figure 4.1, 4.2**) due to its higher brightness in mammalian cells over mIFP³⁷. However, we decided to start our further directed evolution efforts from NIR-GECO1 for two reasons. The first reason is that NIR-GECO1 was already optimized and worked well in brain slices, and so starting

from it might save time and lower risk. The second reason is that over-expression of the miRFP-based Ca^{2+} indicator appeared to be toxic to bacteria and it was challenging for us to incorporate the construct into the bacteria-HeLa screening system (as described in **Figure 3.2**) that we used for engineering NIR-GECO1.

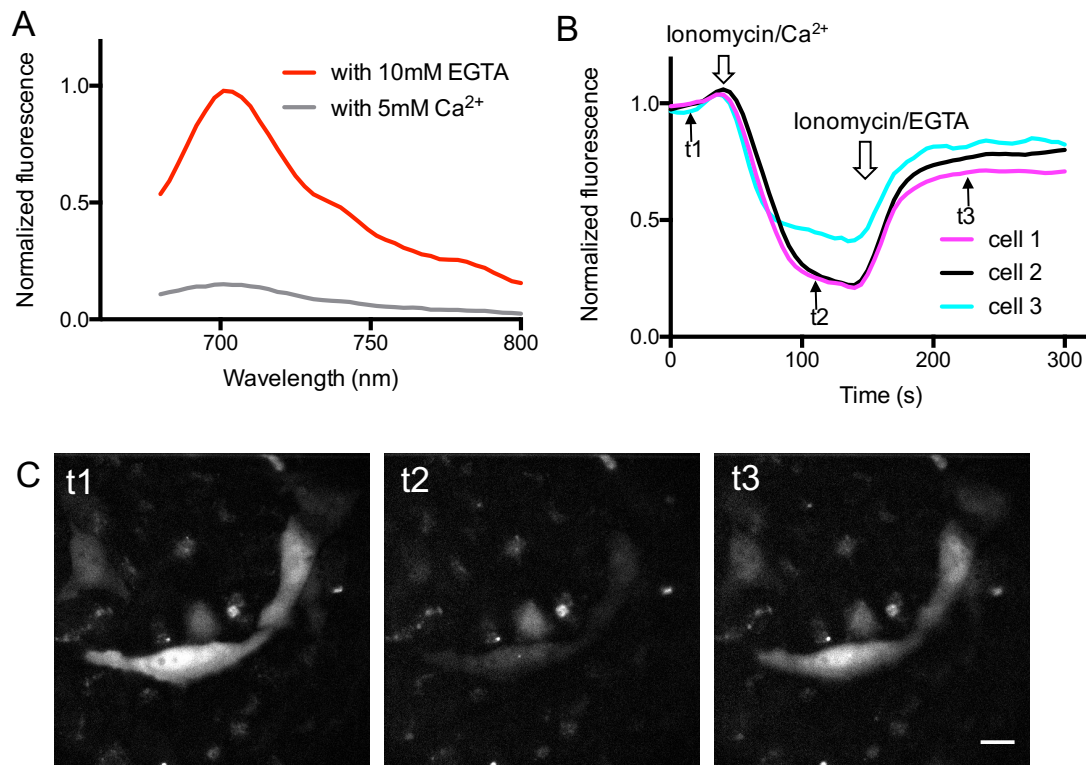


Figure 4.1 Ca^{2+} indicator prototype based on miRFP.

The mIFP domain of NIR-GECO1 was replaced with miRFP using the same insertion point and linker sequences (that is, CaM-RS20 was used to replace residues 170-177 of miFP or residues 172-179 of miRFP, **Figure 4.2**). **(A)** Fluorescence emission spectra of prototype of miRFP-based Ca^{2+} indicator in the presence (5 mM Ca^{2+}) and absence of Ca^{2+} (10 mM EGTA). **(B)** Intensity vs time traces for transfected HeLa cells. Cells were treated with ionomycin/ Ca^{2+} to

increase cellular Ca^{2+} concentrations and ionomycin/EGTA to deplete cellular Ca^{2+} . **(C)** Fluorescent images of miRFP-based Ca^{2+} indicator prototype at time points t1 to t3 (as denoted in **B**). Scale bar, 20 μm ; 650/60 nm excitation and 720/60 nm emission.

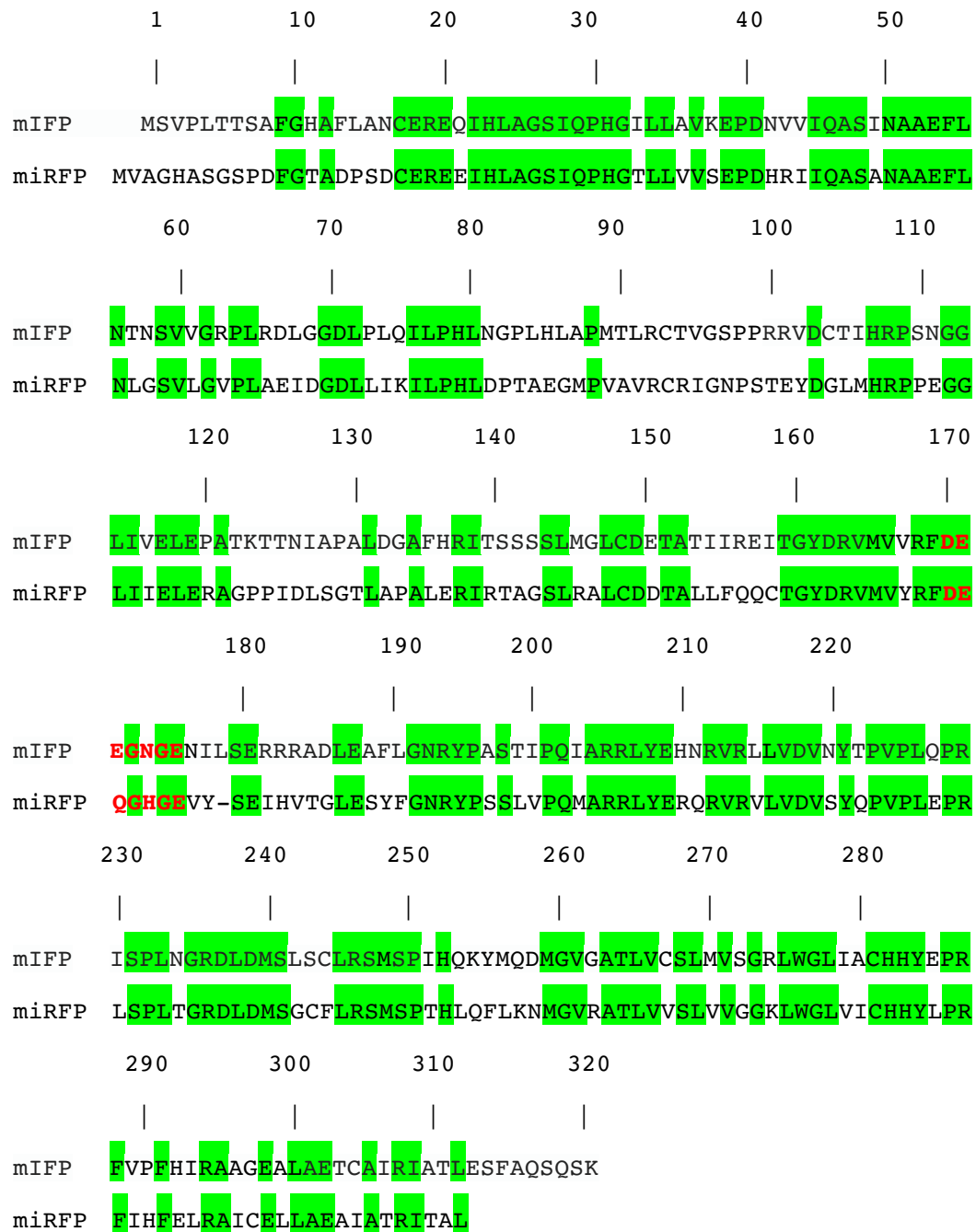


Figure 4.2. Alignment of amino acid sequences of mIFP and miRFP.

Alignment numbering is based on mIFP. The structurally analogous residues between mIFP and mIRFP are highlighted in green. Residues that were replaced by CaM-RS20 to make NIR-GECO1, and the prototype mIRFP-based Ca²⁺ indicator, respectively, are in bold and red.

Starting from the template of NIR-GECO1, three rounds of directed evolution were performed following the work-flow described in **Figure 3.2**. The top variant identified in the third round of screening, NIR-GECO2, possesses identical spectral properties with NIR-GECO1 and accumulated 6 mutations during the evolution process (**Figure 4.3**). The Ca²⁺-affinity of NIR-GECO2 is higher than that of NIR-GECO1 with a K_d of 102 nM (K_d of NIR-GECO1 is 215 nM) (**Figure 4.4A**), which is more suitable for reporting neural activity. To evaluate the brightness of NIR-GECO2, we expressed both NIR-GECO1 and NIR-GECO2 in HeLa cells and quantified the overall cellular brightness 24h after transfection. Under these conditions, NIR-GECO2 is approximately 50% brighter than NIR-GECO1 in HeLa cells (**Figure 4.4B**).

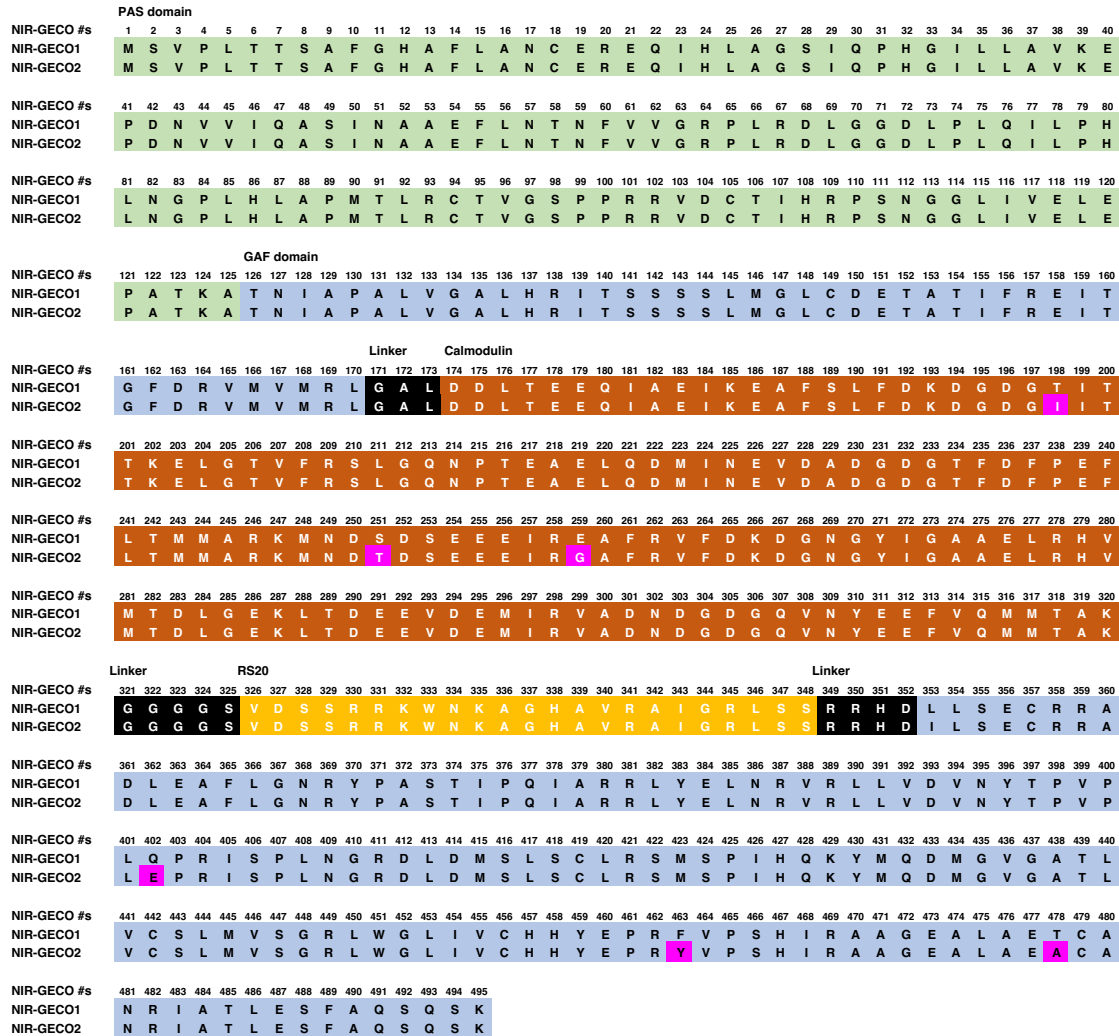


Figure 4.3 Sequence alignment of NIR-GECO2 and NIR-GECO1.

Single-amino-acid changes relative to NIR-GECO1 are highlighted with a magenta background. PAS domain, GAF domain, linkers, calmodulin, and RS20 are shown as light green, light blue, black, brown and yellow, respectively, consistent with domain colors in **Figure 3.1A, B and C**.

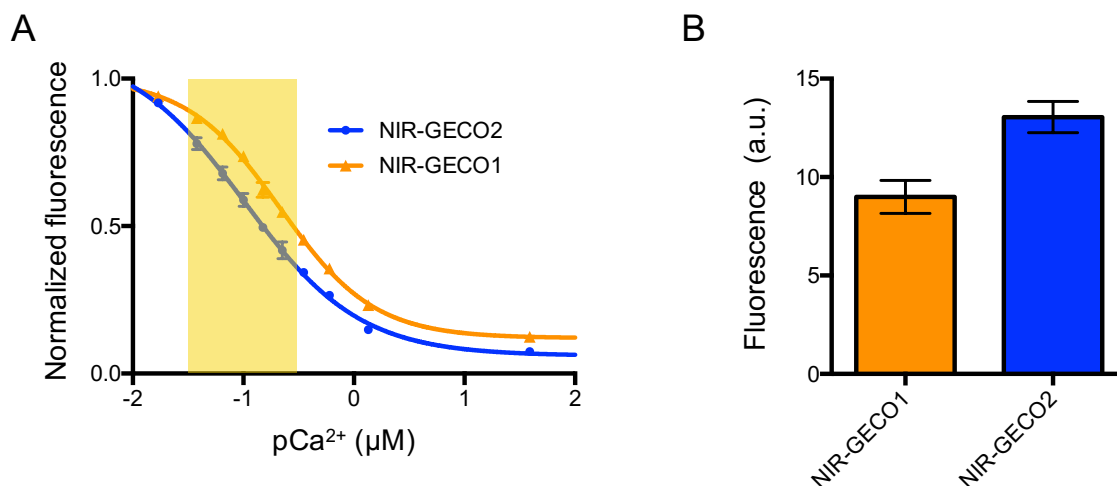


Figure 4.4 *In vitro* characterization of NIR-GECO2.

(A) Fluorescence of NIR-GECO1 and NIR-GECO2 as a function of Ca^{2+} concentration. Center values are the mean, and error bars are s.d. $n = 3$. Shaded area represents common cytosolic Ca^{2+} dynamic range of neurons. (B) Relative fluorescence intensity of NIR-GECO1 and NIR-GECO2 in HeLa cells ($n = 18$ cells from 3 cultures for NIR-GECO1; $n = 25$ from 3 cultures for NIR-GECO2). Fluorescence was normalized by co-expression of EGFP (NIR channel, 650/60 nm Ex and 720/60 nm Em; green channel, 490/15 nm Ex and 525/50 nm Em).

4.3.2 Characterization of NIR-GECO2 in cultured mouse hippocampal neurons and in acute mouse brain slices.

We next expressed NIR-GECO2 in dissociated hippocampal neurons via AAV virus transduction under the control of CAG promoter^{205,206}. 48h later, we observed bright fluorescence and large fluorescence fluctuations in response to spontaneous neural activity (**Figure 4.5**). To further evaluate the performance of NIR-GECO2, we induced expression of NIR-GECO2 along with CoChR¹¹⁴ in layer

2/3 (L2/3) of mouse motor cortex via *in utero* electroporation (IUE). We then prepared brain slices and activated neurons using 200 ms-pulse blue light from a light-emitting diode (LED) (470/34 nm). In transfected neurons, NIR-GECO2 reported light-evoked Ca^{2+} transients with 20% to 30% $-\Delta F/F_0$ for a single stimulation under 10 \times objective (**Figure 4.6B**). Under 20 \times objective, $-\Delta F/F_0$ went up to 40% to 50% with doubled light power (**Figure 4.6D**).

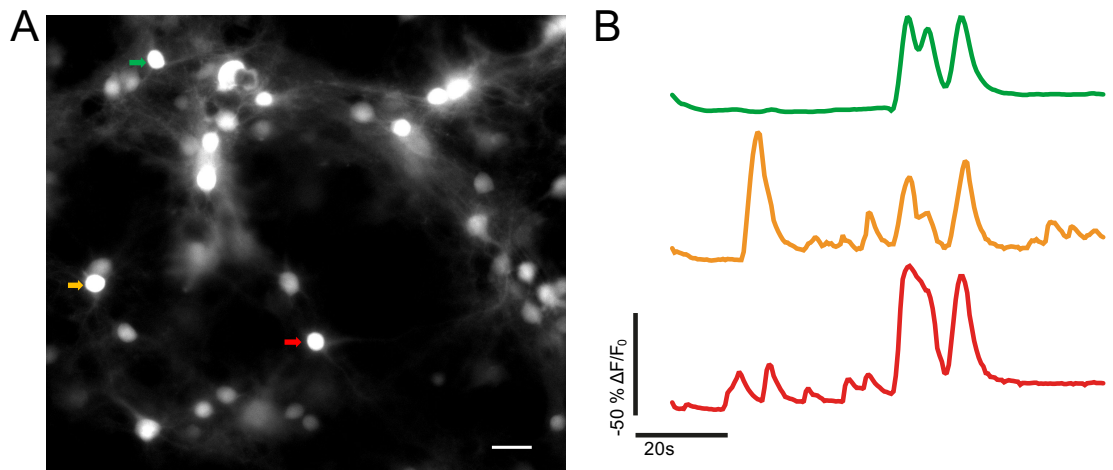


Figure 4.5. NIR-GECO2 in cultured mouse hippocampal neurons.

(A) Representative Image of cultured mouse hippocampal neurons expressing NIR-GECO2 (631/28 nm Ex and 664LP nm Em). Scale bar, 25 μm . (B) NIR-GECO2 fluorescence traces from 3 neurons, indicated with correspondingly colored arrows in A, in response to neural spontaneous activity.

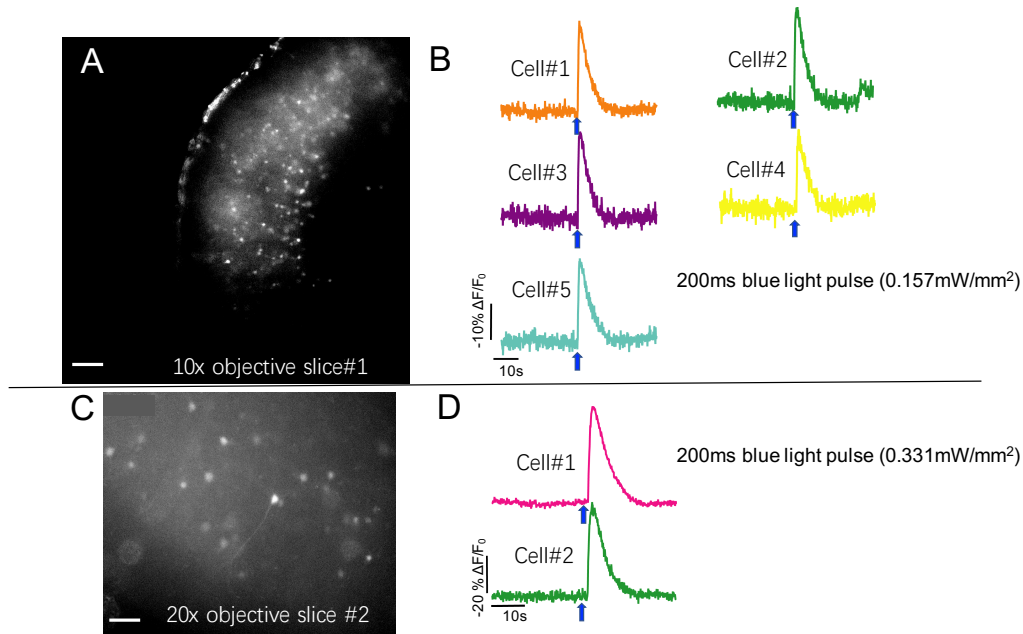


Figure 4.6. All-optical electrophysiology in acute mouse slice using NIR-GECO2 and CoChR.

(A) Wide-field image of a slice expressing the NIR-GECO2 gene introduced by IUE at E15.5. Image was captured using 10× objective (631/28 nm Ex and 664LP Em). Scale bar, 100 μm . (B) Representative fluorescence response of NIR-GECO2 to 200 ms blue-light (indicated by blue arrows, 470/34 nm, 0.175 mW/mm²). Representative traces are from 5 cells in A; acquisition rate 20 Hz. (C) Wide-field image of a slice expressing the NIR-GECO2 gene introduced by IUE at E15.5. Image was captured using 20× objective (631/28 nm Ex and 664LP Em). Scale bar, 50 μm . (D) Representative fluorescence response of NIR-GECO2 to 200ms blue-light (indicated by blue arrows, 470/34 nm, 0.331 mW/mm²). Representative traces are from 2 cells in C; acquisition rate 20 Hz.

4.3.3 Imaging neural activity in *C. elegans in vivo* using NIR-GECO2

We next tested NIR-GECO2 in *Caenorhabditis elegans*, a popular model organism in neuroscience. We chose to co-express NIR-GECO2 with hemoxygenase1³³ to increase the BV concentration in the neurons of the worm, which we expected would normally be lower than the concentration in mammalian cells. The gene of NIR-GECO2-T2A-HO1 was codon optimized for worms and was driven for expression by pan-neuronal-expression promoter *tag-168*. As a control, the gene of codon optimized NLS-jGCaMP7s²¹⁵ with same promoter was co-infected with NIR-GECO2-T2A-HO1 into worms. jGCaMP7s is the latest version of the GCaMP series of green fluorescent GECIs²¹⁵. In transgenic worms co-expressing NIR-GECO2 and NLS-GCaMP7s, we observed strong fluorescence and very low background noise in the NIR channel ($\lambda_{\text{ex}} = 637$ nm laser light, $\lambda_{\text{em}} = 664\text{LP}$) when imaged using a confocal microscope (**Figure 4.7A**). Although the expression of NLS-jGCaMP7s can also be easily seen from green channel ($\lambda_{\text{ex}} = 465$ nm laser light, emission at 527/50BP), we also observed strong autofluorescence from the intestinal area of worms (**Figure 4.7A**). Results from dual-color Ca^{2+} imaging revealed that both NIR-GECO2 and NLS-jGCaMP7 were able to report spontaneous neural activity with robust but opposite fluorescence responses (**Figure 4.7B**). During the imaging, we noticed that worms showed less undesired body-reaction (*i.e.*, motion) upon illumination of 640 nm laser compared to 465 nm laser, which made it easier to capture continuous images from NIR channel. Using only NIR-GECO2, we imaged a number of neurons and visualized their spontaneous neural activity (**Figure 4.7C**).

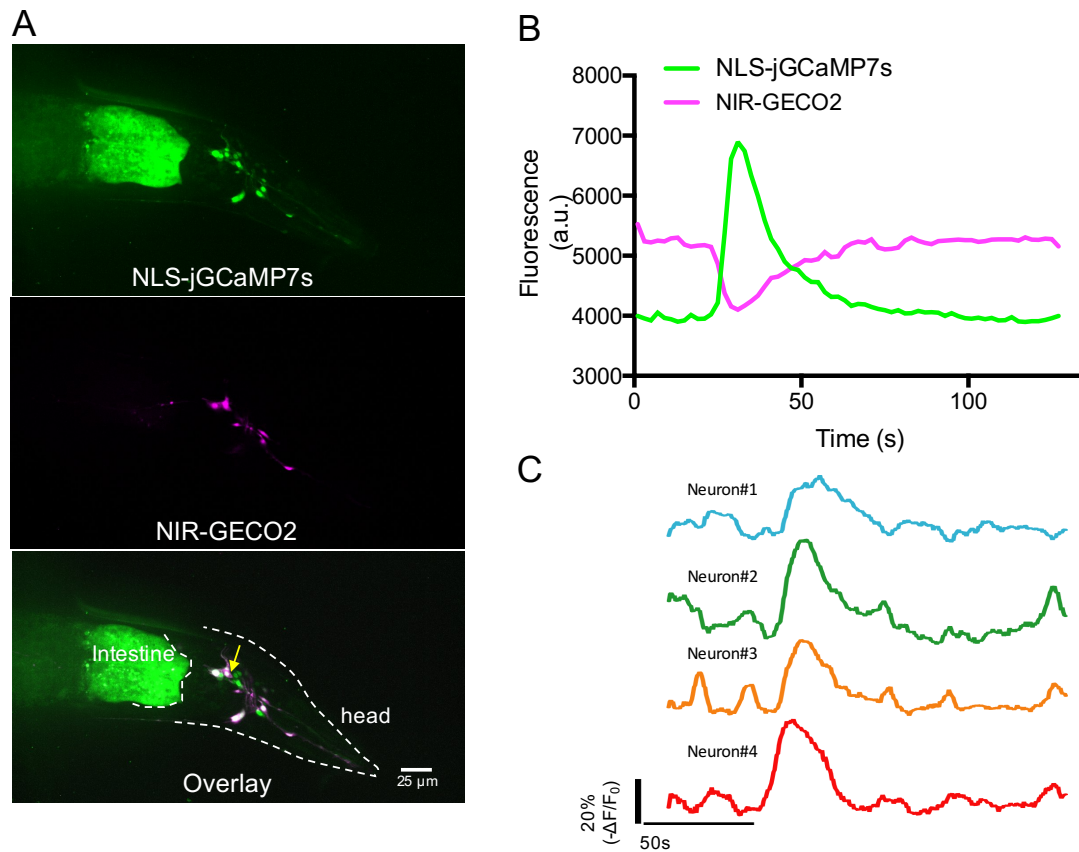


Figure 4.7. Imaging neural activity in the *C. elegans* using NIR-GECO2 and NLS-jGCaMP7s.

(A) Representative confocal images of worms co-expressing NIR-GECO2-T2A-HO1 and NLS-jGCaMP7s (representative of more than 3 worms). Top, fluorescent image of neurons expressing NLS-jGCaMP7s ($\lambda_{\text{ex}} = 465$ nm laser light, emission at 527/50BP). Middle, fluorescent image of neurons expressing NIR-GECO2-T2A-HO1 ($\lambda_{\text{ex}} = 637$ nm laser light, $\lambda_{\text{em}} = 664$ LP). Bottom, Overlay image of green channel and NIR channel. Scale bar, 25 μm . (B) Spontaneous Ca^{2+} fluctuation of a representative worm neuron (indicated in A by a yellow arrow) coexpressing NIR-

GECO2 and NLS-jGCaMP7s. Imaging conditions were identical to the experiments in **A**, acquisition rate 2 Hz. **(C)** Representative spontaneous Ca^{2+} oscillations of worm neurons reported by NIR-GECO2. Imaging conditions were identical to the experiments in **A**, acquisition rate 2 Hz.

4.3.4 Development of NIR-GECO variants with blue-shifted spectra

Both NIR-GECO1 and NIR-GECO2 have excitation and emission maxima at 678 and 704 nm, respectively. Accordingly, wavelengths in the range of 670-690 nm are optimal for excitation of NIR-GECO under one-photon illumination conditions. However, laser lines in this range are relatively uncommon in biological research labs. The most common red laser line is the 640-nm laser, which is ~40 nm blue-shifted from the excitation maximum of NIR-GECO1 and NIR-GECO2. Although both NIR-GECO1 and NIR-GECO2 could be effectively excited with 640 nm excitation, as we have demonstrated throughout Chapter 3 and 4, the mismatch between the optimal excitation of NIR-GECO and the available light source might hamper the wide usage of NIR-GECO, especially for *in vivo* imaging. To fill the gap between our indicator and the common imaging platform, we attempted to blue-shift the excitation spectrum of NIR-GECO2.

It has previously been demonstrated that mIFP, the template protein of NIR-GECO2, could be blue-shifted via the introduction of a single mutation I251C²⁰⁷. In mIFP (and NIR-GECO2), the incorporation of BV involves the formation of a thioether linkage between the cysteine at position 18 and the A-ring of BV (**Figure 4.8A**)²⁰⁷. In mIFP with the mutation I251C (iBlueberry), the introduced cysteine at

position 251 also covalently bonds to the A-ring by forming a second thioether group that also results in a decrease of the conjugation to the rest of the chromophore. This decreased conjugation results in a blue-shifted spectrum (**Figure 4.8B**)²⁰⁸. We suspected that, by introducing the same mutation to NIR-GECO2, the spectra of NIR-GECO2 would be similarly blue-shifted. We therefore introduced a single mutation I426C (corresponds to I251C in mIFP) into NIR-GECO2. As expected, the resulting variant was blue-shifted, with excitation and emission maxima at 645 nm and 673 nm, respectively (**Figure 4.8C**). Unfortunately, the introduction of the I426C mutation detrimentally affected the function of NIR-GECO2 and the dynamic range of NIR-GECO2 (I426C) dropped from 13-fold to 1.5-fold (**Figure 4.8C**). We reason that since there are two residues covalently bound to BV in NIR-GECO2 (I426C), the chromophore has become too rigid to be modulated by the interaction of CaM and RS20. To make the mutant more flexible, we introduced a second mutation, C18I, which would remove the thioether bond formed between C18 and ring A of BV but remain similar conjugation of the chromophore (**Figure 4.8D**)²⁰⁷. The resulting variant, NIR-GECO2 (C18I, I426C), has excitation and emission maxima at 646 nm and 672 nm, respectively and a Ca²⁺-dependent fold change of 4.5 (**Figure 4.8E**). However, the new mutant is dimmer than NIR-GECO2 and further directed evolution will be needed to rescue the fluorescence.

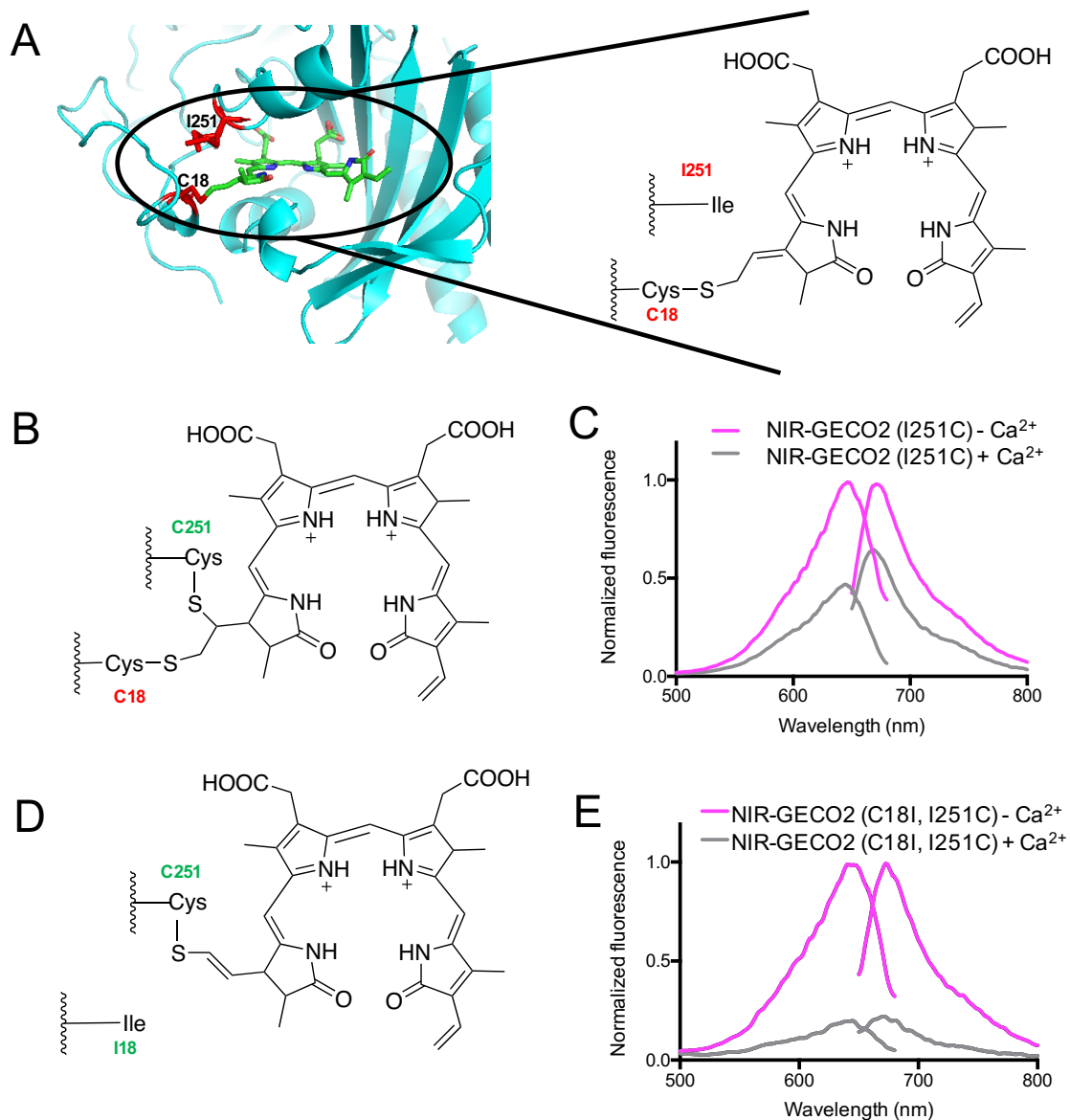


Figure 4.8. Rational design of blue-shifted NIR-GECO2.

(A) Covalent bonding between C18 of mIFP and its chromophore BV. Left, modeled structure of mIFP based on *DrBphP* (PDB:2O9B)²⁸, a close homolog of mIFP. C18 and I251 are labeled in red. These two residues are both in similar positions relative to the BV chromophore; right, schematic of chromophore structure in mIFP and NIR-GECO2. (B) Schematics of proposed chromophore structure in mIFP (I251C) and NIR-GECO2 (I426C). (C) Fluorescence excitation

and emission spectra of NIR-GECO2 (I426C) in the absence and presence of free Ca^{2+} (39 μM). (D) Proposed schematic of chromophore structure in mIFP (C18I, I251C) and NIR-GECO2 (C18I, I426C). (E) Fluorescence excitation and emission spectra of NIR-GECO2 (C18I, I426C) with the absence and presence of 39 μM free Ca^{2+} .

4.4 Conclusion

Based on NIR-GECO1, we evolved an improved NIR fluorescent Ca^{2+} indicator NIR-GECO2 with ~50% improvement in overall cellular brightness and more optimal Ca^{2+} affinity for reporting neural activity. We demonstrated that NIR-GECO2 enables more sensitive NIR Ca^{2+} imaging in cultured neurons and acute brain slices. We also expressed NIR-GECO2 in transgenic worms and observed NIR fluorescence oscillations in response to worms' spontaneous neural activity. NIR-GECO2 worked reliably in worms and will serve as an excellent tool for studying neural circuits, information integration and signal transduction in *C. elegans* and other model organisms.

NIR GECIs, however, still face challenges and there is substantial room for further optimization. First, NIR GECIs have smaller fluorescence changes ($\Delta F/F_0$) in neurons than the state-of-art green- and red-fluorescent GECIs. Second, NIR GECIs suffer from relatively low brightness and faster photobleaching, especially under two-photon illumination conditions. Third, NIR GECIs have slower on and off kinetics compared to the fastest green and red fluorescent GECIs. Due to those challenges, the future acceptance of NIR GECIs greatly relies on continued

directed evolution and effective high-throughput screening strategies to identify further improved variants. One of the possible direction is to engineer blue-shifted NIR-GECO variants, as blue-shifted BV-FPs tend to be brighter and are more compatible with currently available common light sources.

4.5 Materials and methods

4.5.1 General methods and materials

The general molecular biology methods used in this chapter were same to those described in section **3.5.1** except that the AAVs used in this chapter were produced at Janelia Research Campus (JRC) Virus core.

4.5.2 Construction of miRFP-based Ca²⁺ indicator prototype

The gene encoding miRFP was a gift from Edward Boyden (Addgene plasmid no. 108410). The insertion site of miRFP was determined by amino-acid-sequence alignment between miRFP and mIFP using Web BLAST. The DNA sequences encoding miRFP_{1 to 172}, CaM-RS20 (from NIR-GECO1), miRFP_{179 to 311} were amplified by PCR amplification separately and then severed as DNA templates for the assembly of miRFP_{1 to 172}-CaM-RS20-miRFP_{179 to 311} by overlap extension PCR. The generated DNA sequence was then inserted into pcDNA3.1 vector for mammalian expression and pBAD vector (same with the one used in section **3.5.2**) for bacterial expression.

4.5.3 Engineering of NIR-GECO2 and design of blue-shifted NIR-GECO2 variant

The pcDuEx2 vector (more details in section 3.5.3) was used to enable expression in both *E. coli* and mammalian cells. NIR-GECO1 served as the template for Library generation. Libraries were generated by error-prone PCR of the whole gene¹⁹¹.

In the evolution of NIR-GECO2, approximately 10,000 colonies were screened in a given round. For each round, the top 2% of colonies with high fluorescence intensity were picked, cultured and tested on 384-well plates. Approximately 25% of those picked variants were further screened in HeLa cells on the basis of fluorescence. In a given round, screening was stopped when a substantially improved variant was identified. There were 3 rounds of screening before NIR-GECO2 was identified.

To generate blue-shifted mutant based on NIR-GECO2, mutations I426C and C18I were introduced into NIR-GECO2 by using QuikChange Mutagenesis Kit (Agilent Technologies).

4.5.4 Protein purification and *in vitro* characterization

The genes for the mRFP-based Ca²⁺ indicator prototype, NIR-GECO1, and NIR-GECO2, with a poly-histidine tag on the C terminus, were expressed from

pBAD vector. Bacteria were lysed with a cell disruptor (Constant Systems Ltd) and then centrifuged at 15,000g for 30 min, and proteins were purified by Ni-NTA affinity chromatography (Agarose Bead Technologies). The buffer was typically exchanged to 10 mM MOPS, 100 mM KCl (pH 7.2) with centrifugal concentrators (GE Healthcare Life Sciences). The spectra of miRFP-based Ca^{2+} indicator prototype, with and without Ca^{2+} , were measured in a 384-well plate. Briefly, purified proteins were loaded into 384-well plates and then supplied with either 10 mM EGTA or 5mM CaCl_2 before measuring emission spectra. Ca^{2+} titrations of NIR-GECO1 and NIR-GECO2 were carried out using EGTA-buffered Ca^{2+} solutions (Calcium Calibration Buffer Kit no. 1, Life Technologies). We prepared buffers by mixing a CaEGTA buffer (30 mM MOPS, 100 mM KCl, 10 mM EGTA, 10 mM CaCl_2) and an EGTA buffer (30 mM MOPS, 100 mM KCl, 10 mM EGTA) to give free Ca^{2+} concentrations ranging from 0 nM to 39 μM at 25 °C. Fluorescence intensities were plotted against Ca^{2+} concentrations and fitted by a sigmoidal binding function to determine the Hill coefficient and K_d .

4.5.5 Imaging of miRFP-based Ca^{2+} indicator prototype in HeLa cells

HeLa cells were grown from their original frozen stocks without authentication or mycoplasma detection. HeLa cells (40-60% confluent) on 24-well glass bottom plate (Cellvis) were transfected with 0.5 μg of plasmid DNA and 2 μl TurboFect (Thermo Fisher Scientific). Following 2 h incubation, the media was changed to DEME (Gibco Fisher Scientific) with 10% FBS (SIGMA-ALDRICH), 2 mM

GlutaMax (Thermo Fisher Scientific) and 1% penicillin-streptomycin (Gibco) and the cells were incubated for 48h at 37 °C in a CO₂ incubator before imaging. Prior to imaging, culture medium was changed to HBSS. Wide-field imaging was performed on a Nikon Eclipse Ti microscope that was equipped with a 75 W Nikon xenon lamp, a 16-bit 512SC QuantEM EMCCD (Photometrics), and a 60× objective and was driven by a NIS-Elements AR 4.20 software package (Nikon). For time-lapse imaging, HeLa cells were treated with 4 mM EGTA (with 5 μM ionomycin) and then 10 mM CaCl₂ (with 5 μM ionomycin). Images were taken every 5 seconds. Filter set: 650/60 nm excitation and 720/60 nm emission.

4.5.6 Imaging of NIR-GECO2 in dissociated hippocampal neurons

The protocol for preparing dissociated hippocampal neurons was the same with the protocol described in section 3.5.7. We transduced cultured neurons at 5 days *in vitro* (DIV) by administering ~10¹⁰ viral particles of AAV2/8-CAG-NIR-GECO2 (Janelia Research Campus (JRC) Virus core). Wide-field fluorescence imaging of cultured neurons was performed using an epifluorescence inverted microscope (Eclipse Ti-E, Nikon) equipped with a Zyla5.5 sCMOS (scientific complementary metal-oxide semiconductor) camera (Andor) and a SPECTRA X light engine (Lumencor). NIS-Elements Advanced Research (Nikon) was used for automated microscope and camera control. Cells were imaged 1 week after transduction with a 20×/0.75-NA air objective lenses (Nikon) at room temperature.

Image were taken every 0.5 s. Filter set: 631/28 nm excitation and 664LP nm emission.

4.5.7 Imaging of NIR-GECO2 in acute brain slice

In utero electroporation were used for introducing expression of NIR-GECO2 and CoChR in the layer 2/3 (L2/3) of mouse motor cortex. The protocols for *in utero* electroporation and acute brain slice preparation were same to the protocols described in in section **3.5.10** and **3.5.11**, respectively. After preparation, slices were transferred to a recording chamber superfused (2-3 ml/min) with ACSF on an epifluorescence inverted microscope (Eclipse Ti-E, Nikon) equipped with a Zyla5.5 sCMOS (scientific complementary metal-oxide semiconductor) camera (Andor) and a SPECTRA X light engine (Lumencor). NIS-Elements Advanced Research (Nikon) was used for automated microscope and camera control. Blue light pulse from a 470/34 nm LED were combined with continuous illumination from a 631/28 nm LED to simultaneously stimulate and record Ca²⁺ transients in neurons co-expressing NIR-GECO2 and CoChR. Fluorescence of NIR-GECO2 was collected through a 664LP emission and imaged at 20-Hz acquisition frequency.

4.5.8 Ca²⁺ imaging in *C. elegans*

The genes of NIR-GECO2-T2A-HO1 and NLS-jGCaMP7s were codon-optimized for expression in *C. elegans* using the online resource at

<http://www.bioinformatics.org/>. Worms were maintained and grown following standard protocols. Transgenic worms expressing NIR-GECO2-T2A-HO1 and NLS-jGCaMP7s were generated by injecting the plasmids *tag-168::NIR-GECO2-T2A-HO1* and *tag-168::NLS-jGCaMP7s* into N2 background worms and picking those with strongest expression of NLS-jGCaMP7s. The transgenic worms (used without regard to sex) at L4 stage of development were put onto NGM plates with OP50 lawns no less than 16 h before experiments. Worms were mounted on 5% agarose pads on microscope slides, immobilized with 5 mM tetramisole and imaged using a Nikon Eclipse Ti inverted microscope equipped with a 40× NA 1.15 water immersion objective (Nikon), a 637-nm laser (637 LX, OBIS) focused on the back focal plane of the objective, and a 5.5 Zyla camera (Andor), controlled by NIS-Elements AR software. Fluorescence of NIR-GECO2 was imaged with 637 nm excitation at 800 mW/mm² and 664LP emission filter (Semrock); jGCaMP7s fluorescence was imaged with a 475-nm laser excitation filter and a 527/50BP emission filter (Semrock).

Chapter 5: Conclusion and future direction

5.1 Summary of the thesis

As a universal second messenger, Ca^{2+} is associated with many biological functions such as muscle contraction, neuronal transmission, gene regulation, and cell apoptosis²⁰⁹. Genetically encoded Ca^{2+} indicators (GECIs), therefore, are indispensable tools to monitor Ca^{2+} dynamic in a variety of biological process. In neuroscience, GECIs are widely used to measure neural activity and so there have been intensive efforts to date to improve GECI performance and the microscopy methods used to image them. The highly optimized GCaMP6 series enable monitoring of neural activity in large numbers of neurons *in vivo* using one-photon²¹⁰, two-photon²¹¹, or even three-photon²¹² microscopy. Optogenetic actuators (*i.e.*, channelrhodopsins) are another type of proteins that are widely used as tools in neuroscience. This class of proteins is mainly composed of light-gated ion channels or pumps that can be activated with light to stimulate or inhibit neural activity. Despite the fact that GCaMP6 (and the latest version jGCaMP7) outperformed all other GECIs, their spectral overlap with optogenetic actuators makes it challenging to image the GECI, without also activating the actuator, when combining those optogenetic tools for simultaneous controlling and recording of neural activity. To solve this problem, we have come up with two solutions made possible by protein-engineering (rather than microscopy advances): (1) development of a high-performance bioluminescent GECI and; (2) engineering of highly red-shifted GECIs.

In chapter 2, we report our efforts to develop a bioluminescent GECl, LUCI-GECO1, based on NanoLuc, one of the brightest luciferases, and ncpGCaMP6s, a topological variant of GCaMP6s. LUCI-GECO1 retains the optimal Ca^{2+} affinity of GCaMP6s and works well in HeLa cells and in neurons. We also demonstrated the experimental compatibility of LUCI-GECO1 and CheRiff, a blue-shifted channelrhodopsin. Due to the lack of excitation light, LUCI-GECO1 is a good match to CheRiff for simultaneously monitoring and activating neural activity.

In addition to using bioluminescent tools, developing red-shifted GEClS is another strategy to achieve zero-cross talk between optogenetic actuators and GEClS. Although RFP-based GEClS (*i.e.*, the R-GECO series and RCaMP series) have less spectral crosstalk with blue-light-activated optogenetic actuators than GFP-based GEClS do, their combined use with optogenetic actuators is hampered for two reasons. The first reason is that commonly used wavelengths (*e.g.*, ~560 nm) for excitation of red GEClS can still stimulate blue-light-activated channelrhodopsins^{187, 200} due to their very broad activation profiles. The second reason is that mApple-based GEClS (*i.e.*, jRGECO1a and RCaMP2) exhibit strong photoactivation upon illumination with blue-green light, and the combination of blue-green light-activated channelrhodopsins with those GEClS may lead to experimental imaging artefacts under some conditions¹⁶⁴. To address these shortcomings, in Chapter 3, we described our work on engineering a genetically-encoded NIR fluorescent Ca^{2+} indicator, NIR-GECO1, with excitation and emission maxima at 678 nm and 704 nm, respectively. We demonstrated that NIR-GECO1 was able to robustly report Ca^{2+} transients in cultured neurons, in acute brain slices,

and in mouse brain *in vivo* at mesoscale. Due to its highly red-shifted spectrum, we were able to achieve zero crosstalk for the combined use of NIR-GECO1 and CoChR, a high photo-current channelrhodopsin, in acute brain slices.

To further enhance the performance of NIR-GECO1, we performed 3 more rounds of directed evolution as described in Chapter 4. The resulting variant, NIR-GECO2, is 50% brighter than NIR-GECO1 in mammalian cells and exhibits higher Ca^{2+} affinity with a K_d of 102 nM ($K_d = 215$ nM for NIR-GECO1). We demonstrated the utility of NIR-GECO2 in cultured neurons, in acute brain slices, and in *C. elegans in vivo*. NIR-GECO2 enables more sensitive Ca^{2+} imaging than NIR-GECO1.

In summary, to reduce the crosstalk between GECIs and optogenetic actuators, we developed a bioluminescent GECI, LUCI-GECO1, that does not require excitation light. In addition we developed first and second generation NIR GECIs, NIR-GECO1 and NIR-GECO2, with excitation maximum at 678 nm. Those GECIs are fully compatible with optogenetic actuators. In the following section of this concluding chapter, I provide my own perspectives for these two types of GECIs and some possible future research directions.

5.2 LUCI-GECO: general perspective and future directions

LUCI-GECO1 is a Nanoluc-based ratiometric bioluminescent Ca^{2+} indicator that emits blue-green light in the presence of its substrate furimazine. Compared to other NanoLuc-based intensimetric Ca^{2+} indicators (*i.e.*, GeNL(Ca^{2+})⁸⁶), LUCI-GECO1 has two major advantages. First, LUCI-GECO1 is brighter in the resting-

state (*i.e.*, low Ca^{2+} concentration) due to the higher photon-production efficiency of an intact luciferase. The luciferase of intensimetric Ca^{2+} indicators, however, is split and produces a more limited number of photons in the resting-state. Second, bioluminescent imaging of LUCI-GECO1 could potentially reduce artifacts caused by changes of substrate concentration and motion of specimen because of normalization of signals from two channels (blue and green). On the other hand, LUCI-GECO1 and other ratiometric indicators require more complicated optical devices than their intensimetric counterparts, which might limit their utility for combination with other optical probes. Compared to another ratiometric bioluminescent GECI, CalfluxVTN¹⁰³, LUCI-GECO1 showed somewhat lower dynamic range but higher affinity to Ca^{2+} , suggesting that LUCI-GECO1 is more suited for use in neurons where Ca^{2+} concentration changes are relatively small (from ~100 nM to few hundred nM in most of cases).

In addition to combined use with optogenetic tools, another potential use of bioluminescent GECIs is to report Ca^{2+} dynamics from deep-tissue of small mammal model organisms (*i.e.*, mice) *in vivo*. However, *in vivo* use of all currently available bioluminescent GECIs is limited by two major issues. The first issue is that the substrate, furimazine (or coelenterazine) for LUCI-GECO1 and many other bioluminescent tools has poor biodistribution and is unable to cross the brain-blood barrier, which makes brain imaging challenging. The second issue is the intrinsic dimness of bioluminescence compare to fluorescence. The dim signals from bioluminescence require non-ideal camera settings like long exposure times and pixel binning, which could cause two problems for *in vivo* imaging. The first

problem is slow imaging rates (~seconds level) and the second problem is poor resolution (~mm level). Ideally, single-cell resolution and millisecond-imaging rate is preferable for imaging of brain area to understand brain function²¹³. Some of these issues may be addressed with further hardware improvements (*e.g.*, improved camera sensitivity). On the molecular side, future directions could focus on discovery or engineering of new luciferase-luciferin pairs that could provide better sensitivity due to higher quantum yield, higher catalytic efficiency, and more red-shifted emission. Once revolutionary luciferase-luciferins emerge, more efforts could be put on the engineering of new bioluminescent GECI using strategies similar to those used to make LUCI-GECO1, CalfluxVTN¹⁰³ and GeNL (Ca²⁺)⁸⁶.

5.3 NIR-GECO: general perspective and future directions

In Chapter 3 and 4, we reported NIR-GECO1 and NIR-GECO2, respectively. NIR-GECO1 is the first example of a NIR GECI based on a monomeric BV-FP such as mIFP³⁶. Although BV-FPs are structurally distinct from β -barrel FPs, we have demonstrated that, through the use of protein engineering and directed evolution, BV-FPs can also serve as templates for making single FP-based indicators. NIR-GECO1 exhibits robust inverse Ca²⁺ responses in cultured neurons and acute brain slices. Multiplexed imaging of NIR-GECO1 with other genetically-encoded indicators or optogenetic actuators provides excellent opportunities for measuring multiple distinct cellular activities or performing all-optical electrophysiology (simultaneous optical observation and perturbation of neural

activity), respectively. As a second generation NIR GECl, NIR-GECO2 works very well in *C. elegans in vivo* and is potentially a robust tool to study molecular mechanisms of worm behaviors along with optogenetic actuators.

Multiplexed imaging with other genetically-encoded tools, however, is not the end of the story for the NIR-GECO series. One more intriguing use of NIR-GECO2 (or further improved versions) is to visualize neural activity deep within the brains of rodents and other small animals. NIR wavelengths of light experience minimal absorbance and scattering by tissue, enabling them to be used for deeper tissue imaging in conjunction with NIR-GECO variants. As each layer of the mouse cortex is several hundreds of μm thick²¹⁴, even modest improvements in imaging depth can provide new opportunities for interrogating the brain. However, even using latest version of NIR-GECO variants, we still haven't succeeded in obtaining functional imaging in rodents *in vivo* at single-cell resolution, thus further optimization is needed

Unlike GFP-type FPs and their derivative indicators, in which the chromophore is autogenerated, NIR-GECOs (and other BV-FPs) need to incorporate endogenous BV as their chromophores. Thus, the brightness of this type of FP largely depends on the cellular concentration of BV. Considering the low BV concentration of neurons and the challenging *in vivo* delivery of BV, future efforts could be invested in either developing a better way to deliver BV, or improving the BV incorporation efficiency of NIR-GECO. One possible way to enhancing *in vivo* delivery of BV is to supplement with BV dimethylester (BVMe₂). BVMe₂ is a more hydrophobic molecule and has greater cell permeability³⁵. To improve the overall

fluorescence (resulting from a combination of intrinsic fluorescent brightness and BV incorporation efficiency) of NIR-GECO2 in mammalian cells, a new and effective screening approach is in demand. Potentially, we could adapt the mammalian cell-based screening approach reported by Piatkevich *et. al.*³⁷.

In addition to improving the performance of NIR-GECO, another direction could be the development of other NIR indicators by swapping the Ca²⁺-sensing of NIR-GECO to voltage-sensing domain, neurotransmitter-sensing domains, kinase activity-sensing domains, or others, just as has been done with GCaMP series and R-GECO series⁵⁴. Overall, we expect NIR-GECO to be the first in a long line of NIR indicators that will create new opportunities for biological imaging and ultimately lead to new advances and treatments for human diseases.

References

1. Johnson FH, Shimomura O, Saiga Y, Gershman LC, Reynolds GT, Waters JR. Quantum efficiency of cypridina luminescence, with a note on that of aequorea. *J. Cell Comp. Physiol.* 1962; 60(1): 85-103.
2. Shimomura O, Johnson FH, Saiga Y. Extraction, purification and properties of aequorin, a bioluminescent protein from the luminous hydromedusan, aequorea. *J. Cell Comp. Physiol.* 1962; 59(3): 223-239.
3. Prasher DC, Eckenrode VK, Ward WW, Prendergast FG, Cormier MJ. Primary structure of the aequorea victoria green-fluorescent protein. *Gene.* 1992; 111(2): 229-233.
4. Yang TT, Cheng L, Kain SR. Optimized codon usage and chromophore mutations provide enhanced sensitivity with the green fluorescent protein. *Nucleic Acids Res.* 1996; 24(22): 4592-4593.
5. Heim R, Tsien RY. Engineering green fluorescent protein for improved brightness, longer wavelengths and fluorescence resonance energy transfer. *Curr. Biol.* 1996; 6(2): 178-182.
6. Heim R, Cubitt AB, Tsien RY. Improved green fluorescence. *Nature.* 1995; 373(6516): 663-664.
7. Matz MV, Fradkov AF, Labas YA, et al. Fluorescent proteins from nonbioluminescent anthozoa species. *Nat. Biotechnol.* 1999; 17(10): 969-973.
8. Campbell RE, Tour O, Palmer AE, et al. A monomeric red fluorescent protein. *Proc. Natl. Acad. Sci. U.S.A.* 2002; 99(12): 7877-7882

9. Shaner NC, Lin MZ, McKeown MR, et al. Improving the photostability of bright monomeric orange and red fluorescent proteins. *Nat. Methods.* 2008; 5(6): 545-551.
10. Wang L, Jackson WC, Steinbach PA, Tsien RY. Evolution of new nonantibody proteins via iterative somatic hypermutation. *Proc. Natl. Acad. Sci. U.S.A.* 2004; 101(48): 16745-16749.
11. Shaner NC, Campbell RE, Steinbach PA, Giepmans BNG, Palmer AE, Tsien RY. Improved monomeric red, orange and yellow fluorescent proteins derived from *discosoma* sp. red fluorescent protein. *Nat. Biotechnol.* 2004; 22(12): 1567-72.
12. Wiedenmann J, Schenk A, Röcker C, Girod A, Spindler K, Nienhaus GU. A far-red fluorescent protein with fast maturation and reduced oligomerization tendency from *entacmaea quadricolor* (anthozoa, actinaria). *Proc. Natl. Acad. Sci. U.S.A.* 2002; 99(18): 11646-11651.
13. Merzlyak EM, Goedhart J, Shcherbo D, et al. Bright monomeric red fluorescent protein with an extended fluorescence lifetime. *Nat. Methods.* 2007; 4(7): 555-557.
14. Kredel S, Oswald F, Nienhaus K, et al. mRuby, a bright monomeric red fluorescent protein for labeling of subcellular structures. *PLoS One.* 2009; 4(2): e4391.
15. Subach OM, Gundorov IS, Yoshimura M, et al. Conversion of red fluorescent protein into a bright blue probe. *Chem. Biol.* 2008; 15(10): 1116-1124.
16. Solovieva EA, Bogdanova EA, Lukyanov S, et al. Bright far-red fluorescent protein for whole-body imaging. *Nat. Methods.* 2007; 4(9): 741-746.

17. Chu J, Haynes RD, Corbel SY, et al. Non-invasive intravital imaging of cellular differentiation with a bright red-excitable fluorescent protein. *Nat. Methods.* 2014; 11(5): 572-578.
18. Tomosugi W, Tani T, Kotera I, et al. An ultramarine fluorescent protein with increased photostability and pH insensitivity. *Nat. Methods.* 2009; 6(5): 351-353.
19. Li ZY, Zhang ZP, Bi LJ, et al. Mutagenesis of mNeptune red-shifts emission spectrum to 681-685 nm. *PloS One.* 2016; 11(4): e0148749.
20. Kobayashi H, Ogawa M, Alford R, Choyke PL, Urano Y. New strategies for fluorescent probe design in medical diagnostic imaging. *Chem. Rev.* 2010; 110(5): 2620-2640.
21. Shcherbakova DM, Shemetov AA, Kaberniuk AA, Verkhusha VV. Natural photoreceptors as a source of fluorescent proteins, biosensors, and optogenetic tools. *Annu. Rev. Biochem.* 2015; 84(1): 519-550.
22. Ntziachristos V. Going deeper than microscopy: The optical imaging frontier in biology. *Nat. Methods.* 2010; 7(8): 603-614.
23. Anders K, Essen L. The family of phytochrome-like photoreceptors: Diverse, complex and multi-colored, but very useful. *Curr. Opin. Structl. Biol.* 2015; 35: 7-16.
24. Sineshchekov VA. Photobiophysics and photobiochemistry of the heterogeneous phytochrome system. *Biochim. Biophys. Acta. Bioenerg.* 1995; 1228(2): 125-164.

25. Giraud E, Zappa S, Vuillet L, et al. A new type of bacteriophytochrome acts in tandem with a classical bacteriophytochrome to control the antennae synthesis in *rhodospseudomonas palustris*. *J. Biol. Chem.* 2005; 280: 32389-32397.
26. Rockwell NC, Lagarias JC. A brief history of phytochromes. *Chemphyschem* 2010; 11(6): 1172-1180.
27. Yang X, Kuk J, Moffat K. Crystal structure of *pseudomonas aeruginosa* bacteriophytochrome: Photoconversion and signal transduction. *Proc. Natl. Acad. Sci. U.S.A.* 2008;105(38): 14715-14720.
28. Wagner JR, Zhang J, Brunzelle JS, Vierstra RD, Forest KT. High resolution structure of *deinococcus* bacteriophytochrome yields new insights into phytochrome architecture and evolution. *J. Biol. Chem.* 2007; 282(16): 12298-12309.
29. Anders K, Essen L. The family of phytochrome-like photoreceptors: Diverse, complex and multi-colored, but very useful. *Curr. Opin. Structl. Biol.* 2015; 35: 7-16.
30. Shu X, Royant A, Lin MZ, et al. Mammalian expression of infrared fluorescent proteins engineered from a bacterial phytochrome. *Science.* 2009; 324(5928): 804-807.
31. Filonov GS, Piatkevich KD, Ting L, Zhang J, Kim K, Verkhusha VV. Bright and stable near-infrared fluorescent protein for in vivo imaging. *Nat. Biotechnol.* 2011; 29(8): 757-761.

32. Auldridge ME, Satyshur KA, Anstrom DM, Forest KT. Structure-guided engineering enhances a phytochrome-based infrared fluorescent protein. *J. Biol. Chem.* 2012; 287(10): 7000-7009.
33. Dan Y, William CG, Chun H, et al. An improved monomeric infrared fluorescent protein for neuronal and tumour brain imaging. *Nat. Commun.* 2014; 5(1): 3626.
34. Shcherbakova DM, Verkhusha VV. Near-infrared fluorescent proteins for multicolor in vivo imaging. *Nat. Methods.* 2013; 10(8): 751-754.
35. Rodriguez EA, Tran GN, Gross LA, et al. A far-red fluorescent protein evolved from a cyanobacterial phycobiliprotein. *Nat. Methods.* 2016; 13(9): 763-769.
36. Dan Y, Baird MA, Allen JR, et al. A naturally monomeric infrared fluorescent protein for protein labeling in vivo. *Nat. Methods.* 2015; 12(8): 763-765.
37. Piatkevich KD, Jung EE, Straub C, et al. A robotic multidimensional directed evolution approach applied to fluorescent voltage reporters. *Nat. Chem. Biol.* 2018; 14(4): 352-360.
38. Shcherbakova DM, Baloban M, Emelyanov AV, Brenowitz M, Guo P, Verkhusha VV. Bright monomeric near-infrared fluorescent proteins as tags and biosensors for multiscale imaging. *Nat. Commun.* 2016; 7: 12405.
39. Oliinyk OS, Shemetov AA, Pletnev S, Shcherbakova DM, Verkhusha VV. Smallest near-infrared fluorescent protein evolved from cyanobacteriochrome as versatile tag for spectral multiplexing. *Nat. Commun.* 2019; 10(1): 279.
40. Piatkevich KD, Suk H, Kodandaramaiah SB, et al. Near-infrared fluorescent proteins engineered from bacterial phytochromes in neuroimaging. *Biophys. J.* 2017; 113(10): 2299-2309.

41. Drepper T, Egger T, Circolone F, Heck A, Krauß U, et al. Reporter proteins for in vivo fluorescence without oxygen. *Nat. Biotechnol.* 2007; 25(4): 443-445.
42. Kumagai A, Ando R, Miyatake H, et al. A bilirubin-inducible fluorescent protein from eel muscle. *Cell.* 2013; 153(7): 1602-1611.
43. Chapman S, Faulkner C, Kaiserli E, et al. The photoreversible fluorescent protein iLOV outperforms GFP as a reporter of plant virus infection. *Proc. Natl. Acad. Sci. U.S.A.* 2008; 105(50): 20038-20043.
44. Miesenböck G, De Angelis DA, Rothman JE. Visualizing secretion and synaptic transmission with pH-sensitive green fluorescent proteins. *Nature.* 1998; 394(6689): 192-195.
45. Tang S, Wong H, Wang Z, et al. Design and application of a class of sensors to monitor Ca²⁺ dynamics in high Ca²⁺ concentration cellular compartments. *Proc. Natl. Acad. Sci. U.S.A.* 2011; 108(39): 16265-16270.
46. Jayaraman S, Haggie P, Wachter RM, Remington SJ, Verkman AS. Mechanism and cellular applications of a green fluorescent protein-based halide sensor. *J. Biol. Chem.* 2000; 275(9): 6047-6050.
47. Galiotta LJ, Haggie PM, Verkman AS. Green fluorescent protein-based halide indicators with improved chloride and iodide affinities. *FEBS. Lett.* 2001; 499(3): 220-224.
48. Kuner T, Augustine GJ. A genetically encoded ratiometric indicator for chloride. *Neuron.* 2000; 27(3): 447-459.

49. Østergaard H, Henriksen A, Hansen FG, Winther JR. Shedding light on disulfide bond formation: Engineering a redox switch in green fluorescent protein. *EMBO J.* 2001; 20(21): 5853-5862.
50. Hanson GT, Aggeler R, Oglesbee D, et al. Investigating mitochondrial redox potential with redox-sensitive green fluorescent protein indicators. *J. Biol. Chem.* 2004; 279(13): 13044-13053.
51. Nakai J, Imoto K, Ohkura M. A high signal-to-noise Ca²⁺ probe composed of a single green fluorescent protein. *Nat. Biotechnol.* 2001; 19(2): 137-141.
52. Tian L, Hires SA, Mao T, et al. Imaging neural activity in worms, flies and mice with improved GCaMP calcium indicators. *Nat. Methods.* 2009; 6(12): 875-881.
53. Chen TW, Wardil TJI, Sun Y, et al. Ultrasensitive fluorescent proteins for imaging neuronal activity. *Nature.* 2013; 499(7458): 295-300.
54. Greenwald EC, Mehta S, Zhang J. Genetically encoded fluorescent biosensors illuminate the spatiotemporal regulation of signaling networks. *Chem. Rev.* 2018; 118(24): 11707-11794.
55. Ghosh I, Hamilton AD, Regan L. Antiparallel leucine zipper-directed protein reassembly: Application to the green fluorescent protein. *J. Am. Chem. Soc.* 2000; 122(23): 5658-5659.
56. Kojima T, Karasawa S, Miyawaki A, Tsumuraya T, Fujii I. Novel screening system for protein-protein interactions by bimolecular fluorescence complementation in *saccharomyces cerevisiae*. *J. Biosci. Bioeng.* 2011; 111(4): 397-401.

57. Ding Z, Liang J, Lu Y, et al. A retrovirus-based protein complementation assay screen reveals functional AKT1-binding partners. *Proc. Natl. Acad. Sci. U.S.A.* 2006; 103(41): 15014-15019.
58. Miller KE, Kim Y, Huh W, Park H. Bimolecular fluorescence complementation (BiFC) analysis: Advances and recent applications for genome-wide interaction studies. *J. Mol. Biol.* 2015; 427(11): 2039-2055.
59. Song YB, Park CO, Jeong J, Huh W. Monitoring G protein-coupled receptor activation using an adenovirus-based β -arrestin bimolecular fluorescence complementation assay. *Anal. Biochem.* 2014; 449: 32-41.
60. Butko MT, Yang J, Geng Y, et al. Fluorescent and photo-oxidizing TimeSTAMP tags track protein fates in light and electron microscopy. *Nat. Neurosci.* 2012; 15(12): 1742-1751.
61. Cardullo RA. Theoretical principles and practical considerations for fluorescence resonance energy transfer microscopy. *Methods Cell Biol.* 2013; 114: 441-456.
62. Lam AJ, St-pierre F, Gong Y, et al. Improving FRET dynamic range with bright green and red fluorescent proteins. *Nat. Methods.* 2012; 9(10): 1005-1012.
63. Laviv T, Kim BB, Chu J, Lam AJ, Lin MZ, Yasuda R. Simultaneous dual-color fluorescence lifetime imaging with novel red-shifted fluorescent proteins. *Nat. Methods.* 2016; 13(12): 989-992.
64. Shcherbakova DM, Cox Cammer N, Huisman TM, Verkhusha VV, Hodgson L. Direct multiplex imaging and optogenetics of rho GTPases enabled by near-infrared FRET. *Nat. Chem Biol.* 2018; 14(6):5 91-600.

65. Leavesley SJ, Rich TC. Overcoming limitations of FRET measurements. *Cytometry A*. 2016; 89(4): 325-327.
66. Alford S, Abdelfattah A, Ding Y, Campbell R. A fluorogenic red fluorescent protein heterodimer. *Chem. Biol.* 2012; 19(3): 353-360.
67. Alford SC, Ding Y, Simmen T, Campbell RE. Dimerization-dependent green and yellow fluorescent proteins. *ACS Synth. Biol.* 2012; 1(12): 569-575.
68. Ding Y, Li J, Enterina JR, et al. Ratiometric biosensors based on dimerization-dependent fluorescent protein exchange. *Nat. Methods*. 2015; 12(3): 195-198.
69. Kim J, Lee S, Jung K, et al. Intensiometric biosensors visualize the activity of multiple small GTPases in vivo. *Nat. Commun.* 2019; 10(1): 1-11.
70. Mehta S, Zhang Y, Roth RH, et al. Single-fluorophore biosensors for sensitive and multiplexed detection of signalling activities. *Nat. Cell Biol.* 2018; 20(10): 1215-1225.
71. Ando R, Mizuno H, Miyawaki A. Regulated fast nucleocytoplasmic shuttling observed by reversible protein highlighting. *Science*. 2004; 306(5700): 1370-1373.
72. Mo GCH, Ross B, Hertel F, et al. Genetically-encoded biosensors for visualizing live-cell biochemical activity at superresolution. *Nat. Methods*. 2017; 14(4): 427-434.
73. Martini S, Haddock SHD. Quantification of bioluminescence from the surface to the deep sea demonstrates its predominance as an ecological trait. *Sci. Rep.* 2017; 7(1): 45750.

74. de Wet JR, Wood KV, Helinski DR, DeLuca M. Cloning of firefly luciferase cDNA and the expression of active luciferase in escherichia coli. *Proc. Natl. Acad. Sci. U.S.A.* 1985; 82(23): 7870-7873.
75. Contag CH, Spilman SD, Contag PR, et al. Visualizing gene expression in living mammals using a bioluminescent reporter. *Photochem. Photobiol.* 1997; 66(4): 523-531.
76. Lorenz WW, McCann RO, Longiaru M, Cormier MJ. Isolation and expression of a cDNA encoding renilla reniformis luciferase. *Proc. Natl. Acad. Sci. U.S.A.* 1991; 88(10): 4438-4442.
77. Tannous BA, Kim D, Fernandez JL, Weissleder R, Breakefield XO. Codon-optimized gaussia luciferase cDNA for mammalian gene expression in culture and in vivo. *Mol. Ther.* 2005; 11(3): 435-443.
78. Loening AM, Fenn TD, Wu AM, Gambhir SS. Consensus guided mutagenesis of renilla luciferase yields enhanced stability and light output. *Protein Eng. Des. Sel.* 2006; 19(9): 391-400.
79. Wu AM, Loening AM, Gambhir SS. Red-shifted renilla reniformis luciferase variants for imaging in living subjects. *Nat. Methods.* 2007; 4(8): 641-643.
80. Branchini BR, Ablamsky DM, Davis AL, et al. Analytical biochemistry. *Anal. Biochem.* 1960; 396(2): 290-297.
81. Hall MP, Unch J, Binkowski BF, et al. Engineered luciferase reporter from a deep sea shrimp utilizing a novel imidazopyrazinone substrate. *ACS Chem Biol.* 2012; 7(11): 1848-1857.

82. Dixon AS, Schwinn MK, Hall MP, et al. NanoLuc complementation reporter optimized for accurate measurement of protein interactions in cells. *ACS Chem. Biol.* 2016; 11(2): 400-408.
83. Tran V, Moser LA, Poole DS, Mehle A. Highly sensitive real-time in vivo imaging of an influenza reporter virus reveals dynamics of replication and spread. *J. Virol.* 2013; 87(24): 13321-13329.
84. Hoshino H, Nakajima Y, Ohmiya Y. Luciferase-YFP fusion tag with enhanced emission for single-cell luminescence imaging. *Nat. Methods.* 2007; 4(8): 637-639.
85. Saito K, Chang YF, Horikawa K, et al. Luminescent proteins for high-speed single-cell and whole-body imaging. *Nat. Commun.* 2012; 3(1): 1262.
86. Suzuki K, Kimura T, Shinoda H, et al. Five colour variants of bright luminescent protein for real-time multicolour bioimaging. *Nat. Commun.* 2016; 7(1): 13718.
87. Iwano S, Obata R, Miura C, et al. Development of simple firefly luciferin analogs emitting blue, green, red and near-infrared biological window light. *Tetrahedron.* 2013; 69(19): 3847-3856.
88. Kuchimaru T, Iwano S, Kiyama M, et al. A luciferin analogue generating near-infrared bioluminescence achieves highly sensitive deep-tissue imaging. *Nat. Commun.* 2016; 7(1): 11856.
89. Iwano S, Sugiyama M, Hama H, et al. Single-cell bioluminescence imaging of deep tissue in freely moving animals. *Science.* 2018; 359(6378): 935-939.
90. Yeh HW, Karmach O, Ji A, Carter D, Martins-Green MM, Ai HW. Red-shifted luciferase–luciferin pairs for enhanced bioluminescence imaging. *Nat. Methods.* 2017; 14(10): 971-974.

91. Yeh H, Wu T, Chen M, Ai HW. Identification of factors complicating bioluminescence imaging. *Biochemistry*. 2019; 58(12): 1689-1697.
92. Bell CJ, Manfredi G, Griffiths EJ, Rutter GA. Luciferase expression for ATP imaging: Application to cardiac myocytes. *Methods Cell Biol*. 2007; 80: 341-352.
93. Baubet V, Le Mouellic H, Campbell AK, Lucas-Meunier E, Fossier P, Brûlet P. Chimeric green fluorescent protein-aequorin as bioluminescent Ca²⁺ reporters at the single-cell level. *Proc. Natl. Acad. Sci. U.S.A.* 2000; 97(13): 7260-7265.
94. Rutter GA, Burnett P, Rizzuto R, et al. Subcellular imaging of intramitochondrial Ca²⁺ with recombinant targeted aequorin: Significance for the regulation of pyruvate dehydrogenase activity. *Proc. Natl. Acad. Sci. U.S.A.* 1996; 93(11): 5489-5494.
95. Ozawa T, Kaihara A, Sato M, Tachihara K, Umezawa Y. Split luciferase as an optical probe for detecting Protein-Protein interactions in mammalian cells based on protein splicing. *Anal. Chem.* 2001; 73(11): 2516-2521.
96. Luker KE, Smith MCP, Luker GD, Gammon ST, Piwnica-Worms H, Piwnica-Worms D. Kinetics of regulated protein-protein interactions revealed with firefly luciferase complementation imaging in cells and living animals. *Proc. Natl. Acad. Sci. U.S.A.* 2004; 101(33): 12288-12293.
97. Remy I, Michnick SW. A highly sensitive protein-protein interaction assay based on gaussia luciferase. *Nat. Methods*. 2006; 3(12): 977-979.
98. Takakura H, Hattori M, Takeuchi M, Ozawa T. Visualization and quantitative analysis of G protein-coupled receptor- β -arrestin interaction in single cells and

specific organs of living mice using split luciferase complementation. *ACS Chem. Biol.* 2012; 7(5): 901-910.

99. Misawa N, Kafi AKM, Hattori, M Miura K, Masuda K, Ozawa T. Rapid and high-sensitivity cell-based assays of Protein–Protein interactions using split click beetle luciferase complementation: An approach to the study of G-protein-coupled receptors. *Anal. Chem.* 2010; 82(6): 2552-2560.

100. Dixon AS, Schwinn MK, Hall MP, et al. NanoLuc complementation reporter optimized for accurate measurement of protein interactions in cells. *ACS Chem. Biol.* 2016; 11(2): 400-408.

101. Kaihara A, Umezawa Y, Furukawa T. Bioluminescent indicators for Ca²⁺ based on split renilla luciferase complementation in living cells. *Anal. Sci.* 2008; 24(11): 1405-1408.

102. Oh Y, Park Y, Cho JH, et al. An orange calcium-modulated bioluminescent indicator for non-invasive activity imaging. *Nat. Chem. Biol.* 2019; 15(5): 433-436.

103. Yang J, Cumberbatch D, Centanni S, et al. Coupling optogenetic stimulation with NanoLuc-based luminescence (BRET) Ca⁺⁺. *Nat. Commun.* 2016; 7: 13268.

104. Inagaki S, Tsutsui H, Suzuki K, et al. Genetically encoded bioluminescent voltage indicator for multi-purpose use in wide range of bioimaging. *Sci. Rep.* 2017; 7(1): 42398.

105. Yoshida T, Kakizuka A, Imamura H. BTeam, a novel BRET-based biosensor for the accurate quantification of ATP concentration within living cells. *Sci. Rep.* 2016; 6(1): 39618.

106. Thestrup T, Litzlbauer J, Bartholomaeus I, Mues M, Russo L, et al. Optimized ratiometric calcium sensors for functional in vivo imaging of neurons and T-lymphocytes. *Nat. Methods*. 2014; 11(2): 175-182.
107. Tsutsui H, Jinno Y, Tomita A, et al. Improved detection of electrical activity with a voltage probe based on a voltage-sensing phosphatase. *J. Physiol*. 2013; 591(18): 4427-4437.
108. Imamura H, Huynh Nhat KP, Togawa H, et al. Visualization of ATP levels inside single living cells with fluorescence resonance energy transfer-based genetically encoded indicators. *Proc. Natl. Acad. Sci. U.S.A.* 2009; 106(37): 15651-15656.
109. Yizhar O, Fenno L, Davidson T, Mogri M, Deisseroth K. Optogenetics in neural systems. *Neuron*. 2011; 71(1): 9-34.
110. Miesenböck G. The optogenetic catechism. *Science*. 2009; 326(5951): 395-399.
111. Gradinaru V, Zhang F, Ramakrishnan C, et al. Molecular and cellular approaches for diversifying and extending optogenetics. *Cell*. 2010; 141(1): 154-165.
112. Boyden ES, Zhang F, Bamberg E, Nagel G, Deisseroth K. Millisecond-timescale, genetically targeted optical control of neural activity. *Nat. Neurosci*. 2005; 8(9): 1263-1268.
113. Hochbaum DR, Zhao Y, Farhi SL, et al. All-optical electrophysiology in mammalian neurons using engineered microbial rhodopsins. *Nat. Methods*. 2014; 11(8): 825-833.

114. Klapoetke NC, Murata Y, Kim SS, et al. Independent optical excitation of distinct neural populations. *Nat. Methods*. 2014; 11(3): 338-346.
115. Greenwald EC, Mehta S, Zhang J. Genetically encoded fluorescent biosensors illuminate the spatiotemporal regulation of signaling networks. *Chem. Rev*. 2018; 118(24): 11707-11794.
116. Kralj JM, Douglass AD, Hochbaum DR, Maclaurin D, Cohen AE. Optical recording of action potentials in mammalian neurons using a microbial rhodopsin. *Nat. Methods*. 2012; 9(1): 90-95.
117. Gong Y, Li JZ, Schnitzer, MJ. Enhanced archaerhodopsin fluorescent protein voltage indicators. *PLoS One*. 2013; 8(6): e66959.
118. Yizhar O, Fenno LE, Prigge M, et al. Neocortical excitation/inhibition balance in information processing and social dysfunction. *Nature*. 2011; 477(7363): 171-178.
119. Chen TW, Wardill TJ, Sun Y, et al. Ultrasensitive fluorescent proteins for imaging neuronal activity. *Nature*. 2013; 499(7458): 295-300.
120. Packer AM, Russell LE, Dalglish HW, Häusser M. Simultaneous all-optical manipulation and recording of neural circuit activity with cellular resolution in vivo. *Nat. Methods*. 2015; 12(2): 140-146.
121. Carrillo-Reid L, Yang W, Bando Y, Peterka DS, Yuste R. Imprinting and recalling cortical ensembles. *Science*. 2016; 353(6300): 691-694.
122. Rickgauer JP, Deisseroth K, Tank DW. Simultaneous cellular-resolution optical perturbation and imaging of place cell firing fields. *Nat. Neurosci*. 2014; 17(12): 1816-1824.

123. Rhoades JL, Nelson JC, Nwabudike I, et al. ASICs mediate food responses in an enteric serotonergic neuron that controls foraging behaviors. *Cell*. 2019;176(1-2): 85-97.e14.
124. Sun F, Zeng J, Jing M, et al. A genetically encoded fluorescent sensor enables rapid and specific detection of dopamine in flies, fish, and mice. *Cell*. 2018; 174(2): 481-496.e19.
125. Patriarchi T, Cho JR, Merten K, et al. Ultrafast neuronal imaging of dopamine dynamics with designed genetically encoded sensors. *Science*. 2018; 360(6396).
126. Rajasethupathy P, Sankaran S, Marshel JH, et al. Projections from neocortex mediate top-down control of memory retrieval. *Nature*. 2015; 526(7575): 653-659.
127. Kim CK, Yang SJ, Pichamoorthy N, et al. Simultaneous fast measurement of circuit dynamics at multiple sites across the mammalian brain. *Nat. Methods*. 2016;13(4):325-328.
128. Jennings JH, Kim CK, Marshel JH, et al. Interacting neural ensembles in orbitofrontal cortex for social and feeding behaviour. *Nature*. 2019; 565(7741): 645-2.
129. Farhi SL, Parot VJ, Grama A, et al. Wide-area all-optical neurophysiology in acute brain slices. *J. Neurosci*. 2019, 0618-19.
130. Dana H, Mohar B, Sun Y, et al. Sensitive red protein calcium indicators for imaging neural activity. *eLife*. 2016; 5.
131. Fan LZ, Nehme R, Adam Y, et al. All-optical synaptic electrophysiology probes mechanism of ketamine-induced disinhibition. *Nat. Methods*. 2018; 15(10): 823-831.

132. Clapham DE. Calcium signaling. *Cell*. 2007; 131(6): 1047-1058.
133. Zhao Y, Araki S, Wu J, et al. An expanded palette of genetically encoded Ca^{2+} indicators. *Science*. 2011; 333(6051): 1888-1891
134. Wu J, Abdelfattah AS, Miraucourt LS, et al. A long stokes shift red fluorescent Ca^{2+} indicator protein for two-photon and ratiometric imaging. *Nat. Commun.* 2014; 5: 5262.
135. Miyawaki A, Llopis J, Heim R, McCaffery JM. Fluorescent indicators for Ca^{2+} based on green fluorescent proteins and calmodulin. *Nature*. 1997; 388(6645): 882-887.
136. Arenkiel BR, Peca J, Davison IG, et al. In vivo light-induced activation of neural circuitry in transgenic mice expressing channelrhodopsin-2. *Neuron*. 2007; 54(2): 205-218.
137. Hastings JW, Johnson CH. Bioluminescence and chemiluminescence. *Meth. Enzymol.* 2003; 360: 75-104.
138. Kurose K, Inouye S, Sakaki Y, Tsuji FI. Bioluminescence of the Ca^{2+} -binding photoprotein aequorin after cysteine modification. *Proc. Natl. Acad. Sci. U.S.A.* 1989; 86(1): 80-84.
139. Agetsuma M, Matsuda T, Nagai T. Methods for monitoring signaling molecules in cellular compartments. *Cell Calcium*. 2017; 64: 12-19.
140. den Hamer A, Dierickx P, Arts R, de Vries JSPM, Brunsveld L, Merckx M. Bright bioluminescent BRET sensor proteins for measuring intracellular caspase activity. *ACS Sens.* 2017; 2(6): 729-734.

141. Ding J, Luo AF, Hu L, Wang D, Shao F. Structural basis of the ultrasensitive calcium indicator GCaMP6. *Sci. China Life Sci.* 2014; 57(3): 269-274.
142. Frommer WB, Davidson MW, Campbell RE. Genetically encoded biosensors based on engineered fluorescent proteins. *Chem. Soc. Rev.* 2009; 38(10): 2833-2841.
143. Schaub FX, Reza MS, Flaveny CA, et al. Fluorophore-NanoLuc BRET reporters enable sensitive in vivo optical imaging and flow cytometry for monitoring tumorigenesis. *Cancer Res.* 2015; 75(23): 5023-5033.
144. Baird GS, Zacharias DA, Tsien RY. Circular permutation and receptor insertion within green fluorescent proteins. *Proc. Natl. Acad. Sci. U.S.A.* 1999; 96(20): 11241-11246.
145. Barykina NV, Subach OM, Doronin DA, et al. A new design for a green calcium indicator with a smaller size and a reduced number of calcium-binding sites. *Sci. Rep.* 2016; 6: 34447.
146. Wu J, Abdelfattah AS, Zhou H, et al. Genetically encoded glutamate indicators with altered color and topology. *ACS Chem. Biol.* 2018; 13(7): 1832-1837.
147. Yang Y, Liu N, He Y, et al. Improved calcium sensor GCaMP-X overcomes the calcium channel perturbations induced by the calmodulin in GCaMP. *Nat. Commun.* 2018; 9(1): 1504.
148. Steinmetz NA, Buetfering C, Lecoq J, et al. Aberrant cortical activity in multiple GCaMP6-expressing transgenic mouse lines. *eNeuro.* 2017; 4(5): 17.20171.

149. Miyawaki A, Griesbeck O, Heim R, Tsien RY. Dynamic and quantitative Ca²⁺ measurements using improved cameleons. *Proc. Natl. Acad. Sci U.S.A.* 1999; 96(5): 2135-2140.
150. Kügler S, Kilic E, Bähr M. Human synapsin 1 gene promoter confers highly neuron-specific long-term transgene expression from an adenoviral vector in the adult rat brain depending on the transduced area. *Gene Ther.* 2003; 10(4): 337-347.
151. Grynkiewicz G, Poenie M, Tsien RY. A new generation of Ca²⁺ indicators with greatly improved fluorescence properties. *J. Biol. Chem.* 1985; 260: 3440-3450.
152. Tank DW, Sugimori M, Connor JA, Llinás RR. Spatially resolved calcium dynamics of mammalian Purkinje cells in cerebellar slice. *Science.* 1988; 242(4879): 773-777.
153. Kerr R, Lev-Ram V, Baird G, Vincent P, Tsien RY, Schafer WR. Optical imaging of calcium transients in neurons and pharyngeal muscle of *C. elegans*. *Neuron.* 2000; 26(3): 583-594.
154. Baker PF, Hodgkin AL, Ridgway EB. Depolarization and calcium entry in squid giant axons. *J. Physiol.* 1971; 218(3): 709-755.
155. Sabatini BL, Oertner TG, Svoboda K. The life cycle of Ca (2+) ions in dendritic spines. *Neuron.* 2002; 33(3): 439-452.
156. Scanziani M, Häusser M. Electrophysiology in the age of light. *Nature.* 2009; 461(7266): 930-939.

157. Qian Y, Rancic V, Wu J, Ballanyi K, Campbell RE. A bioluminescent Ca²⁺ indicator based on a topological variant of GCaMP6s. *Chembiochem*. 2019; 20(4): 516-520.
158. Tsien RY. The green fluorescent protein. *Annu. Rev. Biochem.* 1998; 67(1): 509-544.
159. Bajar BT, Wang ES, Zhang S, Lin MZ, Chu J. A guide to fluorescent protein FRET pairs. *Sensors*. 2016; 16(9): 1488.
160. Zlobovskaya OA, Sergeeva TF, Shirmanova MV, et al. Genetically encoded far-red fluorescent sensors for caspase-3 activity. *Biotechniques*. 2016; 60(2): 62-68.
161. Filonov GS, Verkhusha VV. A near-infrared BiFC reporter for in vivo imaging of protein-protein interactions. *Chem. Biol.* 2013; 20(8): 1078-1086.
162. Pandey N, Nobles CL, Zechiedrich L, Maresso AW, Silberg JJ. Combining random gene fission and rational gene fusion to discover near-infrared fluorescent protein fragments that report on protein-protein interactions. *ACS Synth. Biol.* 2015; 4(5): 615-624.
163. Tchekanda E, Sivanesan D, Michnick SW. An infrared reporter to detect spatiotemporal dynamics of protein-protein interactions. *Nat. Methods*. 2014; 11(6): 641-644.
164. Akerboom J, Carreras Calderón N, Tian L, et al. Genetically encoded calcium indicators for multi-color neural activity imaging and combination with optogenetics. *Front. Mol. Neurosci.* 2013; 6: 2.

165. Baird GS, Zacharias DA, Tsien RY. Circular permutation and receptor insertion within green fluorescent proteins. *Proc. Natl. Acad. Sci. U.S.A.* 1999; 96(20): 11241-11246.
166. Nagai T, Sawano A, Park ES, Miyawaki A. Circularly permuted green fluorescent proteins engineered to sense Ca²⁺. *Proc. Natl. Acad. Sci. U.S.A.* 2001; 98(6): 3197-3202.
167. Shen Y, Dana H, Abdelfattah AS, et al. A genetically encoded Ca²⁺ indicator based on circularly permuted sea anemone red fluorescent protein eqFP578. *BMC Biol.* 2018; 16(1): 9.
168. Ohkura M, Sasaki T, Kobayashi C, Ikegaya Y, Nakai J. An improved genetically encoded red fluorescent Ca²⁺ indicator for detecting optically evoked action potentials. *PLoS ONE.* 2012; 7(7): e39933.
169. Wu J, Liu L, Matsuda T, et al. Improved orange and red Ca²⁺ indicators and photophysical considerations for optogenetic applications. *ACS Chem. Neurosci.* 2013; 4(6): 963-972.
170. Inoue M, Takeuchi A, Horigane SI, et al. Rational design of a high-affinity, fast, red calcium indicator R-CaMP2. *Nat. Methods.* 2015; 12(1): 64-70.
171. Wu J, Abdelfattah AS, Zhou H, et al. Genetically encoded glutamate indicators with altered color and topology. *ACS Chem. Biol.* 2018; 13(7): 1832-1837.
172. Wagner JR, Zhang J, Brunzelle JS, Vierstra RD, Forest KT. High resolution structure of deinococcus bacteriophytochrome yields new insights into

phytochrome architecture and evolution. *J. Biol. Chem.* 2007; 282(16): 12298-12309.

173. Takala H, Björling A, Berntsson O, et al. Signal amplification and transduction in phytochrome photosensors. *Nature.* 2014; 509(7499): 245-248.

174. Akerboom J, Chen T, Wardill TJ, et al. Optimization of a GCaMP calcium indicator for neural activity imaging. *J. Neurosci.* 2012; 32(40): 13819-13840.

175. Piatkevich KD, Suk H, Kodandaramaiah SB, et al. Near-infrared fluorescent proteins engineered from bacterial phytochromes in neuroimaging. *Biophys. J.* 2017; 113(10): 2299-2309.

176. Li L, Li D, Chen S, Chen J, Hu H, Pan H. Potentiation of high voltage-activated calcium channels by 4-aminopyridine depends on subunit composition. *Mol. Pharmacol.* 2014; 86(6): 760-772.

177. Rogawski MA, Barker JL. Effects of 4-aminopyridine on calcium action potentials and calcium current under voltage clamp in spinal neurons. *Brain Res.* 1983; 280(1): 180-185.

178. Shemesh O, Tanese D, Zampini V, et al. Temporally precise single-cell-resolution optogenetics. *Nat. Neurosci.* 2017; 20(12): 1796-1806.

179. Wu J, Liu L, Matsuda T, et al. Improved orange and red Ca²⁺ indicators and photophysical considerations for optogenetic applications. *ACS Chem. Neurosci.* 2013; 4(6): 963-972.

180. Depry C, Allen MD, Zhang J. Visualization of PKA activity in plasma membrane microdomains. *Mol. Biosyst.* 2011; 7(1): 52-58.

181. Harada K, Ito M, Wang X, et al. Red fluorescent protein-based cAMP indicator applicable to optogenetics and in vivo imaging. *Sci. Rep.* 2017; 7(1): 7351-9.
182. Borodinsky LN, Spitzer NC. Second messenger pas de deux: The coordinated dance between calcium and cAMP. *Sci. Signal.* 2006; 2006(336): pe22.
183. Cooper DM, Mons N, Karpen JW. Adenylyl cyclases and the interaction between calcium and cAMP signalling. *Nature.* 1995; 374(6521): 421-424.
184. Kandel ER. The molecular biology of memory: cAMP, PKA, CRE, CREB-1, CREB-2, and CPEB. *Mol. Brain.* 2012; 5: 14.
185. Landa LR, Harbeck M, Kaihara K, et al. Interplay of Ca²⁺ and cAMP signaling in the insulin-secreting MIN6 beta-cell line. *J. Biol. Chem.* 2005; 280(35): 31294-31302.
186. Ohkura M, Sasaki T, Kobayashi C, Ikegaya Y, Nakai J. An improved genetically encoded red fluorescent Ca²⁺ indicator for detecting optically evoked action potentials. *PLoS One.* 2012; 7(7): e39933.
187. Abdelfattah AS, Farhi SL, Zhao Y, et al. A bright and fast red fluorescent protein voltage indicator that reports neuronal activity in organotypic brain slices. *J. Neurosci.* 2016; 36(8): 2458-2472.
188. Fan Y, Chen Z, Ai H. Monitoring redox dynamics in living cells with a redox-sensitive red fluorescent protein. *Anal. Chem.* 2015; 87(5): 2802-2810.
189. Gambetta GA, Lagarias JC. Genetic engineering of phytochrome biosynthesis in bacteria. *Proc. Natl. Acad. Sci. U.S.A.* 2001; 98(19): 10566-10571.

190. Pease LR, Heckman KL. Gene splicing and mutagenesis by PCR-driven overlap extension. *Nat. Protoc.* 2007; 2(4): 924-932.
191. Directed evolution library creation: Methods and protocols. 2nd ed. New York: Springer-Verlag; 2014.
192. Lin J, Sann S, Zhou K, et al. Optogenetic inhibition of synaptic release with chromophore-assisted light inactivation (CALI). *Neuron.* 2013; 79(2): 241-253.
193. Makarov NS, Campo J, Hales JM, Perry JW. Rapid, broadband two-photon-excited fluorescence spectroscopy and its application to red-emitting secondary reference compounds. *Opt. Mater. Express.* 2011; 1(4): 551.
194. Drobizhev M, Makarov NS, Tillo SE, Hughes TE, Rebane A. Two-photon absorption properties of fluorescent proteins. *Nat. Methods.* 2011; 8(5): 393-399.
195. Lakowicz JR. Principles of fluorescence spectroscopy. 3rd ed. Springer US; 2006.
196. Pologruto TA, Sabatini BL, Svoboda K. ScanImage: Flexible software for operating laser scanning microscopes. *Biomed. Eng. Online.* 2003; 2: 13.
197. Gottschalk S, Fehm TF, Deán-Ben XL, Razansky D. Noninvasive real-time visualization of multiple cerebral hemodynamic parameters in whole mouse brains using five-dimensional optoacoustic tomography. *J. Cereb. Blood Flow Metab.* 2015; 35(4): 531-535.
198. Krzywinski M, Altman N. Visualizing samples with box plots. *Nat. Methods.* 2014; 11(2): 119-120.
199. Zhang W, Campbell RE. CHAPTER 4: Optogenetic reporters for cell biology and neuroscience. *Optogenetics*; 2018: 63-98.

200. Yong Qian, Kiryl D Piatkevich, Benedict Mc Larney, et al. A genetically encoded near-infrared fluorescent calcium ion indicator. *Nat. Methods.* 2019; 16(2): 171-174.
201. Arnold FH. Engineering enzymes for non-aqueous solvents. *Trends in Biotechnol.* 1990; 8(9): 244-249.
202. Wardill TJ, Chen T, Schreiter ER, et al. A neuron-based screening platform for optimizing genetically-encoded calcium indicators. *PLoS One.* 2013; 8(10): e77728.
203. Bindels DS, Haarbosch L, van Weeren L, et al. mScarlet: A bright monomeric red fluorescent protein for cellular imaging. *Nat. Methods.* 2017; 14(1): 53-56.
204. Goedhart J, van Weeren L, Hink MA, Vischer NOE, Jalink K, Gadella TWJ. Bright cyan fluorescent protein variants identified by fluorescence lifetime screening. *Nat. Methods.* 2010; 7(2): 137-139.
205. Hitoshi N, Ken-ichi Y, Jun-ichi M. Efficient selection for high-expression transfectants with a novel eukaryotic vector. *Gene.* 1991; 108(2): 193-199.
206. Jun-ichi M, Satoshi T, Kimi A, et al. Expression vector system based on the chicken β -actin promoter directs efficient production of interleukin-5. *Gene.* 1989; 79(2): 269-277.
207. Yu D, Dong Z, Gustafson WC, et al. Rational design of a monomeric and photostable far-red fluorescent protein for fluorescence imaging in vivo. *Protein Sci.* 2016; 25(2): 308-315.

208. Baloban M, Shcherbakova DM, Pletnev S, Pletnev VZ, Lagarias JC, Verkhusha VV. Designing brighter near-infrared fluorescent proteins: Insights from structural and biochemical studies. *Chem. Sci.* 2017; 8(6): 4546-4557.
209. Berridge MJ, Lipp P, Bootman MD. The versatility and universality of calcium signalling. *Nat. Rev. Mol. Cell Biol.* 2000; 1(1): 11-21.
210. Ahrens MB, Orger MB, Robson DN, Li JM, Keller PJ. Whole-brain functional imaging at cellular resolution using light-sheet microscopy. *Nat. Methods.* 2013; 10(5): 413.
211. Peron S, Freeman J, Iyer V, Guo C, Svoboda K. A cellular resolution map of barrel cortex activity during tactile behavior. *Neuron.* 2015; 86(3): 783-799.
212. Dimitre G Ouzounov, Tianyu Wang, Mengran Wang, et al. In vivo three-photon imaging of activity of GCaMP6-labeled neurons deep in intact mouse brain. *Nat. Methods.* 2017; 14(4): 388-390.
213. Susaki E, Tainaka K, Perrin D, et al. Whole-brain imaging with single-cell resolution using chemical cocktails and computational analysis. *Cell.* 2014; 157(3): 726-739.
214. DeFelipe J, Alonso-Nanclares L, Arellano JI. Microstructure of the neocortex: Comparative aspects. *J. Neurocytol.* 2002; 31(3-5): 299-316.
215. Dana H, Sun Y, Mohar B, Hulse B, Hasseman PH, et al. High-performance GFP-based calcium indicators for imaging activity in neuronal populations and microcompartments. *BioRxiv* 2018; doi: 10.1101/434589.
216. Mishin AS, Belousov VV, Solntsev KM, Lukyanov KA. Novel uses of fluorescent proteins. *Curr. Opin. Chem. Biol.* 2015; 27: 1-9